MAGNETO-OPTICAL CONTROL OF COHERENT NONLINEAR PROCESSES

A Dissertation

by

PAUL STEVE HSU

Submitted to the Office of Graduate Studies of
Texas A&M University
in partial fulfillment of the requirements for the degree of

DOCTOR OF PHILOSOPHY

May 2008

Major Subject: Physics

MAGNETO-OPTICAL CONTROL OF COHERENT NONLINEAR PROCESSES

A Dissertation

by

PAUL STEVE HSU

Submitted to the Office of Graduate Studies of
Texas A&M University
in partial fulfillment of the requirements for the degree of

DOCTOR OF PHILOSOPHY

Approved by:

Chair of Committee,	George R. Welch
Committee Members,	Alexei V. Sokolov
	Alexey Belyanin
	Goong Chen
Head of Department,	Edward Fry

May 2008

Major Subject: Physics

ABSTRACT

Magneto-Optical Control of Coherent Nonlinear Processes. (May 2008)

Paul Steve Hsu, B.S., University of National Central University

Chair of Advisory Committee: Dr. George R. Welch

Laser-atom interactions create atomic coherence and large nonlinear atomic polarization. We investigate resonant laser-atom interactions to generate large nonlinearities and control them using magneto-optical fields. Coherent control of high-order susceptibilities and magneto-optical rotation are demonstrated. Experiments are supported by theoretical studies that effectively describe the observed phenomena.

It is shown that a new coherent field, with polarization orthogonal to a weak signal field, can be parametrically generated via an all-resonant four-wave-mixing process. This is demonstrated in a double-ladder system having two intermediate states between a ground and an excited state. It is shown that the parametric-generation process can be coherently controlled by coupling lasers and magnetic fields. It is theoretically established that the underlying physics is a resonant three-photon process with a wide domain of control parameters.

Electromagnetically induced transparency (EIT), where absorption of a weak probe is suppressed via quantum interference, is demonstrated in a usual three-level ladder system. It is observed that in contrast with EIT in a usual ladder system, addition of a second channel helps to suppress the absorption of two weak probe fields in the double-ladder system. The resulting enhancement of transmission in two different channels is due to gain caused by three-photon processes.

Coherent control is strongly limited by coherence lifetime, which is the inverse of the dephasing rate. A lambda-system, having two ground states coupled to a common excited state by lasers, can generate a new eigen (dark)-state that is transparent to

incoming fields and hence suppresses fluorescence. However, ground-state dephasing perturbs the dark state. A new method for measuring the ground-state dephasing rate from fluorescence signals is proposed and a proof-of-principle experiment demonstrated.

While two laser fields in a lambda-system are resonant with their respective transitions, the atomic polarizations are very sensitive to an applied magnetic field. This effect can be used for optical magnetometry. The degree of sensitivity of the magnetometer is determined by two competing parameters–atomic density and laser intensity. It is shown experimentally that the optimal sensitivity reaches saturation, which is contrary to the idea that sensitivity increases indefinitely with an increase in the above parameters.

ACKNOWLEDGMENTS

First, I would like to thank my advisor George Welch for his enthusiasm and fully support during my six years in his group. His deep knowledge of quantum optics and many other fields has been an invaluable resource, and his great curiosity and high standards always inspired and challenged me. George, I consider it as a privilege to have been your student, and I will always remember the time spent in the lab.

I would also like to thank Anil K. Patnaik, who served not only as my mentor collaborator but also as co-supervisor (unofficial) during the completion of this work. He guided me into the physics world of my research with his profound knowledge. I learned lots of quantum optics from Anil, and without him, this dissertation would certainly not have been possible.

In addition, I would like to thank the other members of the dissertation committee, Dr. Alexei Sokolov, Dr. Alexey Belyanin and Dr. Goong Chen. Their feedback on my preliminary exam raised important questions that steered this work in the right direction. Also, Dr. Vladimir A. Sautenkov, Dr. Yuri V. Rostovtsev, Dr. Cen-Yun Ye and Dr. John R. H. Xie in our quantum optics group provided many fruitful discussions and useful experimental suggestions.

I would also like to gratefully acknowledge the useful discussions and the help setting up experiments from Aihua Zhang, Hui chen, Hebin Li, Ling Wang and Joe Musser.

Lastly, I would like to thank my friends and family for their full support and encouragement during my time at Texas A&M. To my parents who taught me the value of hard work and discipline and who sacrificed so much for my education. I cannot thank you enough. This dissertation is dedicated to you.

TABLE OF CONTENTS

CHAPTER Page

LIST OF FIGURES

FIGURE Page

FIGURE Page

FIGURE Page

FIGURE Page

CHAPTER I

INTRODUCTION

The interaction of light and matter is a lively research area, and has been for at least two centuries. The early area of this field was wrestling with the nature of light as rays. By the 17th century, the two rival concepts of corpuscles [1] and waves [2] were well established. In the 19th century, Maxwell built the foundations of modern field theory with a detailed account of light as electromagnetic waves. In the 20th century, the field was revolutionized when Max Plank proposed the important supposition that the electromagnetic energy could be emitted only in quantized form [3], i.e., the energy could only be a multiple of an elementary unit $E = h\nu$. Later followed Albert Einstein's postulation on the rate of emission and absorption of light in the medium [4]. Therefore the absorption and emission of light could be thought to be a property of light-matter interaction. By 1913, Bohr applied the fundamental idea of quantization of atomic dynamics and was able to predict the position of atomic spectra. Since then, the light-matter interaction can be completely described in the atomic system. The two postulates by Plank and Einstein opened a new era of the study of light and matter interaction, in particular, when the coherent light source became available in 1958 [5]. The use of coherent light, for its ability in the selection of excited atoms and the preparation of atoms in a coherent superposition of energy states, have found tremendous applications in the study of light-matter interaction and understanding of the underlying physics in the interaction. In the last two decades, new developments have made it possible to control and manipulate the optical properties of atomic ensembles via coherent laser light. There are numerous excited phenomena that have

---

The journal model is *IEEE Transactions on Automatic Control.*

been observed such as : coherent population trapping (CPT) [6], electromagnetically induced transparency(EIT) [7], lasing without inversion (LIW) [8, 9, 10], laser cooling and trapping of neutral atoms [11], Bose-Einstein condensation (BEC) [12], ultra-slow [13, 14, 15] and superluminal light [16] propagation, and quantum memories for photons [17, 18]. The foundation of those excitements is *atomic coherence*. Therefore, those nonlinear optical processes can be varied via controlling the atomic coherence. This dissertation addresses the control of atomic coherence in three main parts: (i) magneto-optical control of nonlinear process in a double-ladder system, (ii) new method for ground-state dephasing measurement, and (iii)optical magnetometry with intense laser fields.

A. Interaction of electromagnetic wave with matter

The modern concept of light contains elements of both particle and wave. This property is referred to as wave-particle duality. A compatible and unambiguous theoretical explanation of light and the interaction of light and matter is given by Maxwell's electromagnetic theory and the quantum. The combined theory is known as *quantum electrodynamics*. In this section, we present the general methods to describe the basic interaction process between the light and atoms.

1. Maxwell's equation for the propagation dynamic of a classical EM wave

The electromagnetic field radiation propagation through the medium is governed by Maxwell's equations [19]

$$\vec{\nabla} \cdot \vec{\mathbf{D}} = 0, \tag{1.1}$$

$$\vec{\nabla} \cdot \vec{\mathbf{B}} = 0, \tag{1.2}$$

$$\vec{\nabla} \times \vec{\mathbf{E}} + \frac{1}{c}\frac{\partial \vec{\mathbf{B}}}{\partial t} = 0, \tag{1.3}$$

$$\vec{\nabla} \times \vec{\mathbf{H}} - \frac{1}{c}\frac{\partial \vec{\mathbf{D}}}{\partial t} = 0. \tag{1.4}$$

Here $\vec{\mathbf{D}}$ is the displacement, $\vec{\mathbf{E}}$ is the electric field, $\vec{\mathbf{H}}$ is the magnetic field, and c is the speed of light. The electric displacement $\vec{\mathbf{D}}$ and magnetic induction $\vec{\mathbf{B}}$ are defined as

$$\vec{\mathbf{D}} = \vec{\mathbf{E}} + 4\pi\vec{\mathbf{P}},\ \vec{\mathbf{B}} = \vec{\mathbf{H}} + 4\pi\vec{\mathbf{M}}, \tag{1.5}$$

where $\vec{\mathbf{P}}$ is the macroscopic polarization of the media and $\vec{\mathbf{M}}$ is the magnetization of the medium. In this dissertation, the systems under consideration are non-magnetic medium, implying $\vec{\mathbf{M}} = 0$. In this case $\vec{\mathbf{B}}$=$\vec{\mathbf{H}}$, and combining the curl equations (1.3)(1.4) and using (1.5), we get

$$\vec{\nabla} \times \vec{\nabla} \times \vec{\mathbf{E}} + \frac{1}{c^2}\frac{\partial^2}{\partial t^2}(\vec{\mathbf{E}} + 4\pi\vec{\mathbf{P}}) = 0. \tag{1.6}$$

Moreover, in isotropic media $\vec{\mathbf{D}} = \epsilon\vec{\mathbf{E}}$, where ϵ is the permittivity of the medium. Therefore from Eq. (1.1), we get $\vec{\nabla} \cdot \vec{\mathbf{E}} = 0$. By applying this condition in the triple product of Eq. (1.6), the equation (1.6) then reduced to

$$\nabla^2\vec{\mathbf{E}} - \frac{1}{c^2}\frac{\partial^2\vec{\mathbf{E}}}{\partial t^2} = \frac{4\pi}{c^2}\frac{\partial^2\vec{\mathbf{P}}}{\partial t^2}. \tag{1.7}$$

In the following calculations we consider a plane wave, circularly polarized in the $x-y$ plane, propagating along the z-direction in the medium

$$\mathbf{E}(\vec{z}, t) = \hat{\epsilon}\mathcal{E}(z, t)e^{ikz-iwt} + c.c, \tag{1.8}$$

where $\mathcal{E}(z)$ is the amplitude of the field with a central frequency w, propagation wave vector $\vec{k}$ ($k = |\vec{k}|$) and the direction of electric field is $\hat{\epsilon}$. For the continues wave laser, the time dependent of $\mathcal{E}$ is negligible.

If the electric field is written as in Eq. (1.8) then the response of medium is given

by the polarization

$$\vec{\mathbf{P}}(z,t) = \hat{\epsilon}\mathcal{P}(z,t)e^{ikz-iwt} + c.c, \tag{1.9}$$

where $\mathcal{P}$ is a slow varying function of position and time. The induced polarization can be expanded in a Taylor series in the power of the laser field $\vec{\mathbf{E}}$. The α^{th} component of the polarization is

$$\mathcal{P}_\alpha(z,t) = \mathcal{P}_\alpha|_{\mathcal{E}=0} + \underbrace{\sum_\beta (\frac{\partial \mathcal{P}_\alpha}{\partial E_\beta})}_{\chi^{(1)}}|_{\mathcal{E}=0} E_\beta + \frac{1}{2!}\underbrace{\sum_{\beta,\gamma}(\frac{\partial^2 \mathcal{P}_\alpha}{\partial E_\beta \partial E_\gamma})}_{\chi^{(2)}}|_{\mathcal{E}=0} E_\beta E_\gamma + \cdots, \tag{1.10}$$

where the $\chi^{(1)}$ and $\chi^{(2)}$ are known as the linear susceptibility and the second-order nonlinear susceptibility, respectively. In conventional (i.e., linear) optics, the induced polarization depends linearly on the electric field strength, i.e., $\mathcal{P} = \chi^{(1)}E$. The high order susceptibilities, i.e., $\chi^{(n)}(n \gg 1 \text{withn} \in \text{N})$, correspond the nonlinear part of the induced polarization. However, the investigation of interest in this dissertation is to determine the response to the medium to a *weak field*. Hence in this chapter, we will only deal with the the linear susceptibility. For brevity, the superscript in χ has been dropped.

The induced macroscopic polarization $\vec{\mathbf{P}}$(z,t) in Eq. (1.9) can be rewritten as

$$\vec{\mathbf{P}}(z,t) = \vec{\epsilon}\chi(w)\mathcal{E}(z)e^{ikz-iwt} + c.c. \tag{1.11}$$

The susceptibility could be time dependent. However, our concern is only on the steady state behavior.

Now coming back to the Eq. (1.7) with the field propagation along z-direction in (1.8), the corresponding Eq. (1.7) can be rewritten as

$$\frac{\partial^2 \vec{\mathbf{E}}}{\partial z^2} - \frac{1}{c^2}\frac{\partial^2 \vec{\mathbf{E}}}{\partial t^2} = \frac{4\pi}{c^2}\frac{\partial^2 \vec{\mathbf{P}}}{\partial t^2}. \tag{1.12}$$

The expressions for $\vec{\mathbf{E}}$ and $\vec{\mathbf{P}}$ are substituted from Eqs. (1.8) and (1.9) in Eq. (1.12), we get

$$\frac{\partial \mathcal{E}}{\partial z} + \frac{1}{c}\frac{\partial \mathcal{E}}{\partial t} = 2i\pi k\mathcal{P}. \tag{1.13}$$

In the derivation of Eq.(1.13). The characteristic changes of amplitude and phase of the electromagnetic wave are slowly varying functions of position compared to the scale of the optical wavelength, and slowly varying functions of time compared to one cycle of optical oscillation. In this case we can apply the *slowly varying amplitude approximation* [20]:

$$\frac{\partial \mathcal{E}}{\partial z} \ll k\mathcal{E},\ \frac{\partial \mathcal{E}}{\partial z} \ll w\mathcal{E},\ \frac{\partial \mathcal{P}}{\partial t} \ll w\mathcal{P},\ \frac{\partial \mathcal{P}}{\partial t} \ll k\mathcal{P}. \tag{1.14}$$

2. Quantum statistics treatment of atomic dynamics

A quantum mechanical state in the atomic system is represented by $|\psi\rangle$. The behavior of $|\psi\rangle$ should satisfy the Schrodinger equation [21]

$$i\hbar\frac{\partial|\psi\rangle}{\partial t} = H|\psi\rangle, \tag{1.15}$$

where H is the Hamiltonian operator of the system under study. The physical quantities of interest and their time dependence are determined by the solution of this equation. An alternative way, especially to deal with atomic spectroscopic problems, is to consider an operator $\hat{\rho}$ instead of the state vector $|\psi\rangle$. This operator $\hat{\rho}$ is called density operator and it is defined as

$$\hat{\rho} = |\psi\rangle\langle\psi| = \sum_{i,j}\rho_{i,j}|i\rangle\langle j|, \tag{1.16}$$

where $|i\rangle$ is a complete set of atomic states and the matric elements is $\rho_{i,j} = \langle i|\hat{\rho}|j\rangle$.

Thus

$$\mathbf{Tr}\rho = \sum_{\mathrm{i=j}} \rho_{\mathrm{ii}} = 1, \tag{1.17}$$

which satisfy the statement of conservation of probability. Here the trace **Tr** of a n-by-n square matrix is defined to be $\mathbf{Tr}\mathrm{M} = \sum_{\mathrm{n}} \mathrm{M}_{\mathrm{nn}}$. From the Schrodinger equation (1.15), it can be shown that

$$\frac{\partial \rho}{\partial t} = -\frac{i}{\hbar}[H, \rho], \tag{1.18}$$

which is known as the *Liouville equation* of motion for the density matrix [22]. In Eq. (1.18), the decay of the atomic levels due to spontaneous emission is not included. The radiative decay from excited state can be also induced by collisions and other phenomena. The finite lifetime of atomic levels can be described by adding phenomenological decay terms to (1.18) [20], thus the Eq. (1.18) becomes

$$\frac{\partial \rho}{\partial t} = -\frac{i}{\hbar}[H, \rho] - \frac{1}{2}\{\Gamma, \rho\}, \tag{1.19}$$

where Γ is a relaxation matrix, $\{\Gamma, \rho\} = \Gamma\rho + \rho\Gamma$. The decay rates are determined by a relaxation matrix Γ as $\langle i|\Gamma|j\rangle = \gamma_i \delta_{ij}$.

The ijth matrix element of Eq. (1.19) is

$$\frac{\partial \rho_{ij}}{\partial t} = -\frac{i}{\hbar}\sum_k (H_{ik}\rho_{kj} - \rho_{ik}H_{kj}) - \frac{1}{2}\sum_k (\Gamma_{ik}\rho_{kj} + \rho_{ik}\Gamma_{kj}). \tag{1.20}$$

The dynamics of light-atom interaction can be fully described by Eq. (1.20) incorporated with Eq. (1.13).

CHAPTER II

STUDY OF RESONANT $\chi^{(3)}$ PROCESS IN DOUBLE-LADDER SYSTEM

A. Introduction

In this chapter we theoretically study the interaction of light with atoms for the case of a simple four-level double-ladder scheme. We use semiclassical theory, assuming a classical light field and quantized atomic states. The theoretical analysis will focus on the resonant $\chi^{(3)}$ processes in this system.

The chapter is organized as follows. First, we briefly introduce the nonlinear process in the atomic system, especially in the lambda, ladder and double-ladder systems. Then we derive the time evolution density matrix elements in a general double-ladder interaction scheme and analyze the role of $\chi^{(3)}$ terms. Further we derive analytical expressions for the propagation dynamics of the probe fields. Finally, we summarize and conclude the work in this chapter.

B. Brief review of nonlinear process in the atomic system

Kerr nonlinearity, a well known phenomena that refers to the third-order susceptibilities $\chi^{(3)}$ has wide variety of applications such as frequency conversion [23], nonlinear light control [24, 25, 26] and parametric generations [27] etc. This third-order susceptibility can be resonantly enhanced, however the linear absorption also increases as well. With the advent of methods to suppress resonant absorption such as electromagnetically induced transparency (EIT) [7, 28], the resonant enhancement of nonlinear process could be achieved at level of a few photons [29, 30]. In a four-level Λ system, the absorptive part of the enhanced third order nonlinearity can be used to control two photon absorption and achieve quantum switching [25]. The refractive

part of the enhanced third order Kerr nonlinearity can be several orders of magnitude larger than obtained by a conventional three-level scheme, and this can be used for resonant cross phase modulation (XPM) [26, 31, 32]. Enhancement of resonant [33] and off-resonant [34, 35] $\chi^{(3)}$ processes based on EIT in the double-Λ configuration have also been experimentally demonstrated.

Nonlinear optical processes can also be enhanced and controlled by using EIT in a ladder configuration [24, 36, 37, 38]. Tewari and Agarwal [24] have theoretical studied control of phase matching and nonlinear generation in dense media by resonant fields in a ladder system. Several experimental and theoretical works have also been reported by Hakuta et al. [36, 37] on resonant enhancement of nonlinear optical generation by using EIT in ladder configuration with atomic hydrogen. To create an additional control channel for absorption and dispersion of the probe field, researcher have studied an EIT-related atomic system in a double-ladder configuration. Wielandy and Gaeta [39] first experimentally demonstrated the use of quantum coherence to control the polarization state of a probe field. They reported a large birefringence and hence a large polarization rotation in a double-ladder system of ^{85}RB. Futher theoretical investigations by Patnaik and Agarwal [40, 41] showed that the polarization state can be coherently controlled by a strong laser field and a static magnetic field. In a similar level configuration, Yoon et al. have shown laser-induced birefringence (LIB) in Ytterbium atoms and they also used the dispersion part of the LIB signal to stabilize the frequency source for a ring dye laser [42]. In the following, we will provide a detailed theoretical analysis of a double-ladder system.

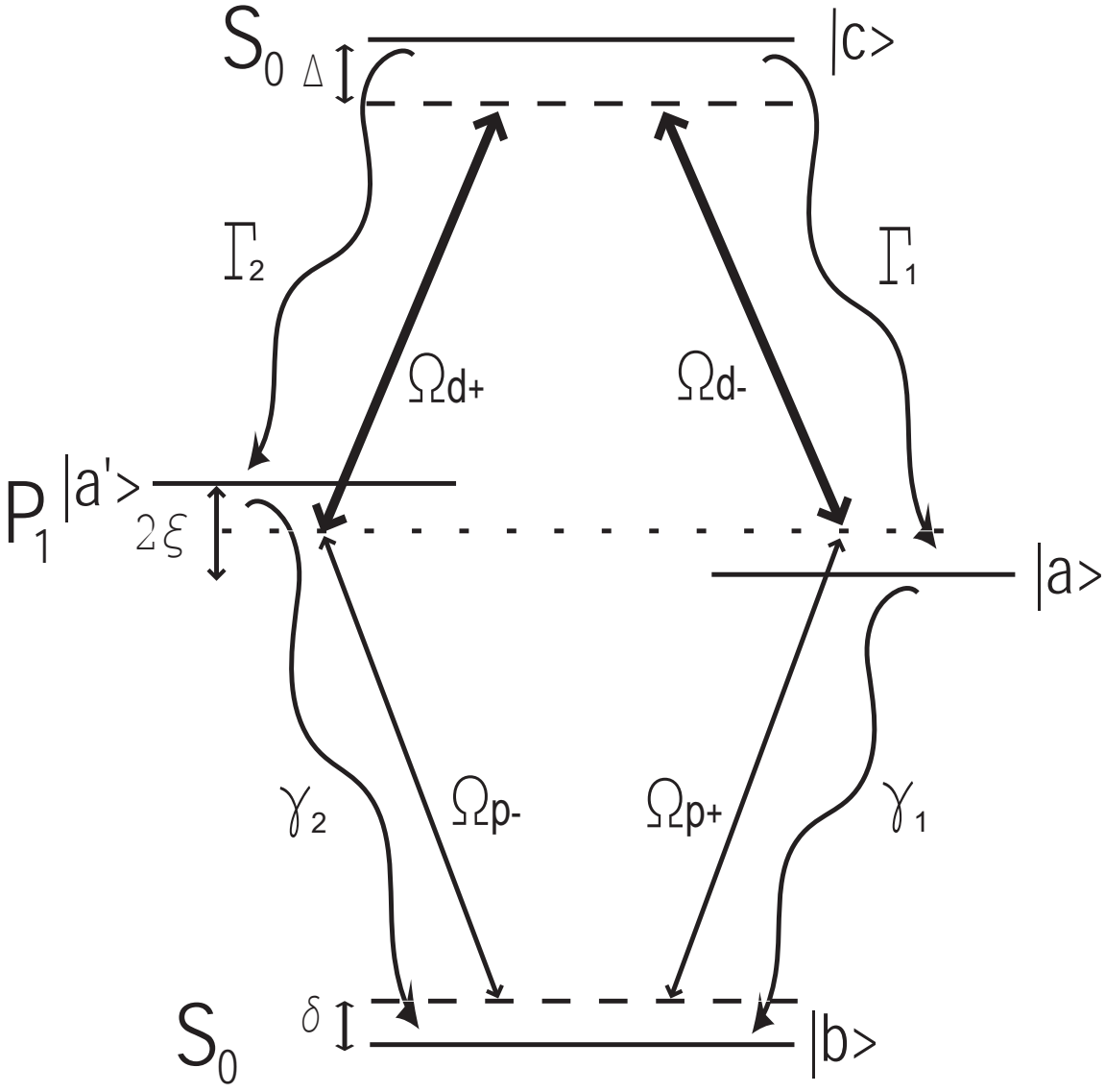

Fig. 1. Diagram showing the energy levels of a double-ladder system.

C. System and atomic dynamics

In this section we theoretically investigate nonlinear $\chi^{(3)}$ processes in a double-ladder system as shown in Fig. 1. We consider the cascaded transitions $|b\rangle \leftrightarrow |a\rangle(|a'\rangle) \leftrightarrow |c\rangle$ that could refer to $|j=0, m=0\rangle \leftrightarrow |j=1, m=\pm 1\rangle \leftrightarrow |j=0, m=0\rangle$ transitions, with $|a\rangle$ and $|a'\rangle$ as the magnetic sublevels with $m=\pm 1$. A weak probe field E_p couples the transitions $|b\rangle$ to $|a\rangle$ and $|a'\rangle$, and a drive field E_d couples transition $|a\rangle$ and $|a'\rangle$ to $|c\rangle$. The fields are assumed to be linearly polarized. For simplicity, the transition $m=0 \leftrightarrow m=0$ is dropped and also it is assumed that the population loss to the $m=0$ state by spontaneous emission could be pumped back by an incoherent pump. Considering the circular polarization component of each field, we have four monochromatic fields propagating along the z direction with polarization $\hat{\epsilon}_{\pm}$,

$$\begin{aligned} \vec{E}_{p\pm}(z,t) &= \mathcal{E}_{p\pm}\hat{\epsilon}_{\pm}(z)e^{-iw_{p\pm}t+ik_{p\pm}z} + c.c., \\ \vec{E}_{d\pm}(z,t) &= \mathcal{E}_{d\pm}\hat{\epsilon}_{\pm}(z)e^{-iw_{d\pm}t+ik_{d\pm}z} + c.c., \end{aligned} \tag{2.1}$$

where the unit polarization vector $\hat{\epsilon}_{\pm}$ corresponds to $\sigma_{\pm}$ polarization, $\mathcal{E}_{\alpha}$ represents the amplitude of the electromagnetic field and k_{α} corresponds to the propagation constant with central frequency ω_{α}; $\alpha \rightarrow p_{\pm}$, $d_{\pm}$. For simplicity, we assume that the two circular components of probe (drive) fields have the same frequency and propagation constant $\omega_{p+} = \omega_{p-} = \omega_p$, $k_{p+} = k_{p-} = k_p$ ($\omega_{d+} = \omega_{d-} = \omega_d$, $k_{d+} = k_{d-} = k_d$).

The dipole matrix elements corresponding to $|c\rangle \leftrightarrow |i\rangle$ and $|i\rangle \leftrightarrow |b\rangle$ (i = a,a′) transition are represented by $\vec{\wp_{ci}}$ and $\vec{\wp_{ib}}$, respectively. These matrix elements can be written with their corresponding unit vectors as

$$\begin{aligned} \vec{\wp_{ca'}} &= -\wp_d\hat{\epsilon}_+, \quad \vec{\wp_{ca}} = \wp_d\hat{\epsilon}_-, \\ \vec{\wp_{a'b}} &= -\wp_p\hat{\epsilon}_-, \quad \vec{\wp_{ca}} = \wp_p\hat{\epsilon}_+, \end{aligned} \tag{2.2}$$

where $\wp_d$ ($\wp_p$) are the dipole moment of drive transitions $j = 0 \leftrightarrow j = 1$ (probe transitions $j = 1 \leftrightarrow j = 0$). In terms of Fig. 1, the atomic Hamiltonian H_o is written as

$$H_o = \hbar[\omega_a A_{aa} + \omega_{a'} A_{a'a'} + \omega_c A_{cc}], \tag{2.3}$$

and the interaction Hamiltonian H_I is

$$H_I = -[\vec{\wp_{ca}} \cdot \vec{E}_{d-} A_{ca} + \vec{\wp_{ca'}} \cdot \vec{E}_{d+} A_{ca'} + \vec{\wp_{ab}} \cdot \vec{E}_{p+} A_{ab} + \vec{\wp_{a'b}} \cdot \vec{E}_{p-} A_{a'b} + H.C.]. \tag{2.4}$$

Here $\hbar\omega_j$ (j=a,a',c) corresponds to the energy separation between $|j\rangle$ and $|b\rangle$, and A_{mn}=$|m\rangle\langle n|$ represents the atomic transition for $m \neq n$ and atomic population for $m = n$. The magnetic sublevles $|a\rangle$ and $|a'\rangle$ are degenerate in our model, therefore the $\omega_{a'}$ is the same as ω_a (ω'_a=ω_a).

The atomic wave function $|\psi\rangle$ will satisfy the Schrodinger equation

$$\frac{\partial}{\partial t}|\psi\rangle = \frac{-i}{\hbar} H|\psi\rangle, \tag{2.5}$$

where $H = H_o + H_I$ is the total Hamiltonian of the system. We perform a unitary transformation $U(t) = exp[iH_o t/\hbar]$ on the wave function $|\psi'\rangle = U(t)|\psi\rangle$. From (2.5), we get

$$\frac{\partial}{\partial t}|\psi'\rangle = \frac{-i}{\hbar} \underbrace{U H_I U^\dagger}_{\bar{H}} |\psi'\rangle = \frac{-i}{\hbar} \bar{H}|\psi'\rangle. \tag{2.6}$$

The Hamiltonian $\bar{H}$ in the interaction picture is

$$\begin{aligned} \bar{H}(t) = & -\hbar[(\Omega_{d+} A_{ca} + \Omega_{d-} A_{ca'}) e^{ik_d z} e^{i\Delta t} + (\Omega_{p+} A_{ab} + \Omega_{p-} A_{a'b}) e^{ik_p z} e^{i\delta t} + \\ & (\Omega'_{d+} A_{ca} + \Omega'_{d-} A_{ca'}) e^{-ik_d z} e^{i(\omega_d + \omega_c)t} + (\Omega'_{p+} A_{ab} + \Omega'_{p-} A_{a'b}) e^{-ik_p z} e^{i(\omega_p + \omega_a)t} \\ & + H.C.], \end{aligned} \tag{2.7}$$

where $\Delta = \omega_d - \omega_c$ is the detuning of the drive field, $\delta = \omega_p - \omega_a$ is the detuning of the probe field, and the coupling Rabi frequencies $\Omega_{p\pm}$ and $\Omega_{d\pm}$ of the probe and drive fields in (2.7) are

$$\begin{aligned} \Omega_{p+} = \frac{\wp_p \mathcal{E}_{p+}}{\hbar} \text{ and } \Omega_{p-} = \frac{-\wp_p \mathcal{E}_{p-}}{\hbar}, \\ \Omega_{d-} = \frac{\wp_d \mathcal{E}_{d-}}{\hbar} \text{ and } \Omega_{d+} = \frac{-\wp_d \mathcal{E}_{d+}}{\hbar}. \end{aligned} \tag{2.8}$$

The spatial dependent term $e^{ik_\alpha z}$ (α = p,d) in the Hamiltonian is assumed to be 1 due to the wavelength $\gg$ dimension of atom, *dipole approximation*, i.e., $k_\alpha z \ll 1$, $e^{ik_\alpha z} \simeq 1$ [20].

It may be noted that (2.7) contains two type of terms, the slow varying terms which the complex exponents multiply Rabi frequencies Ω_s and rapidly oscillation terms, oscillation at a frequencies $(\omega_p + \omega_a)$ and $(\omega_d + \omega_c)$, associated with $\Omega_s^{'}$ (s = $p\pm$, $d\pm$). For a continuous wave laser working at optical frequency $\Omega_s^{'} \ll (\omega_p + \omega_a), (\omega_d + \omega_c)$, then rapidly oscillatory terms are unimportant compared to slow varying term. These terms can therefore be neglected in the *rotating wave approximation (RWA)* [20]. Thus the simplified Hamiltonian can be rewritten as

$$\bar{H}_{RWA}(t) = -\hbar[(\Omega_{d+} A_{ca} + \Omega_{d-} A_{ca'}) e^{i\Delta t} + (\Omega_{p+} A_{ab} + \Omega_{p-} A_{a'b}) e^{i\delta t} + H.C.] \tag{2.9}$$

The approximate interaction Hamiltonian $\bar{H}_{RWA}$ needs to be transformed back to the Schrodinger picture, $H_{I,RWA} = U^\dagger \bar{H}_{RWA} U$.

The atomic Hamiltonian H_0 is unaffected by the approximation, so the total Hamiltonian in the Schrdinger picture under the RAW is

$$\begin{aligned} H_{RWA} &= H_o + H_{I,RWA} \\ &= \hbar[\omega_a A_{aa} + \omega_{a'} A_{a'a'} + \omega_c A_{cc}] - \hbar[(\Omega_{d+} A_{ca} + \Omega_{d-} A_{ca'}) e^{-i\omega_d t} \\ &\quad + (\Omega_{p+} A_{ab} + \Omega_{p-} A_{a'b}) e^{-i\omega_p t} + H.C.]. \end{aligned} \tag{2.10}$$

The equation of motion for the double-ladder system is given by the density-matrix equation

$$\dot{\rho} = \frac{-i}{\hbar}[H_{RWA}, \rho] + \text{decay terms.} \tag{2.11}$$

We consider spatial evolution of the complex Rabi frequency $\Omega_{p\pm}$ corresponding to the probe transitions and the atomic polarization $\mathcal{P}_{\pm} = N\wp_p\rho_{\pm}$ ($\rho_+ = \rho_{ab}$, $\rho_- = \rho_{a'b}$). Here $\rho_{\pm}$ corresponds to the density matrix element in probe transition ρ_{ab} and $\rho_{a'b}$, and N is the atomic density. The propagation of the field along the z direction in the medium is governed by the Maxwell-Bloch equation. The field contains the fast and slow oscillation terms, thus the Maxwell-Bloch equation can be simplified using slowly varying amplitude approximation as [20]

$$\frac{\partial\Omega_{p\pm}}{\partial z} = i\eta\rho_{\pm}, \tag{2.12}$$

where $\eta = k_p N\wp_p^2 \;/\; \hbar\epsilon_0$.

Note that the density matrix elements for probe and drive transitions also contain the slow and fast oscillation terms, therefore we need to use RWA transforming $\rho \rightarrow \tilde{\rho}$ to eliminate the rapid temporal oscillations

$$\begin{aligned} \rho_{jb} &= \tilde{\rho}_{jb}e^{-iw_p t}, \\ \rho_{cj} &= \tilde{\rho}_{cj}e^{-iw_d t}, \\ \rho_{cb} &= \tilde{\rho}_{cb}e^{-i(w_p+w_d)t}, \\ \rho_{j'j'} &= \tilde{\rho}_{j'j'}, \end{aligned} \tag{2.13}$$

where $j = a, a'$ and $j' = a, b, c$.

The dynamic equations for the atomic system evolution are given by the density

matrix equations

$$
\begin{aligned}
\frac{\partial \rho_{cc}}{\partial t} &= -2(\Gamma_1+\Gamma_2)\rho_{cc} + i\Omega_{d-}\rho_{ac} - i\Omega^*_{d-}\rho_{ca} + i\Omega_{d+}\rho_{a'c} \\
&\quad -i\Omega^*_{d+}\rho_{ca'}, \\
\frac{\partial \rho_{ca}}{\partial t} &= -(\Gamma_1+\Gamma_2+\gamma_1+i(\Delta-\xi))\rho_{ca} \\
&\quad +i\Omega_{d-}(\rho_{aa}-\rho_{cc}) + i\Omega_{d+}\rho_{a'a} - i\Omega^*_{p+}\rho_{cb}, \\
\frac{\partial \rho_{ca'}}{\partial t} &= -(\Gamma_1+\Gamma_2+\gamma_2+i(\Delta+\xi))\rho_{ca'}, \\
&\quad +i\Omega_{d+}(\rho_{a'a'}-\rho_{cc}) + i\Omega_{d-}\rho_{aa'} - i\Omega^*_{p-}\rho_{cb}, \\
\frac{\partial \rho_{cb}}{\partial t} &= -(\Gamma_1+\Gamma_2+i(\Delta+\delta))\rho_{cb} \\
&\quad +i\Omega_{d-}\rho_{ab} + i\Omega_{d+}\rho_{a'b} - i\Omega_{p+}\rho_{ca} - i\Omega_{p-}\rho_{ca'}, \\
\frac{\partial \rho_{aa}}{\partial t} &= 2\Gamma_1\rho_{cc} - 2\gamma_1\rho_{aa} + i\Omega^*_{d-}\rho_{ca} \\
&\quad -i\Omega_{d-}\rho_{ac} + i\Omega_{p+}\rho_{ba} - i\Omega^*_{p+}\rho_{ab}, \\
\frac{\partial \rho_{aa'}}{\partial t} &= -(\gamma_1+\gamma_2+2i\xi)\rho_{aa'} + i\Omega^*_{d-}\rho_{ca'} \\
&\quad +i\Omega_{p+}\rho_{ba'} - i\Omega_{d+}\rho_{ac} - i\Omega^*_{p-}\rho_{ab}, \\
\frac{\partial \rho_{ab}}{\partial t} &= -(\gamma_1+i(\delta+\xi))\rho_{ab} + i\Omega_{p+}(\rho_{bb}-\rho_{aa}) \\
&\quad +i\Omega^*_{d-}\rho_{cb} - i\Omega_{p-}\rho_{aa'}, \\
\frac{\partial \rho_{a'a'}}{\partial t} &= 2\Gamma_2\rho_{cc} - 2\gamma_2\rho_{a'a'} + i\Omega^*_{d+}\rho_{ca'} \\
&\quad -i\Omega_{d+}\rho_{a'c} + i\Omega_{p-}\rho_{ba'} - i\Omega^*_{p-}\rho_{a'b}, \\
\frac{\partial \rho_{a'b}}{\partial t} &= -(\gamma_2+i(\delta-\xi))\rho_{a'b} + i\Omega_{p-}(\rho_{bb}-\rho_{a'a'}) \\
&\quad +i\Omega^*_{d+}\rho_{cb} - i\Omega_{p+}\rho_{a'a}, \\
\frac{\partial \rho_{bb}}{\partial t} &= 2\gamma_1\rho_{aa} + 2\gamma_2\rho_{a'a'} + i\Omega^*_{p+}\rho_{ab} \\
&\quad -i\Omega_{p+}\rho_{ba} + i\Omega^*_{p-}\rho_{a'b} - i\Omega_{p-}\rho_{ba'},
\end{aligned}
\tag{2.14}
$$

where the $\delta(\Delta)$ is the detuning of the probe(drive) field from the line center of the intermediate Zeeman states, and 2ξ is the Zeeman splitting created by a static magnetic field. The Γ_l and γ_l (l=1,2) are the rates of spontaneous decay. For simplicity, we assume Γ_l=Γ (γ_l=γ) in the following calculations. To obtain the atomic polarization $\mathcal{P}\pm$ created by the probe transitions, we calculate the off diagonal coherence terms ρ_{ab} and $\rho_{a'b}$. With the assumption of $|\Omega_{d\pm}|\gg|\Omega_{p\pm}|$, the analytical solutions for the steady state are obtained by solving Eqns. (2.14) are

$$\begin{aligned}\rho_{ab} &= \Lambda^{(1)}_{ab}\Omega_{p+} + \Lambda^{(3)}_{ab}\Omega_{p-},\\ \rho_{a'b} &= \Lambda^{(1)}_{a'b}\Omega_{p-} + \Lambda^{(3)}_{a'b}\Omega_{p+}.\end{aligned} \tag{2.15}$$

These solutions are obtained to the first order in both weak fields Ω_{p+} and Ω_{p-}. Writing the solutions explicitly, we have

$$\rho_{ab} = \Omega_{p+}\underbrace{\frac{i[|\Omega_{d+}|^2+(\gamma+i(\delta-\xi))(2\Gamma+i(\Delta+\delta))]}{D_1}}_{\Lambda^{(1)}_{ab}} + \Omega_{p-}\underbrace{\frac{-i\Omega^*_{d-}\Omega_{d+}}{D_1}}_{\Lambda^{(3)}_{ab}}, \tag{2.16}$$

$$\rho_{a'b} = \Omega_{p-}\underbrace{\frac{i[|\Omega_{d-}|^2+(\gamma+i(\delta+\xi))(2\Gamma+i(\Delta+\delta))]}{D_2}}_{\Lambda^{(1)}_{a'b}} + \Omega_{p+}\underbrace{\frac{-i\Omega_{d-}\Omega^*_{d+}}{D_2}}_{\Lambda^{(3)}_{a'b}}, \tag{2.17}$$

where

$$\begin{aligned}D_1 &= |\Omega_{d+}|^2(\gamma+i(\delta+\xi)) + (\gamma+i(\delta-\xi)[|\Omega_{d-}|^2+(2\Gamma+i(\Delta+\delta))(\gamma+i(\delta+\xi))],\\ D_2 &= |\Omega_{d-}|^2(\gamma+i(\delta-\xi)) + (\gamma+i(\delta+\xi)[|\Omega_{d+}|^2+(2\Gamma+i(\Delta+\delta))(\gamma+i(\delta-\xi))].\end{aligned} \tag{2.18}$$

Note that the first terms in both solutions of $\rho_{\alpha\beta}$ correspond to the first order contri-

bution of the weak field to $|\alpha\rangle \leftrightarrow |\beta\rangle$ transition. The second term is the zeroth-order contribution of $\rho_{\alpha\beta}$ which originates from a 3-photon process, for example, $\Lambda^{(3)}_{ab}\Omega_{p-}$ is the zeroth-order term in the expansion of ρ_{ab} for the field Ω_{p+} (i.e., Ω_{p+}=0) but the 3-photon process via absorption of Ω_{p-} and Ω_{d+} followed by stimulated emission in Ω_{d-} results in the $\chi^{(3)}$ process under consideration. Much interesting physics can be derived from Eqs. (2.16) and (2.17). For example, we can independently study the $\chi^{(1)}$ and $\chi^{(3)}$ effects on the two probe transitions in different polarization states. This can be realized if we consider one of the probe fields to be weak relative to the other. Let us denote

$$\begin{aligned} \rho^{(1)}_{ab} = \Lambda^{(1)}_{ab}\Omega_{p+}, \rho^{(3)}_{ab} = \Lambda^{(3)}_{ab}\Omega_{p-}, \\ \rho^{(1)}_{a'b} = \Lambda^{(1)}_{a'b}\Omega_{p-}, \rho^{(3)}_{a'b} = \Lambda^{(3)}_{a'b}\Omega_{p+}. \end{aligned} \tag{2.19}$$

Such that we have $\rho_{ab} = \rho^{(1)}_{ab} + \rho^{(3)}_{ab}$ and $\rho_{a'b} = \rho^{(1)}_{a'b} + \rho^{(3)}_{a'b}$. Setting Ω_{p-} three order magnitude smaller than Ω_{p+}, the $\rho^{(1)}_{a'b}$ shall be negligible compared to $\rho^{(3)}_{a'b}$. Hence $\rho_{a'b}$ is essentially dominated by $\rho^{(3)}_{a'b}$ and ρ_{ab} is dominated by $\rho^{(1)}_{ab}$, and $\rho^{(3)}_{ab}$ can be negligible. Similar conclusion can be made for $\Omega_{p+} \ll \Omega_{p-}$. From Eqs. (2.16)(2.17), we observe that if we set Ω_{d+}=0, $\rho_{a'b}$ reduces to $\rho^{(1)}_{a'b}$ and given as

$$\rho^{(1)}_{a'b} = \frac{i\Omega_{p-}}{(\gamma + i(\delta - \xi))} \tag{2.20}$$

that is a typical 2-level Lorentzian absorption profile, where as $\rho^{(3)}_{a'b}$=0. In the presence of $\Omega_{d\pm}$ the second term $\rho^{(3)}_{a'b}$ in (2.17) produces a gain given by

$$\rho^{(3)}_{a'b} = \frac{-i\Omega_{p+}\Omega_{d-}\Omega^{*}_{d+}}{D_2}. \tag{2.21}$$

We plot the imaginary part of $\rho^{(1)}_{a'b}$, $\rho^{(3)}_{a'b}$ and $\rho_{a'b}$ in the following Fig. 2, where we show the gain contribution from $\rho^{(3)}_{a'b}$ and hence gain in the total Im$[\rho_{a'b}]$. Thus the effect of

resonant $\chi^{(3)}$ process is isolated from the strong $\chi^{(1)}$ processes. Comparing Fig. 2 and Fig. 3, we notice that $\rho_{a'b}$ is totally dominated by $\rho^{(3)}_{a'b}$ when the Ω_{d-} is applied. Note that for all the plots we have assumed the drive field to be resonant, and no magnetic field, i.e., $\Delta = 0$, $\xi = 0$. If the scanning probe fields are off resonance, absorption emerges due to flipping of the sign of $\mathrm{Im}[\rho^{(3)}_{a'b}]$.

D. Propagation dynamics of the probes

Using the derived analytical solutions (2.16) and (2.17). The Maxwell-Block equations (7.6) can be rewritten in matrix form as

$$\frac{\partial}{\partial z}\begin{pmatrix}\Omega_{p+}(z)\\ \Omega_{p-}(z)\end{pmatrix} \equiv i\eta \begin{pmatrix}\Lambda^{(1)}_{ab} & \Lambda^{(3)}_{ab}\\ \Lambda^{(3)}_{a'b} & \Lambda^{(1)}_{a'b}\end{pmatrix}\begin{pmatrix}\Omega_{p+}(z)\\ \Omega_{p-}(z)\end{pmatrix}, \tag{2.22}$$

The propagation of the probe field can thus be calculated by using the eigenvalue and eigenfunction method. For simplicity, we have considered ξ=0, i.e, there is no magnetic field. The solutions for the probes can be obtained from the above equation as

$$\begin{pmatrix}\Omega_{p+}(z)\\ \Omega_{p-}(z)\end{pmatrix} = C_+ e^{\eta\lambda_1 z}\begin{pmatrix}\Omega^*_{d-}\\ \Omega^*_{d+}\end{pmatrix} + C_- e^{\eta\lambda_2 z}\begin{pmatrix}-\Omega_{d+}\\ \Omega_{d-}\end{pmatrix}. \tag{2.23}$$

Solving for the eigenvalue of the 2×2 matrix we get

$$\begin{aligned}\lambda_1 &= \frac{-(2\Gamma + i(\Delta+\delta))}{|\Omega_{d+}|^2 + |\Omega_{d-}|^2 + (\gamma+i\delta)(2\Gamma + i(\Delta+\delta))},\\ \lambda_2 &= \frac{-1}{\gamma + i\delta}.\end{aligned} \tag{2.24}$$

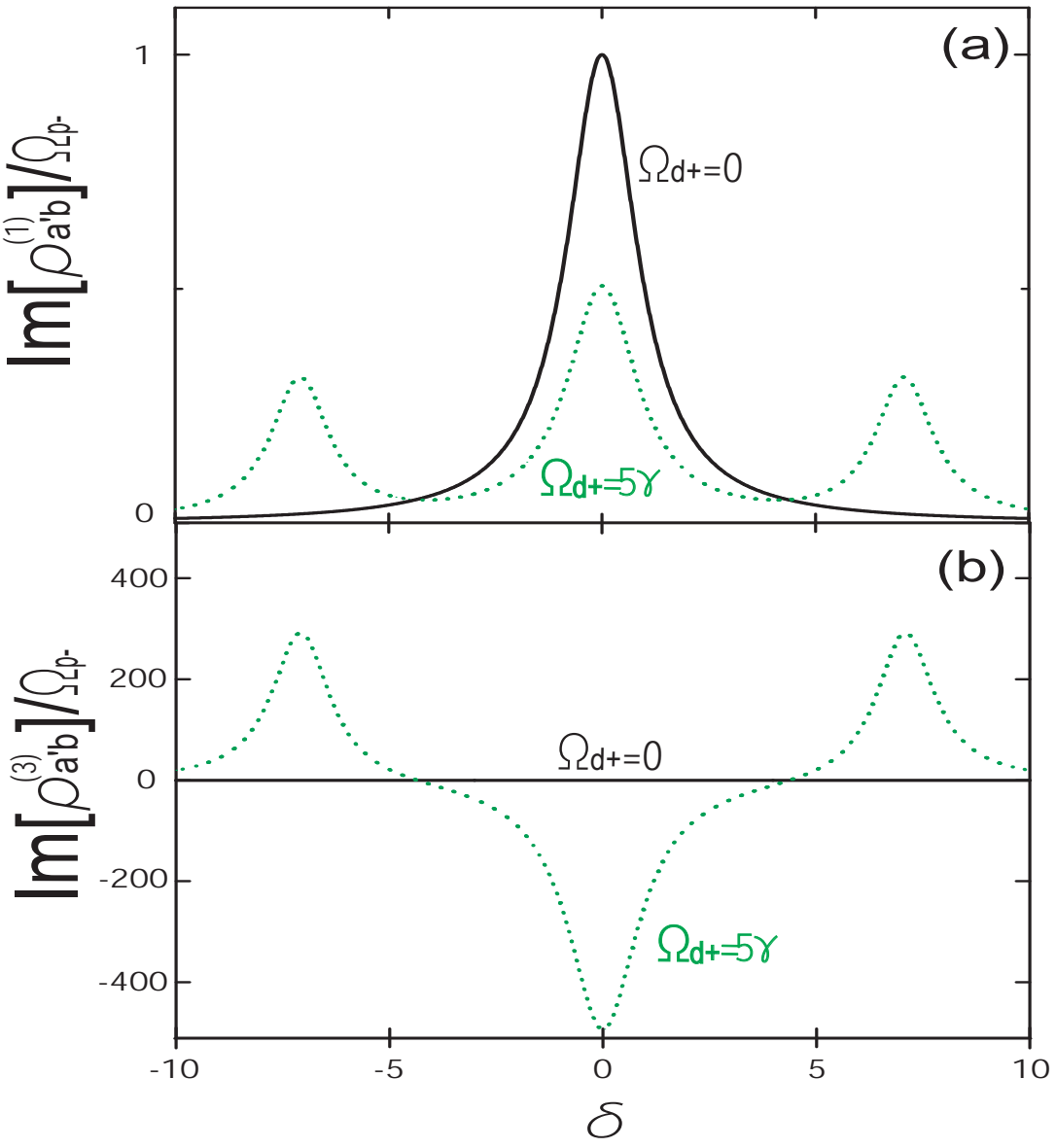

Fig. 2. Plots show the imaginary part of coherence (a) $\mathrm{Im}[\rho^{(1)}_{a'b}]$ (b) $\mathrm{Im}[\rho^{(3)}_{a'b}]$ and (c) $\mathrm{Im}[\rho_{a'b}]$ as a function of probe detuning in the presence of drive field Ω_{d+}=0 (solid line) and Ω_{d+}=5 (dash line). In all the plots, we have assumed Ω_{p+}=0.1, Ω_{p-}=$10^{-3}\times\Omega_{p+}$, Ω_{d-}=5, Γ=0.3 and Δ =0. All the frequencies scale in γ.

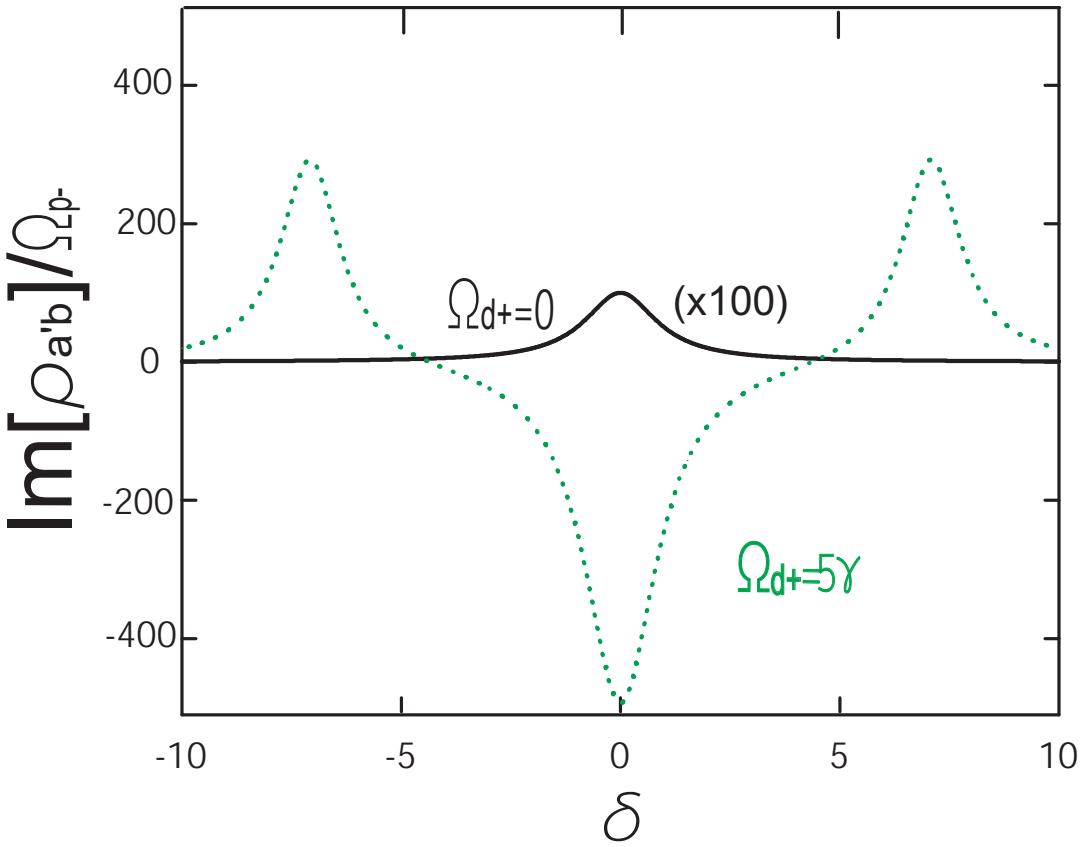

Fig. 3. Plots show the imaginary part of coherence $\mathrm{Im}[\rho_{a'b}]$ as a function of probe detuning in the presence of drive field Ω_{d+}=0 (solid line) and Ω_{d+}=5 (dash line). In the plots, we have assumed Ω_{p+}=0.1, Ω_{p-}=$10^{-3}\times\Omega_{p+}$, Ω_{d-}=5, Γ=0.3 and Δ =0. All the frequencies scale in γ.

The corresponding eigenfunction calculation leads to

$$\begin{aligned} C_+ &= \frac{\Omega_{p-}(0)\Omega_{d+} + \Omega_{p+}(0)\Omega_{d-}}{|\Omega_{d+}|^2 + |\Omega_{d-}|^2}, \\ C_- &= \frac{\Omega_{p-}(0)\Omega^*_{d-} - \Omega_{p+}(0)\Omega^*_{d+}}{|\Omega_{d+}|^2 + |\Omega_{d-}|^2}. \end{aligned} \tag{2.25}$$

To extract the underlying physics from Eqs. (2.23), we focus on the probe Ω_{p+}(z) and identify the regions of interest. From Eqs. (2.23), the solutions of $\Omega_{p\pm}$(z) can be expanded

$$\begin{aligned} \Omega_{p+}(z) &= \frac{\Omega_{p+}(0)|\Omega_{d-}|^2 + \Omega_{p-}(0)\Omega_{d+}\Omega^*_{d-}}{|\Omega_{d+}|^2 + |\Omega_{d-}|^2} \\ &\quad \times \underbrace{\mathrm{Exp}[\frac{-(2\Gamma + i(\Delta+\delta))\eta z}{|\Omega_{d+}|^2 + |\Omega_{d-}|^2 + (\gamma + i\delta)(2\Gamma + i(\Delta+\delta))}]}_{ladder\ transparency} \\ &\quad + \frac{\Omega_{p+}(0)|\Omega_{d+}|^2 - \Omega_{p-}(0)\Omega_{d+}\Omega^*_{d-}}{|\Omega_{d+}|^2 + |\Omega_{d-}|^2} \times \underbrace{\mathrm{Exp}[\frac{-\eta z}{\gamma + i\delta}]}_{2-level\ absorption}, \end{aligned} \tag{2.26}$$

$$\begin{aligned} \Omega_{p-}(z) &= \frac{\Omega_{p+}(0)\Omega_{d-}\Omega^*_{d+} + \Omega_{p-}(0)|\Omega_{d+}|^2}{|\Omega_{d+}|^2 + |\Omega_{d-}|^2} \\ &\quad \times \underbrace{\mathrm{Exp}[\frac{-(2\Gamma + i(\Delta+\delta))\eta z}{|\Omega_{d+}|^2 + |\Omega_{d-}|^2 + (\gamma + i\delta)(2\Gamma + i(\Delta+\delta))}]}_{ladder\ transparency} \\ &\quad + \frac{\Omega_{p-}(0)|\Omega_{d-}|^2 - \Omega_{p+}(0)\Omega_{d-}\Omega^*_{d+}}{|\Omega_{d+}|^2 + |\Omega_{d-}|^2} \times \underbrace{\mathrm{Exp}[\frac{-\eta z}{\gamma + i\delta}]}_{2-level\ absorption}. \end{aligned} \tag{2.27}$$

From the above equations, one observes the following: (i) when the weak probe field Ω_{p+} and the strong drive field Ω_{d-} are present and on resonance with their respective transitions, the probe shows maximum transmission through the medium

due to the EIT as shown in Fig. 4(a). The high transmission of the probe field can be understood as due to the creation of the dark state between the states $|c\rangle$ and $|b\rangle$. This result can be directly seen from our analytical solution once the *2-level absorption* term is dropped from Eq. (2.26) due to Ω_{d+}=Ω_{p-}=0 and therefore only the *ladder transparency* term

$$\Omega_{p+}(z) \quad = \quad \Omega_{p+}(0)\mathrm{Exp}[\frac{-(2\Gamma + i(\Delta+\delta))\eta z}{|\Omega_{d-}|^2 + (\gamma + i\delta)(2\Gamma + i(\Delta+\delta))}], \tag{2.28}$$

remains. Furthermore, if we let Ω_{d-}=0 and $\Omega_{d+} \neq 0$, then Eq. (2.26) reduces to a typical solution for the two level system

$$\Omega_{p+}(z) = \Omega_{p+}(0)\mathrm{Exp}[\frac{-\eta z}{\gamma + i\delta}]. \tag{2.29}$$

(ii) If a strong resonant drive field Ω_{d+} is applied to the above ladder-EIT condition in addition to Ω_{d-} (and Ω_{p-}=0), then the dark state created by Ω_{p+} and Ω_{d-} is perturbed, increasing the absorption of the probe Ω_{p+}.

The absorption of Ω_{p+} followed by Ω_{d-} optically pumps the state $|c\rangle$ which is then coherently transferred to the state $|a'\rangle$ via the Ω_{d+} field, inducing the generation of a $\chi^{(3)}$ field Ω_{p-}, shown as solid line in Fig. 4(b).

(iii) Next we consider when all four fields are present, the amplitudes of the drive fields are the same ($\Omega_{d+} = \Omega_{d-} = \Omega_d$), the amplitudes of the probe fields are the same ($\Omega_{p+}(0) = \Omega_{p-}(0) = \Omega_p(0)$), and all the drive fields are resonant to their respective transitions and probe fields have the same detuning. Under such conditions, the transmission spectra for the two probe fields are identical due to the symmetric configuration of the double ladder system, shown in Fig. 4(c). Then Eqs. (2.26) and (2.27) for two probe fields can be reduced to

$$\Omega_{p+}(z) = \Omega_{p-}(z) \quad = \quad \Omega_p(0)\mathrm{Exp}[\frac{-(2\Gamma + \mathrm{i}(\delta+\Delta))\eta \mathrm{z}}{2|\Omega_\mathrm{d}|^2 + (\gamma + \mathrm{i}\delta)(2\Gamma + \mathrm{i}(\delta+\Delta))}]. \tag{2.30}$$

The amplitude and width of the transmission spectra of two probe fields is higher and broader than the transmission spectra of ladder-EIT shown in Fig. 4(a). With two channels established to generate ladder coherences, the dark state which in the linear combination of $|c\rangle$ and $|b\rangle$ becomes more robust with the symmetric configuration in a double-ladder system. Hence a higher transmission is observed. A detailed discussion of the enhancement in probe transmission will be discussed elsewhere. The increase of transmission linewidth due to power broadening originates from the two strong drive fields coupling to the common excited state $|c\rangle$.

From Fig. 4(b), we notice that the maximum transmission of the generated $\chi^{(3)}$ field occurs while the other three fields are on resonance. Therefore, optical control of the $\chi^{(3)}$ process in an all-resonant condition can be achieved as discussed in the following. To have the probe $\chi^{(1)}$ field and the generated $\chi^{(3)}$ field separated in two transitions with different polarization states, we turn off one of the input probe fields and keep the other three fields (the probe and two drives) on resonance (i.e., $\Omega_{p-}(0)$=0; $\Omega_{p+}(0)$, $\Omega_{d\pm} \neq 0$; $\delta = \Delta = 0$). As a further step, assuming that the optical medium is thin $\eta z \ll \gamma$ and the drive field is strong $|\Omega_{d+}|^2 \gg \gamma\Gamma$, we expand the exponential terms to first order in their arguments. Thus Eqs. (2.26) and (2.27) can be simplified to

$$\Omega_{p+}(z) \approx \Omega_{p+}(0)[1 - \frac{|\Omega_{d+}|^2 \eta z}{\gamma(|\Omega_{d+}|^2 + |\Omega_{d-}|^2)}], \tag{2.31}$$

$$\Omega_{p-}(z) \approx \frac{\Omega_{p+}(0)\Omega_{d-}\Omega_{d+}^*}{|\Omega_{d+}|^2 + |\Omega_{d-}|^2}\frac{\eta z}{\gamma}. \tag{2.32}$$

In Fig. 5 (a), we present a numerical plot of the intensity of probe field Ω_{p+} and the generated $\chi^{(3)}$ field Ω_{p-} as a function of the intensity of the drive field $|\Omega_{d+}|^2$, when all fields are on resonance. The high transmission of the probe due to the EIT created

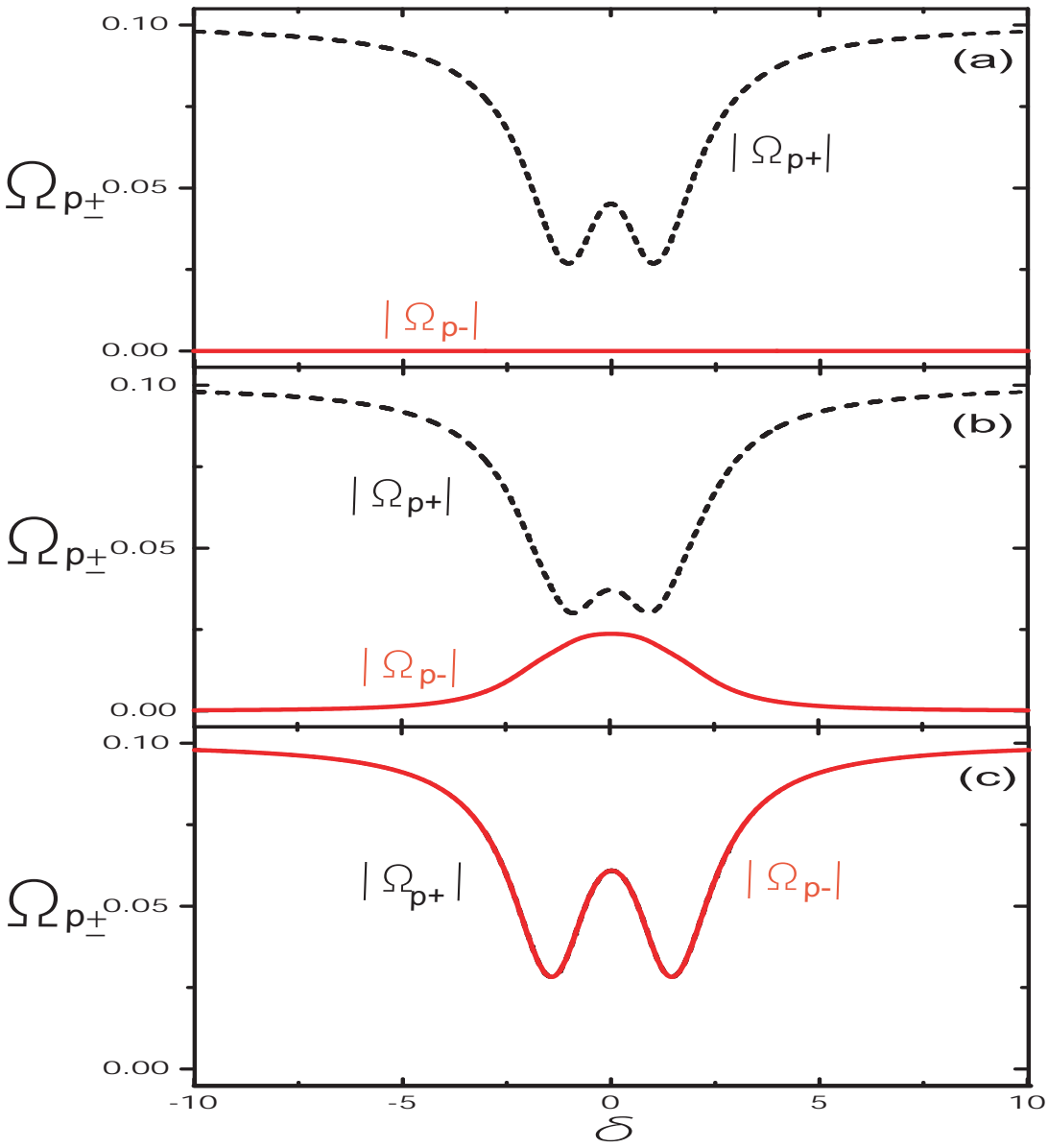

Fig. 4. Theoretically calculated probe transmission as a function of probe detuning from resonance under different conditions. The dashed line is probe $|\Omega_{p+}|$ and solid line is probe $|\Omega_{p-}|$ with $\Omega_{p+}(0)$=0.1, Δ=0, Γ=0.3 and ηz=2. In (a) Ω_{d-}=1, Ω_{d+}=0; (b) Ω_{d-}=Ω_{d+}=1; (c) Ω_{d-}=Ω_{d+}=1, $\Omega_{p-}(0)$=$\Omega_{p+}(0)$=0.1. All the frequencies scale in with γ.

by the strong drive field Ω_{d-} is reduced via the increase of Ω_{d+}. At the same time, more population is optically pumped to the state $|c\rangle$ to generate the $\chi^{(3)}$ field. In Fig. 5(b), when Ω_{d-}=0, only the probe Ω_{p+} and drive Ω_{d+} are present. Because the two fields are not coupled to each other, the probe has low transmission due to the resonant absorption and no $\chi^{(3)}$ field is generated. Applying the drive field Ω_{d-} not only helps to increase probe transmission, but also generates the $\chi^{(3)}$ field through the three photon resonant process. The Fig. 5 (a) and (b) can be described by using Eqs. (2.31) and (2.32). The intensities of both the probe and the $\chi^{(3)}$ fields have quadratic dependence on the drive field intensity $|\Omega_{d+}|^2$ but with opposite signs, as shown in above Eqns. (2.31) and (2.32).

In Fig. 5 (a) and (b), we observe that the amplitude of the $\chi^{(3)}$ field is maximum when the amplitudes of the two orthogonal drive fields are the same ($\Omega_{d\pm}$=Ω_d). To study the optimal generation efficiency of the resonant $\chi^{(3)}$ process, we plot the intensity of output probe and the $\chi^{(3)}$ field as a function of the drive field intensity $|\Omega_d|^2$, shown in Fig. 5 (c). Initially, larger drive field intensity helps to improve the transmission of the probe field and increase amplitude of the $\chi^{(3)}$ field. However, when the drive fields are very strong $|\Omega_d^2| \gg \gamma\Gamma$, the transmission of probe field and the $\chi^{(3)}$ field are saturated. Since the amplitude of two drive field are the same, the above Eqs. (2.31) and (2.32) can be further simplified to

$$\Omega_{p+}(z) \approx \Omega_{p+}(0)[1 - \frac{\eta z}{2\gamma}], \tag{2.33}$$

$$\Omega_{p-}(z) \approx \Omega_{p+}(0)\frac{\eta z}{2\gamma}. \tag{2.34}$$

From Eqs. (2.33) and (2.34) we observe that the output probe field Ω_{p+} and the $\chi^{(3)}$ field Ω_{p-} both are independent of the strong drive fields. This explains the saturation behavior of the two probe fields as shown in Fig. 5 (c).

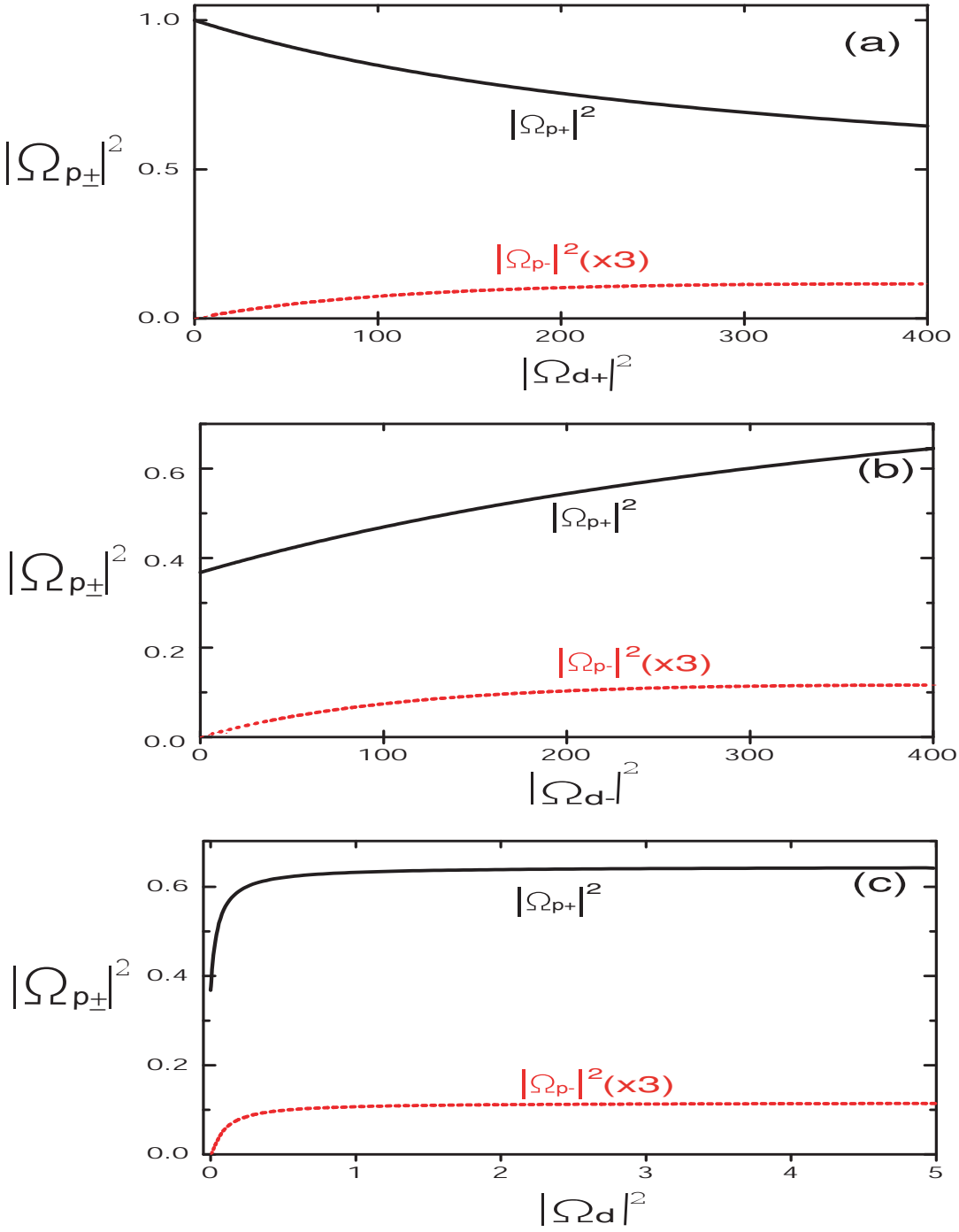

Fig. 5. Plots show the intensity of output fields $|\Omega_{p+}|^2$ (solid line) and $|\Omega_{p-}|^2$ (dash line) vary with the drive field. In these plots , the input fields $\Omega_{p+}(0)$=1 and δ=Δ=0. In (a) Ω_{d-}=20, Ω_{d+} is varying, (b) Ω_{d+}=20, Ω_{d-} is varying. (c) $\Omega_{d\pm}$=Ω_d, Ω_d is varying. All the frequencies scale in γ and ηz=0.05.

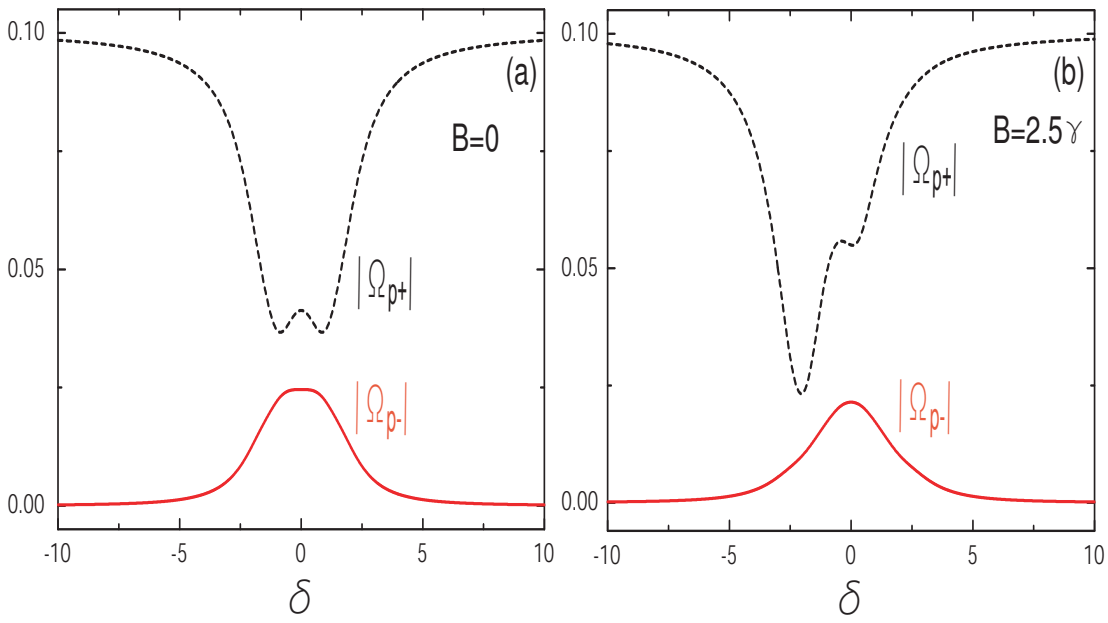

Fig. 6. Plots show the probe field Ω_{p+} (dash line) and generated $\chi^{(3)}$ field Ω_{p-} (solid line) as a function of probe detuning in the presence of (a) B=0 and (b) B=2.5. Input probe $\Omega_{p+}(0)$=0.1, drive fields Ω_{d+}=Ω_{d-}=1, and ηz=1.5. All the frequencies scale in γ.

The resonant $\chi^{(3)}$ process can also be affected by a static magnetic field as shown in Fig. 6. We discovered that the central frequency of the transmission peak for probe Ω_{p+} and the generated field Ω_{p-} remains the same and is unaffected by the magnetic field. However, the magnetic-field-induced Zeeman level shift leads to a decrease of population transfer through the resonant three photon process, which results in the reduction of intensity of the transmission spectrum of the generated field.

E. Summary

We have derived general analytical solutions for the medium polarization corresponding to the two circular polarization of probe fields in a double-ladder system. We have studied the role of the zeroth-order three-photon terms on our analytical so-

lution. We also demonstrate that significant gain on the probe transition can be created through the resonant $\chi^{(3)}$ process and the probe polarization can be totally dominated by the three-photon gain. The analytical solutions for propagation dynamic of two probes are derived. A detail analysis for the analytical expressions in various parameter domain was given. The use of the resonant $\chi^{(3)}$ process for field generation and for optical switching and control can have important applications for optical communication and networking.

CHAPTER III

MAGNETO-OPTICAL CONTROL OF PARAMETRIC GENERATION VIA ALL-RESONANT FOUR-WAVE MIXING PROCESS IN DOUBLE-LADDER SYSTEM

In chapter II we have theoretically studied the resonant $\chi^{(3)}$ process in a double-ladder system. From our analytical results, a new field can be generated via the strong resonant $\chi^{(3)}$ process. This generation process is also a four-wave mixing process, because the generated three-photon signal can be only detected in a specific direction which is defined by the wave vector equation, i.e., $\vec{k}_{g-} = \vec{k}_{p+} + \vec{k}_{d-} - \vec{k}_{d+}$ where $\vec{k}_{g-}$ and $\vec{k}_{p+}$ are the wave vectors for the generated new field and probe, $\vec{k}_{d-}$ and $\vec{k}_{d+}$ are the wave vector for two drive fields in different polarization states. To properly describe the generation process, we use the term four-wave mixing process instead of the resonant $\chi^{(3)}$ process in the following.

In this chapter, we experimentally demonstrate parametric generation of a new coherent field with a polarization orthogonal to the signal field via an all-resonant four-wave mixing process in a double-ladder system. We show that the generation of the coherent field is an efficient resonantly-enhanced process that can be realized in a fairly dilute medium with relatively weak drive fields. Experimentally, we can control both the generated field and also the input probe field simultaneously via the optical fields and by applied magnetic fields.

A. Introduction

Parametric generation of coherent optical fields has been a subject of great interest for the last couple few decades from both the perspectives of rich fundamental physics and its wide ranging applications. The underlying non-linear polarization that gov-

erns the generation process are predominantly either via parametric down conversion or Raman four-wave mixing. These are typically weak off-resonant processes which require driving the system by very high intensity lasers to get reasonable signal-to-noise ratio [27]. However, with the advent of methods to suppress resonant absorption such as Electromagnetically Induced Transparency (EIT) [28, 38], the resonant enhancement of non-linear processes can be achieved even at very low light levels [25]. Recently, coherent generation of a narrow-band field using off-resonant four-wave mixing (FWM) has been reported in a dense atomic medium [33, 34, 35, 43]. The spectral width of such a field is shown to be narrowed by the dispersive properties of the dense medium [35]. However, in certain applications, such as polarization optical switching [39, 40, 41, 42], a broader spectral width is more useful. Another popular off-resonant field generation is coherent anti-Stokes Raman scattering (CARS) in a double-lambda configuration [44]. However, the generation of a signal field is still limited by the high intensity of the drive field, noise from the off-resonant field, and a stringent phase matching condition to separate the (generated) anti-Stokes field from other three fields [44, 45, 46].

In this dissertation, we propose *an efficient and highly controllable resonant FWM process in a double-ladder system* to parametrically generate coherent light. In contrast to the resonant FWM in a lambda system [35], our system generates the field with a broader linewidth using relatively low intensity pumps and at a frequency that is the same as the probe laser. In a related work Zhang et. al. [47] have shown multiwave mixing and their interferences. However, unlike their work, the generated field in our system has polarization which is always orthogonal to the probe field, and hence the signal detection is clean and easy.

B. Experimental setup

We use a dilute gas cell consisting of Cesium atomic vapor which has a four level double-ladder configuration, as shown in Fig. 7(a). The probe laser is tuned to the $6^2S_{1/2}$(F=4)$\rightarrow 6^2P_{3/2}$(F′=5) transition and the drive laser to the $6^2P_{3/2}$(F′=5)$\rightarrow 8^2S_{1/2}$ (F=4) (both on the D2 transition). The experimental setup is shown in Fig. 7(b). A Cs vapor cell of length 5 cm is placed inside a two layer magnetic shield to suppress the stray magnetic field that is present in the lab. The density of Cs vapor is controlled with the temperature of the cell. We use a commercial Ti:sapphire laser (Coherent 899, linewidth approximately 500 kHz), tuned to 794.3 nm as the drive laser and an external cavity diode laser as the probe with its wavelength tuned around 852.2 nm. The drive laser is focused to a spot size of 500 μm and the probe is focused to a spot size 200 μm. The probe and drive beams propagate in opposite directions for approximate two-photon Doppler cancellation. The transmitted probe beam is separated from the drive field via a 50/50 beam splitter. A compensating half-wave plate is used to assure that the polarization state is not disturbed by the Brewster angle from the beam splitter. To measure the transmitted spectrum corresponding to the left- and right-circularly polarized light, we use two detectors and a quarter-wave plate oriented at 45° to the polarization of the polarized beam splitter (PBS) to form a balanced detection. The powers in both the probe and drive fields are controlled by adjusting the half-wave plate before the polarizer. The polarizations of both the fields can be varied by rotating the polarizer and the quarter-wave plate. Data is taken by scanning the frequency of the probe laser and recording the transmission of both the circularly polarized fields at the probe frequency on a digital scope.

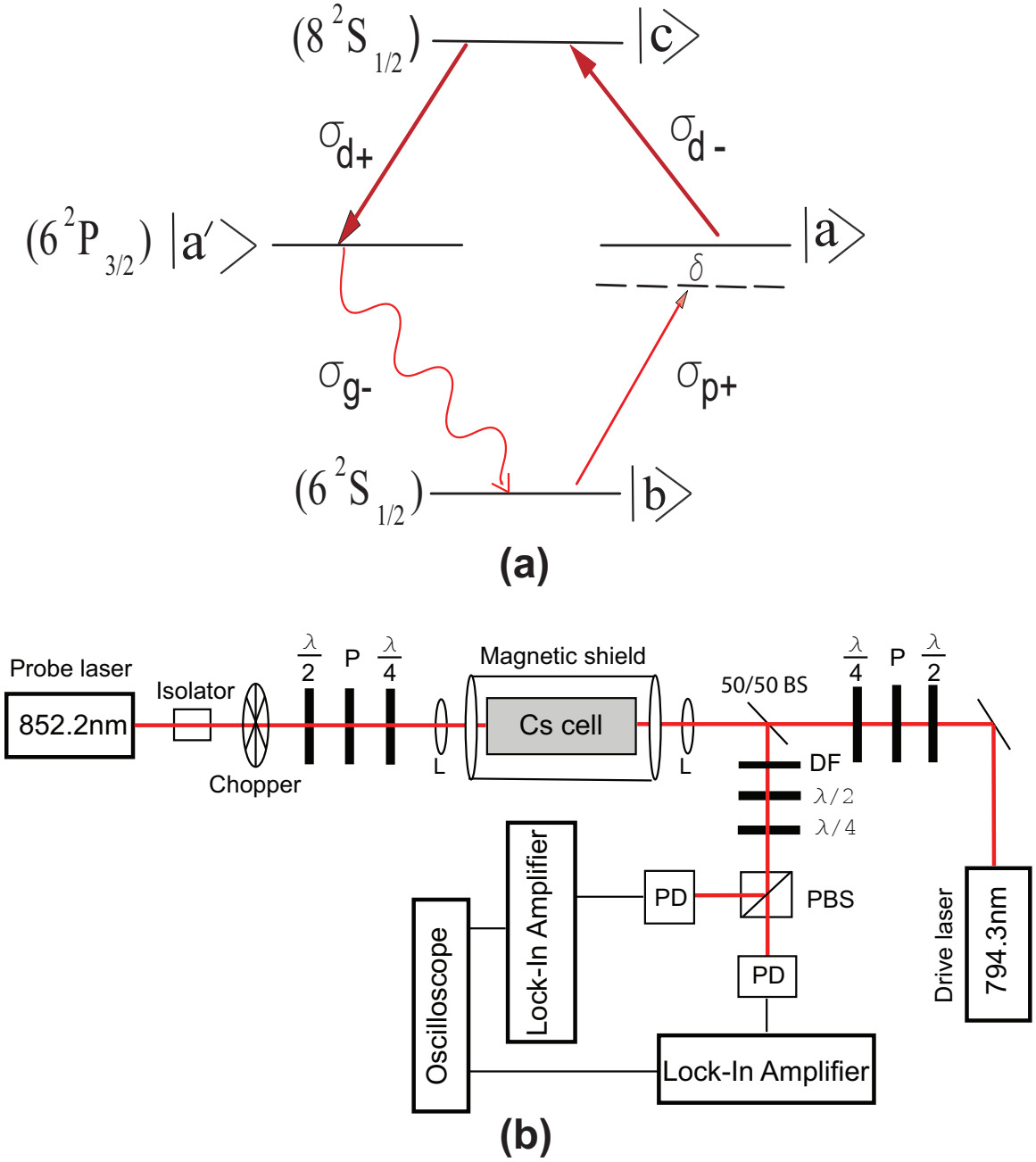

Fig. 7. (a) Diagram showing the ^{133}Cs energy levels. (b) Schematic diagram of the experimental setup: P, Polarizer; $\lambda/2$, half-wave plate; $\lambda/4$, quarter-wave plate; PD, photodiode detector; L, focal lens; BS, beam splitter; DF, dichroic color filter; PBS, polarized beam splitter.

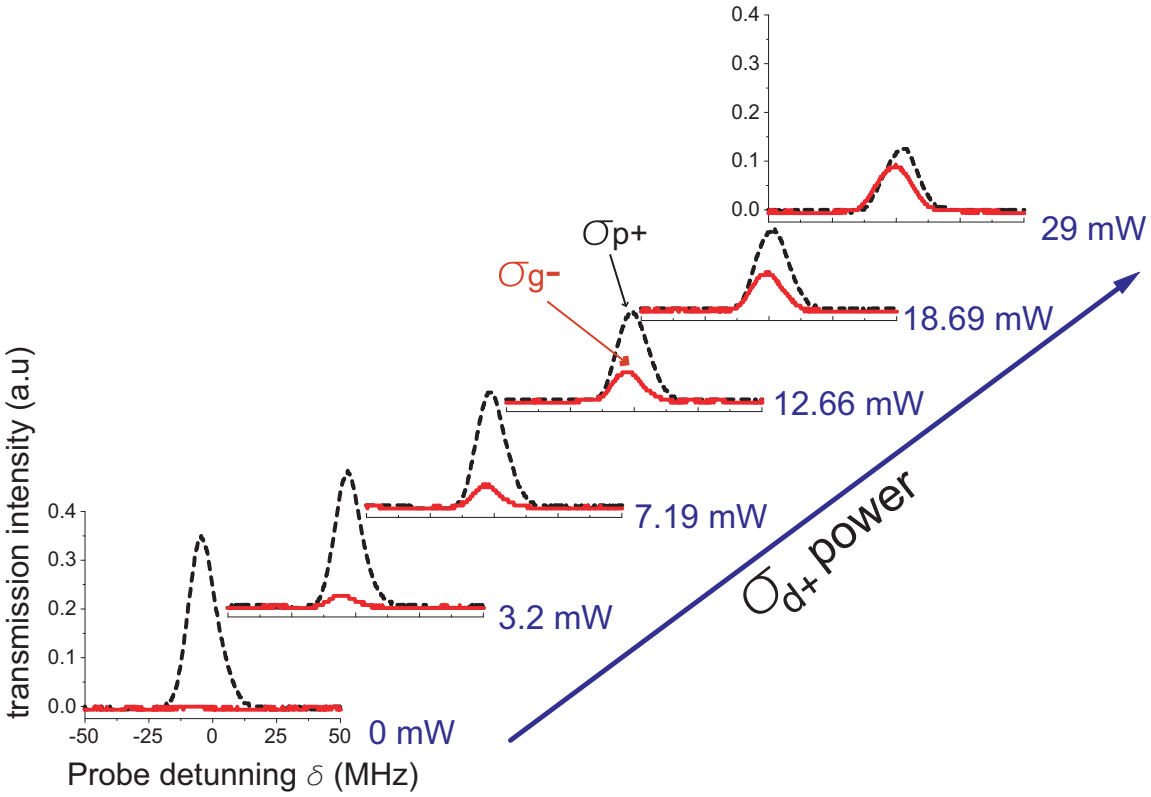

Fig. 8. A 1 μW input probe field σ_{p+} and a 29 mW drive field σ_{d-} couple the Cs atoms with atomic density N=1.1x10^{11} cm^{-3}. The transmission of the probe and new generated field σ_{g-} is varying with the input σ_{d+} drive power.

C. Nonlinear FWM generation via resonant $\chi^{(3)}$ process

1. Optical control of FWM generation

Our main experimental result, shown in Fig. 8, demonstrates efficient generation of the new field in a polarization orthogonal to that of the probe field. Both the drive fields are resonant with their respective transitions. If the drive field σ_{d+} is absent, i.e., only the σ_{p+} and σ_{d-} fields are present, then our system reduces to a standard ladder EIT configuration [38] and hence the probe σ_{p+} transmission is maximum. When the σ_{d+} drive field is turned on, the onset of the generation of σ_{g-} occurs. The power of the generated field σ_{g-} grows with the power of σ_{d+} field. Further, the

transmission of the probe σ_{p+} and generated field σ_{g-} reaches maximum when the probe is on resonance. The maximum transmitted powers of the probe and new fields with increasing drive power is shown in Fig. 9. The high transmission of the probe σ_{p+} field in absence of σ_{d+} can be understood as due to creation of a dark state between states $|c\rangle$ and $|b\rangle$. However, application of the σ_{d+} perturbs the dark state and thus the absorption of the probe σ_{p+} increases. Also more atoms are optically pumped to state $|c\rangle$ which is then coherently transferred to the state $|a'\rangle$ via the σ_{d+} field inducing *a new source polarization* ($\rho_{a'b} \neq 0$) that causes the new field generation. For an input probe power of 1 μW, the maximum power of the generated field in Fig. 9 is about 0.05 μW, which amounts to a conversion efficiency of 5%. The underlying physics is further clarified by the following analytical calculation.

We consider the spatial evolution of the field amplitudes represented by the complex Rabi frequencies $\Omega_{j\pm}$ (j=g,p). We assume that the magnitude of Rabi frequencies of the drive fields $|\Omega_{d\pm}| \gg |\Omega_{p+}|$ and also all the applied fields are on resonance to their respective transitions. Using the slowly varying envelop approximation and dropping the time dependence for our continuous wave fields, the Maxwell equations from Eq. (1.14) can be written for the Rabi frequencies of the probe and generated field as

$$\partial_z \Omega_{p+} = -\eta \mathrm{Im}[\rho_{\mathrm{ab}}], \quad \partial_{\mathrm{z}} \Omega_{\mathrm{g}-} = -\eta \mathrm{Im}[\rho_{\mathrm{a'b}}]. \tag{3.1}$$

Here η=$(3/4\pi)N\lambda^2\gamma$ is equivalent to the inverse of the optical depth; N is the atomic density; λ is wavelength. We can use Eqs. (2.16) and (2.17) to calculate coherences ρ_{ij} under the aforesaid conditions as

$$\mathrm{Im}[\rho_{\mathrm{ab}}] = \frac{\Omega_{p+}}{\gamma} \frac{|\Omega_{d+}|^2 + 2\gamma\Gamma}{|\Omega_{d+}|^2 + |\Omega_{d-}|^2 + 2\gamma\Gamma}, \tag{3.2}$$

$$\mathrm{Im}[\rho_{\mathrm{a'b}}] = -\frac{\Omega_{p+}}{\gamma} \frac{\Omega_{d-}\Omega_{d+}^*}{|\Omega_{d+}|^2 + |\Omega_{d-}|^2 + 2\gamma\Gamma}. \tag{3.3}$$

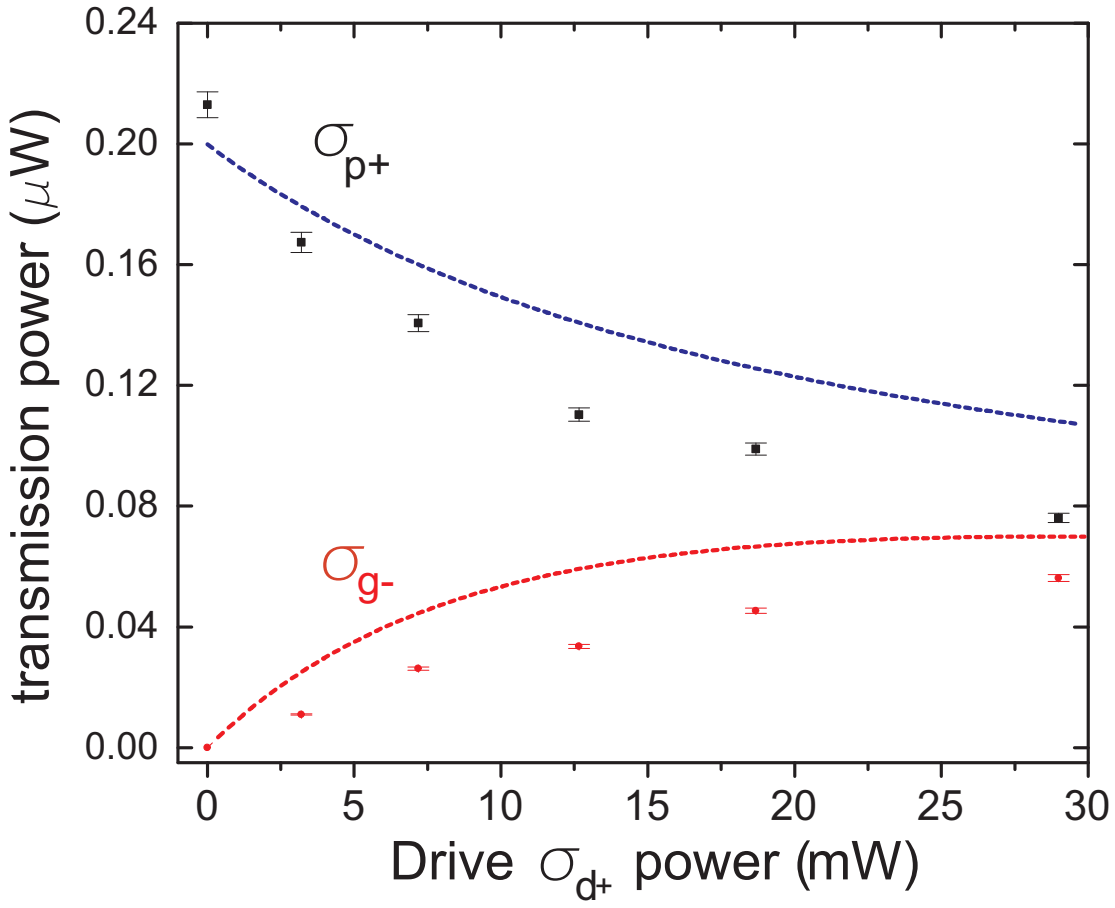

Fig. 9. The corresponding data from Fig. 8 when all fields (probe and two drive fields) are on resonance. The dashed lines are a simple theoretical fit using Eqs. (3.4) and (3.5).

Note that we have ignored the real parts of the coherences as we consider all the fields to be on resonance with their respective transitions–where Re[ρ_{ab}]=Re[$\rho_{a'b}$]=0.

If we consider that the absorption of the probe to be small due to the EIT created by the strong drive field σ_{d-}, the spatial evolution of the Rabi frequency of the probe and the new field along the z direction can be expressed as

$$\frac{\Omega_{p+}(z)}{\Omega_{p+}(0)} \approx 1 - \eta z \frac{|\Omega_{d+}|^2 + 2\gamma\Gamma}{\gamma(|\Omega_{d+}|^2 + |\Omega_{d-}|^2 + 2\gamma\Gamma)}, \tag{3.4}$$

$$\frac{\Omega_{g-}(z)}{\Omega_{p+}(0)} \approx \eta z \frac{\Omega_{d-}\Omega_{d+}^*}{\gamma(|\Omega_{d+}|^2 + |\Omega_{d-}|^2 + 2\gamma\Gamma)}. \tag{3.5}$$

From Eq. (3.5), it is clear that the new field's amplitude is proportional to the amplitude of the input probe field and atomic density. Therefore, a higher power of the new field can be achieved by simultaneously increasing the input probe power and atomic density. Further, from Eqs. (3.4) and (3.5), both the probe field and new field have quadratic dependence, but with opposite sign, on the drive field σ_{d+}. The experimental results shown in Fig. 9 qualitatively agree with Eqs. (3.4) and (3.5). As the Doppler broadening of both σ_{p+} and σ_{g-} fields and also absorption of the σ_{g-} field are ignored, the theoretical plots give higher estimates compared to the experiment. Both the new field and probe field can be controlled via the amplitude as well as the phase of the two drive fields by considering the complex Rabi frequencies as in Eq. (3.5), not shown in the figure. Further, it is interesting to note that the frequency and width of the transmission spectra of the new generated field (several tens of MHz) are the same as the probe field. The frequency of new field and the probe are the same due to the symmetric configuration of the double-ladder system. The broader spectral feature of new field comes from the resonant FWM process in the Doppler broadened medium which will be discussed elsewhere.

The experimental data shown in Fig. 9 can not be quantitatively matched by

Eqs. (3.4) and (3.5) due to not considering the Doppler and FWM signal absorption. To quantitatively match experimental results, we use the analytical solution Eqs. (2.26) and (2.27) which consider the absorption and three-photon gain for both probe and FWM signal. Equations. (2.26) and (2.27) for FWM process can be re-written as

$$\begin{aligned}\Omega_{p+}(z) &= \Omega_{p+}(0)\{\frac{|\Omega_{d-}|^2}{|\Omega_{d+}|^2+|\Omega_{d-}|^2}\mathrm{Exp}[\frac{-2\Gamma\eta z}{|\Omega_{d+}|^2+|\Omega_{d-}|^2+2\gamma\Gamma}] \\ &\quad +\frac{|\Omega_{d+}|^2}{|\Omega_{d+}|^2+|\Omega_{d-}|^2}\mathrm{Exp}[\frac{-\eta z}{\gamma}]\}, \qquad (3.6)\end{aligned}$$

$$\begin{aligned}\Omega_{g-}(z) &= \frac{\Omega_{p+}(0)\Omega_{d-}\Omega_{d+}^*}{|\Omega_{d+}|^2+|\Omega_{d-}|^2}\{\mathrm{Exp}[\frac{-2\Gamma\eta z}{|\Omega_{d+}|^2+|\Omega_{d-}|^2+2\gamma\Gamma)}] \\ &\quad -\mathrm{Exp}[\frac{-\eta z}{\gamma}]\}. \qquad (3.7)\end{aligned}$$

By using Eqs. (3.6) and (3.7) with parameter P1, P2 and P3 to optimize the beam profile and coupling conditions, atomic density in the multilevel system and Rabi frequency for drive field (P1$\cdot\Omega_{p+}(0)$, P2$\cdot\eta z$ and P3$\cdot|\Omega_{d\pm}|^2$). Using Eqs. (3.6) and (3.7) to match the experimental data is better than using the simple reduced solutions Eqs. (3.4) and (3.5), shown in Fig. 10. By analyzing the value of P1, P2 and P3, we can get a good physical picture of (i) how well is our simple comprehensive model working on the complicated multilevel system and (ii) to understand the experimental coupling condition for the probe and drive which is very difficult to measure accurately. A detailed analysis will be discussed in Ref [48].

From the above experimental results, we also discover that the maximum generation of the σ_{p-} field occurs while the power of two drive fields, σ_{d-} and σ_{d+}, are the same. It is known that the combined two equal-amplitude circular components in orthogonal polarization states can be seen as a linearly polarized field. To optimize

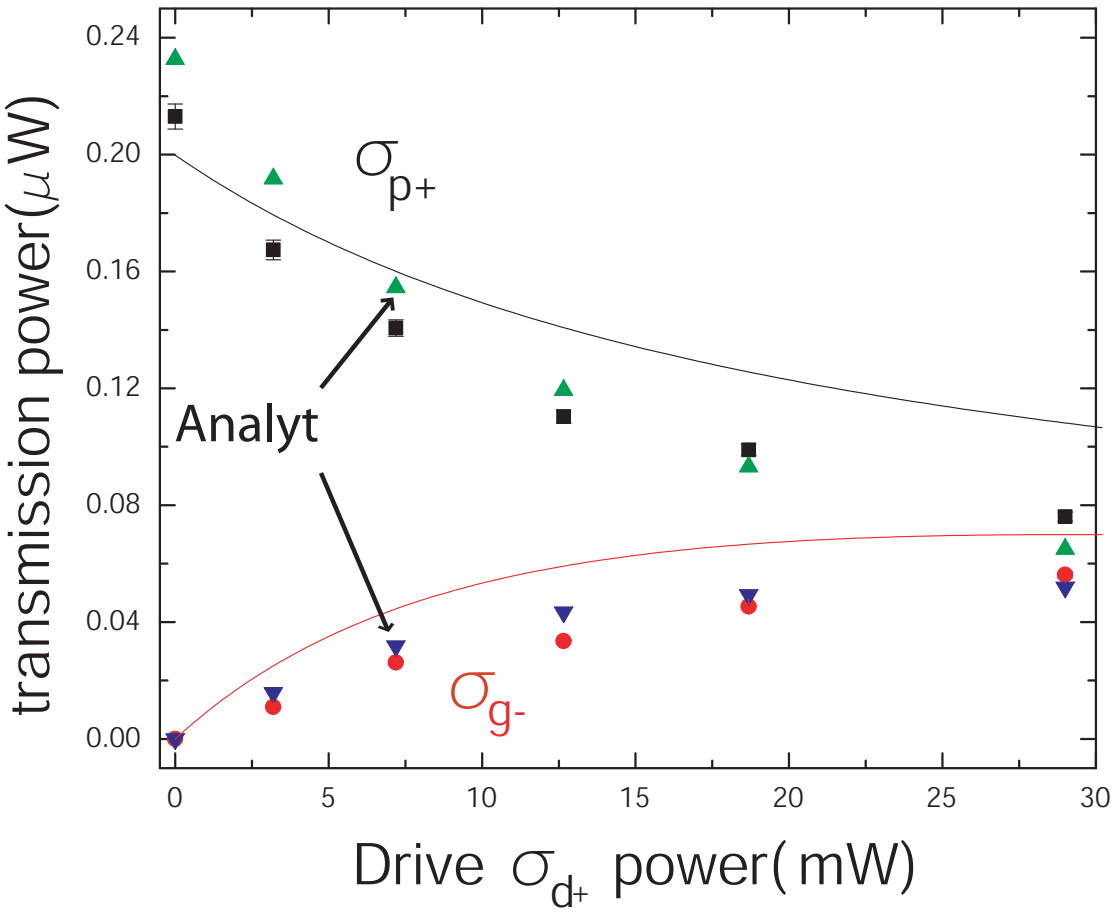

Fig. 10. A 1 μW input probe field σ_{p+} and a 29 mW drive field σ_{d-} couple the Cs atoms with atomic density N=1.1x10^{11} cm^{-3}. The transmission of the probe and new generated field σ_{g-} is varying with the input σ_{d+} drive power. The $\triangle$ and ∇ is using Eqs. (3) and (4) to match experimental results with parameters P1=0.5, P2=0.37, P3=0.00306.

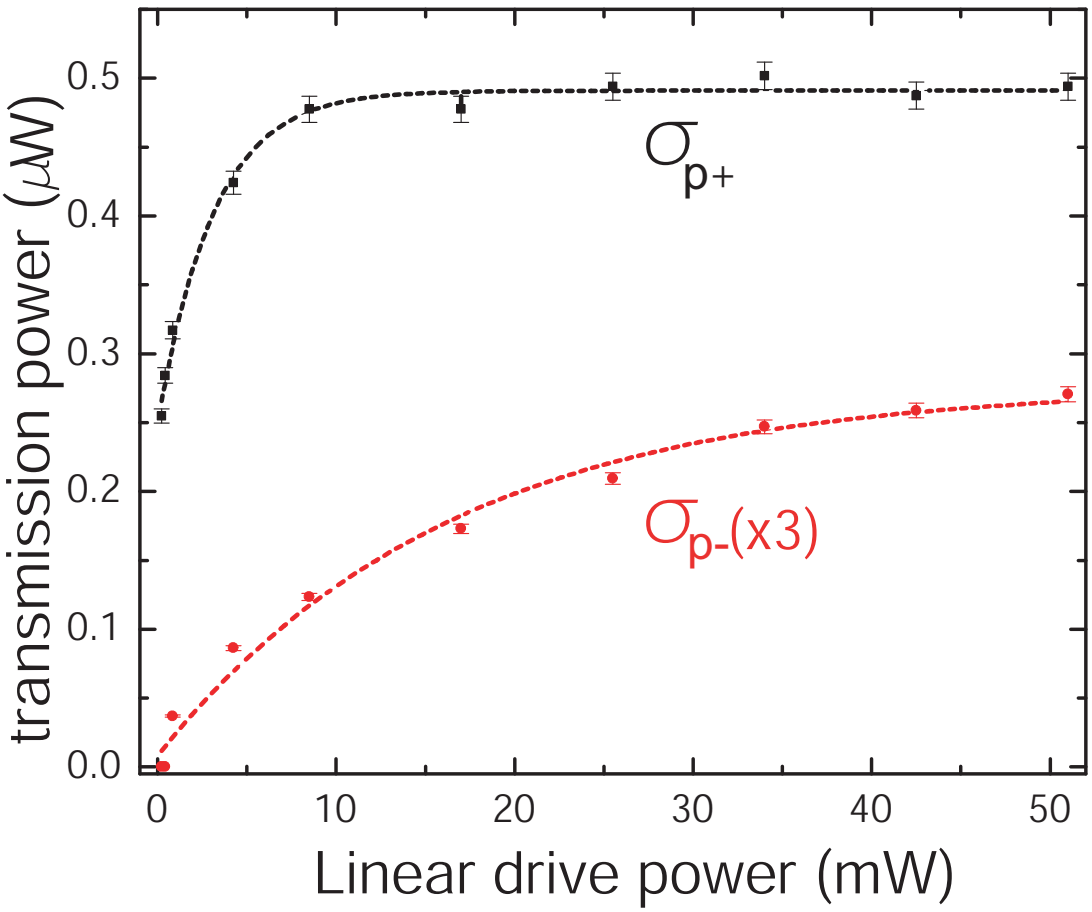

Fig. 11. The transmission of the probe σ_{p+} and generated $\chi^{(3)}$ field σ_{p-} measurement under the conditions of 1 μW input probe σ_{p+} with drive power of σ_{d-} is the same as σ_{d+}(linear polarized light) . All the detunings $\Delta = \delta = \xi$=0 at the atomic density N=3x10^{10} cm^{-3}. The dashed curves are guides for the eye.

the new field generation through the resonant $\chi^{(3)}$ process, we therefore gradually increase the linear drive power as shown in Fig. 11. The saturation of the probe transmission while the linear drive field is strong agrees with Eq. (2.33). However, the transmission saturation of the generated field which is described by Eq. (2.34) is not observed due to the limited the drive power. A detailed analysis of the use of Eqs (3.6) and (3.7) to match the experimental results will also be discussed in Ref [48].

2. Control of FWM generation using a magnetic field

Next we demonstrate the control of this resonant $\chi^{(3)}$ process with a static magnetic field. For ^{133}Cs atom D2 line, a 1 gauss magnetic field causes a Zeeman sublevel shift by $\sim$ 1 MHz [49]. In Fig. 12(a), the probe σ_{p+} field and generated field σ_{p-} show maximum transmission when the probe and a linear drive field are on resonance. Once a magnetic field is applied to the system, the transmission spectra of both fields shifts and the amplitude of the σ_{p-} field decreases. Selected data are shown in Fig. 12 (b)-(d). From our theoretical simulations, shown in Fig. 6, the center frequency of the transmission peak of σ_{p+} and σ_{g-} is not affected by the Zeeman shift. However, in our experimental results, we observe that transmission peak positions of the two fields are functions of magnetic field, shown in Fig. 13. From Fig. 13, the frequency shifting of σ_{p+} and σ_{g-} depend quadratically on the magnetic field. The shift of the transmission peak for both probe fields might result from the induced magnetic dipole moment by the large magnetic field, and this effect can be very strong when the system contains higher excited state optical transitions, e.g., atomic energy level 8S. Further investigation will be discussed in Ref [48].

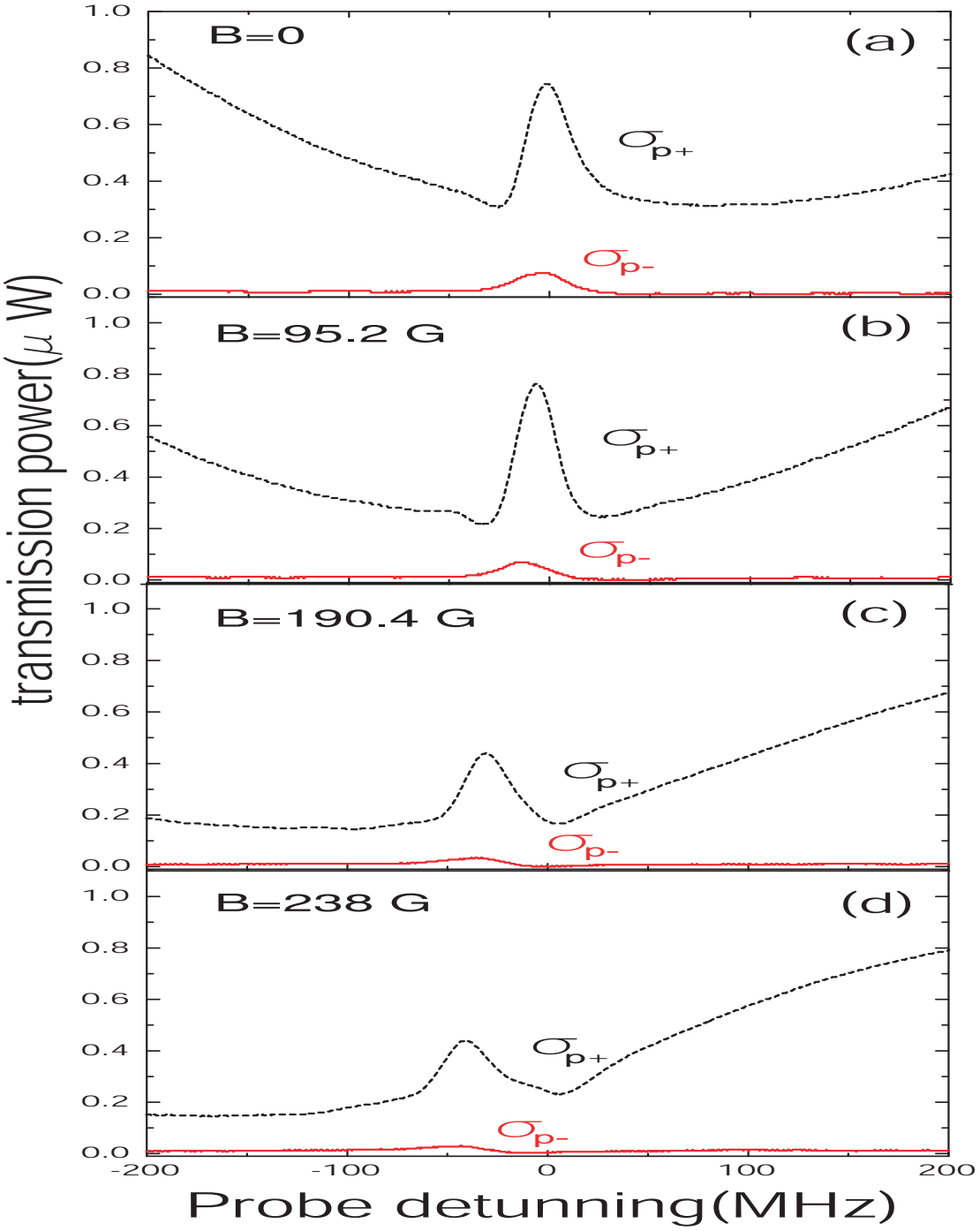

Fig. 12. The transmissions of probe σ_{p+} (dash line) and generated $\chi^{(3)}$ field σ_{p-} (solid line) are a function of probe detuning in present of different external magnetic fields.(a) B=0 G, (b) B=95.2 G (c) B=190.4 G (d) B=238 G. The constant input weak probe field σ_p+=1 μW, linear drive field power 59 mW.

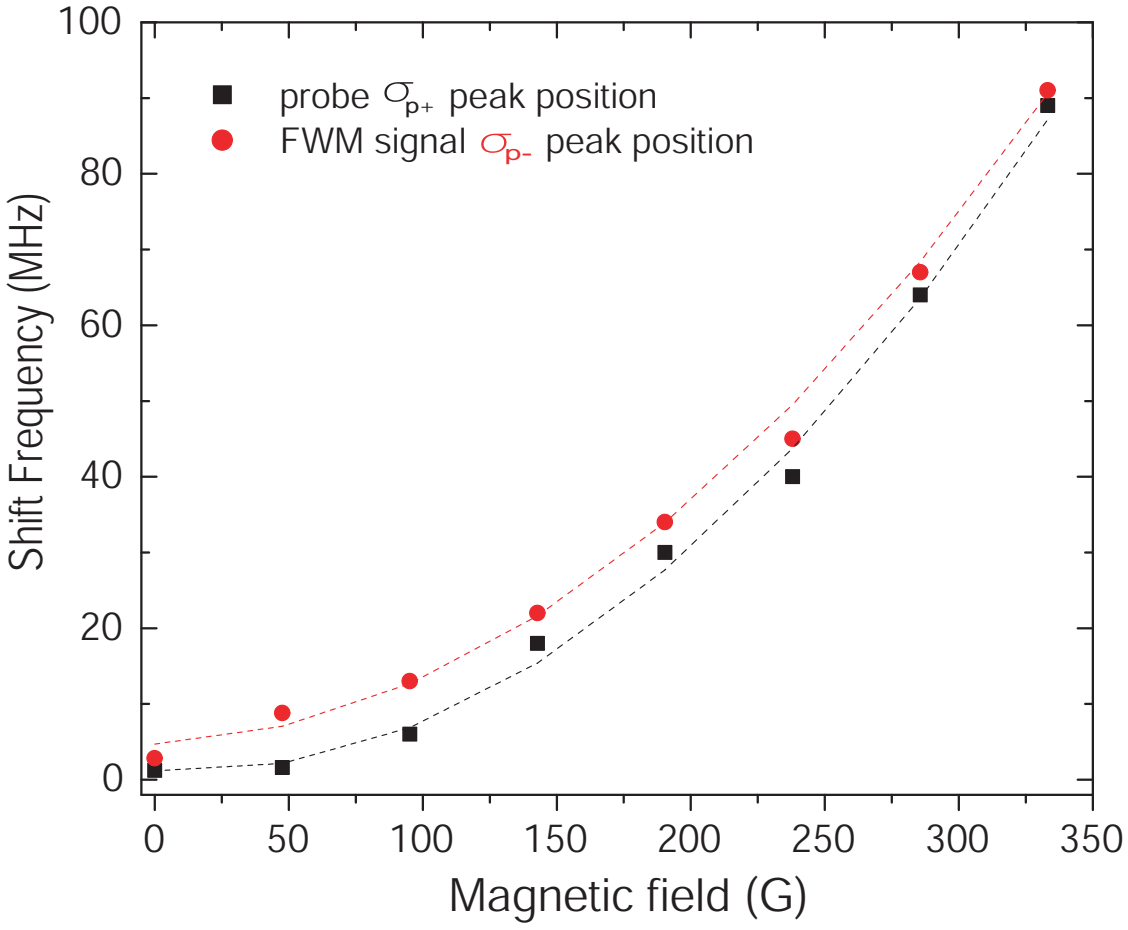

Fig. 13. The frequency shift of transmission peak position of σ_{p+} and σ_{g-}.

CHAPTER IV

TWO CHANNEL PROBE TRANSMISSION ENHANCEMENT OF DOUBLE-EIT VIA RESONANT $\chi^{(3)}$ PROCESS IN A DOUBLE-LADDER SYSTEM

A. Introduction

Electromagnetically Induced transparency (EIT) is an usually thought of as the effect of inducing transparency with a weak probe field in an absorbing medium due to the presence of a strong coupling field on a linked transition. Three popular level schemes for EIT are V, lambda and ladder systems. The induced transparency of lambda and ladder systems is due to population trapping in which the population is transferred into a dark state [28, 38]. Unlike lambda and ladder systems, the induced transparency of the V-type EIT is due to enhanced stimulated emission by the interference of the two optical fields [50]. This controlling of the probe transparency by strong coupling light can have many useful applications in optical communications. To have an additional controllable optical channel, double-EIT has been proposed for controlling two independent probe channels. The applications of double-EIT for magneto-optical rotation, cross phase modulation and polarization phase gate with a tripod atomic system have been discussed in Ref [51, 52]. The double-EIT in a double lambda system is also used for enhanced frequency conversion of nonadiabatic pulses via a four-wave mixing(FWM) process [53] and polarization qubit phase gate [54]. Five level schemes have been proposed to generate double-EIT and optimal cross phase modulation for two slow light pulses with matched group velocities in ^{87}Rb [55].

The quality of EIT is determined by the interruption of the dark state which directly relates to the dark-state dephasing rate. Compared to EIT in a lambda sys-

tem, the induced transparency in the ladder-type atomic system is relative low due to the larger dephasing rate [38]. Moreover, in contrast to EIT in lambda configuration, the relatively low transmission of ladder-type EIT restricts the applications for two channel optical communications.

In this chapter, we experimentally observed that in contrast with EIT in a usual ladder system, the addition of a second channel helps to suppress the absorption of two weak probe fields under double-EIT condition in the double-ladder configuration. We demonstrated that the resulting enhancement of transmission in two different channels is due to new gain caused by the underlying three-photon processes. Our results showed that the transmission of both probe fields is 8% higher than that of the probe in a standard EIT system. We consider these results to have important applications to new types of polarization switching. Whether the probe transmission enhancement of double-EIT exists in the various different systems, i.e., tripod, double-lambda, is analyzed in the Appendix B.

The arrangement of this chapter as follows: a brief review of double-EIT in the atomic system in Sec. II. In Sec. III, we theoretically analyze the transmission enhancement of double-EIT in contrast to the ladder EIT in the double-ladder system. The theoretical prediction of probe transmission enhancement of double-EIT in a double-ladder system can be experimentally verified in Sec. IV. Finally, we summarize in Sec. V.

B. Theoretical analysis of double-EIT and EIT in double-ladder scheme

The theoretical calculations for the density matrix and field propagation for double-ladder system has been developed in Chapter II. We use the notation r=Ω_{d+}/Ω_{d-} and Ω_{d-}=Ω. We rewrite the density element equations Eqs. (2.16) and (2.17) for the

probe transitions

$$\rho_{ab} = \Omega_{p+}\underbrace{i[r^2|\Omega|^2+(\gamma+i\delta))(2\Gamma+i(\Delta+\delta))]/D}_{\Lambda^{(1)}_{ab}} - \Omega_{p-}\underbrace{ir|\Omega|^2/D}_{\Lambda^{(3)}_{ab}}, \quad (4.1)$$

$$\rho_{a'b} = \Omega_{p-}\underbrace{i[|\Omega|^2+(\gamma+i\delta)(2\Gamma+i(\Delta+\delta))]/D}_{\Lambda^{(1)}_{a'b}} - \Omega_{p+}\underbrace{ir|\Omega|^2/D}_{\Lambda^{(3)}_{a'b}}.$$

where

$$D = (\gamma+i\delta)[|\Omega|^2(1+r^2)+(\gamma+i\delta)(2\Gamma+i(\Delta+\delta))] \quad (4.2)$$

The Rabi frequency of the output probe field from Eqs. (2.26) and (2.27) can be also rewritten as

$$\begin{aligned}\Omega_{p+}(z) = {} & \frac{r\Omega_{p-}(0)\Omega+\Omega_{p+}(0)\Omega}{|\Omega|^2(1+r^2)}\mathrm{Exp}[\frac{-(2\Gamma+i(\Delta+\delta))\eta z}{|\Omega|^2(1+r^2)+(\gamma+i\delta)(2\Gamma+i(\Delta+\delta))}] \\ & + \frac{\Omega_{p-}(0)\Omega^*-r\Omega_{p+}(0)\Omega^*}{|\Omega|^2(1+r^2)}\mathrm{Exp}[\frac{-\eta z}{\gamma+i\delta}],\end{aligned} \quad (4.3)$$

$$\begin{aligned}\Omega_{p-}(z) = {} & \frac{r\Omega_{p-}(0)\Omega+\Omega_{p+}(0)\Omega}{|\Omega|^2(1+r^2)}\mathrm{Exp}[\frac{-(2\Gamma+i(\Delta+\delta))\eta z}{|\Omega|^2(1+r^2)+(\gamma+i\delta)(2\Gamma+i(\Delta+\delta))}] \\ & + \frac{\Omega_{p-}(0)\Omega^*-r\Omega_{p+}(0)\Omega^*}{|\Omega|^2(1+r^2)}\mathrm{Exp}[\frac{-\eta z}{\gamma+i\delta}].\end{aligned} \quad (4.4)$$

In the following, we discuss the coherences ρ_{ab} and $\rho_{a'b}$ under the two conditions r=0 and r=1, and demonstrate that in contrast with EIT in a ladder system (r=0 condition) that both probes in the symmetric double-EIT condition (r=1) have higher transmission. For r=0 and Δ=0 condition, the two weak probes $\Omega_{p\pm}$ and the one drive

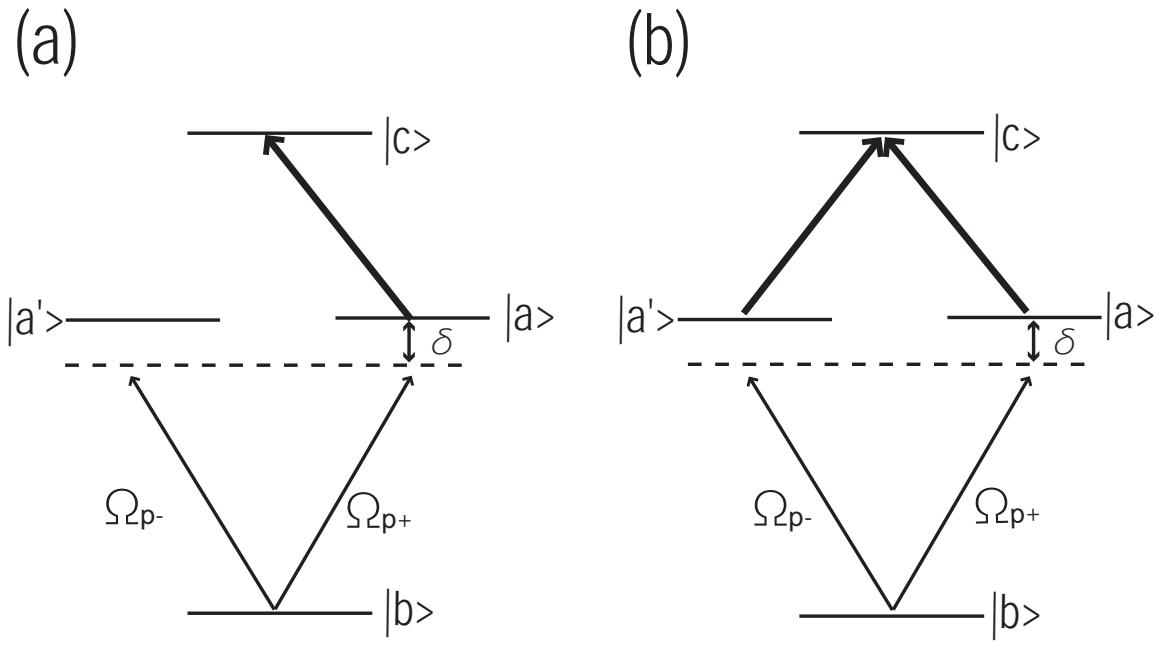

Fig. 14. Energy diagram of condition: (a) r=0, EIT (Ω_{p+}) + two-level systems (Ω_{p-}) (b) r=1, double-EIT system ($\Omega_{p\pm}$).

Ω_{d-} are resonant with their respective transitions, shown in Fig. 14 (a). The steady-state solution of Eqs. (4.1) and (4.2) for the two probe transitions can be reduced to

$$\rho_{ab} = \Omega_{p+} \underbrace{\frac{i(2\Gamma + i\delta)}{|\Omega|^2 + (\gamma + i\delta)(2\Gamma + i\delta)}}_{ladder\ \ EIT}, \tag{4.5}$$

$$\rho_{a'b} = \Omega_{p-} \underbrace{\frac{i}{\gamma + i\delta}}_{two-level}. \tag{4.6}$$

Equation (4.5) shows a typical solution for EIT in ladder configuration, and Eq. (4.6) shows a typical solution for a two-level system. These Eqs. (4.5) and (4.6) show that the strong drive field (Ω) only interacts with the coupled probe field (Ω_{p+}), and it obviously has no effect to the uncoupled probe transition $\rho_{a'b}$. Because the

density-matrix solutions for the probe transitions are obtained from the first-order expansion of the weak probe field, the high order terms of the weak probe interaction are ignored. Therefore, even the weak probes couple to a common ground state, and the first-order expansion solutions still show that there is no interference between the two weak fields.

For the r=1, Δ=0 condition (four fields are present) the amplitude of the weak probe fields are the same ($\Omega_{p\pm}$=Ω_p), the amplitudes of the drive fields are also the same ($\Omega_{d\pm}$=Ω), and the drive fields are resonant with their respective to transitions, and probes have the same detuning, shown in Fig. 14 (b). Under such conditions, the coherence terms for the two probe transitions are the same (ρ_{ab}=$\rho_{a'b}$) and can be expressed as

$$\begin{aligned}
\rho_{ab} &= \Omega_p\{\underbrace{\frac{i[|\Omega|^2+(\gamma+i\delta)(2\Gamma+i\delta)]}{(\gamma+i\delta)[2|\Omega|^2+(\gamma+i\delta)(2\Gamma+i\delta)]}}_{one\ photon\ term} \\
&\quad \underbrace{-\frac{i|\Omega|^2}{(\gamma+i\delta)[2|\Omega|^2+(\gamma+i\delta)(2\Gamma+i\delta)]}}_{three\ photon\ term}\} \\
&= \Omega_p\{\underbrace{\frac{i(2\Gamma+i\delta)}{2|\Omega|^2+(\gamma+i\delta)(2\Gamma+i\delta)}}_{double-EIT}\}. \qquad (4.7)
\end{aligned}$$

Equation (4.7) shows that ρ_{ab} is a linear combination of a one-photon term and three-photon term, and the form of Eq. (4.7) is similar to the solution of ladder EIT shown in Eq. (4.5). Eq. (4.7) shows the EIT for both probe channels, and the four fields form a double-EIT in a symmetric double-ladder configuration. We find that the denominator of Eq. (4.7) is larger than the denominator of Eq. (4.5) while the numerator for these two equations are the same, which means the transparency of the two probe in double-EIT condition is better than the transparency in ladder-EIT

condition. To explore the underlying physics, we analyze the role of the $\Lambda_{ab}^{(1)}$ and $\Lambda_{ab}^{(3)}$ terms in the imaginary part of ρ_{ab} under EIT in ladder configuration and the double-EIT in a symmetric double-ladder configuration, shown in Fig. 15. In Fig. 15 (a), the $\Lambda_{ab}^{(1)}$ for ladder-EIT shows minimum absorption while the weak probe and the strong drive are present. The large transmission of the probe field can be understood as due to creation of a dark state between state $|c\rangle$ and $|b\rangle$ created by the drive field Ω_d and probe field Ω_{p+} [28, 38]. By then applying another strong drive Ω_d coupling state $|a'\rangle$ and $|c\rangle$ to form double-EIT in a double-ladder configuration, the original dark state is perturbed by the additional drive field which leads to increase of the resonant one photon absorption. Since the coherence terms for both probe transitions are the same, the probe in the orthogonal polarization state also has the same absorption. However, the absorbed population from the probe in the orthogonal polarization state is optically pumped to the state $|c\rangle$ which is then coherently transferred to state $|a\rangle$ via the resonant three photon $\chi^{(3)}$ process. The increase of one photon absorption in the $\Lambda_{ab}^{(1)}$ of double-EIT can be over compensated by the gain from the resonant $\chi^{(3)}$ process, shown in Fig. 15 (b). Therefore, the double-EIT in the symmetric double-ladder configuration has better absorption suppression than ladder-EIT at all resonant condition, shown in Fig. 15 (c).

We also calculate the normalized transmission of the output probe field by using Eqs. (4.3) and (4.4) for the above ladder-EIT and double-EIT conditions, shown in Fig. 16. The calculations also show that the probe in the double-EIT configuration has higher transmission and broader transmission linewidth than the EIT in ladder configuration.

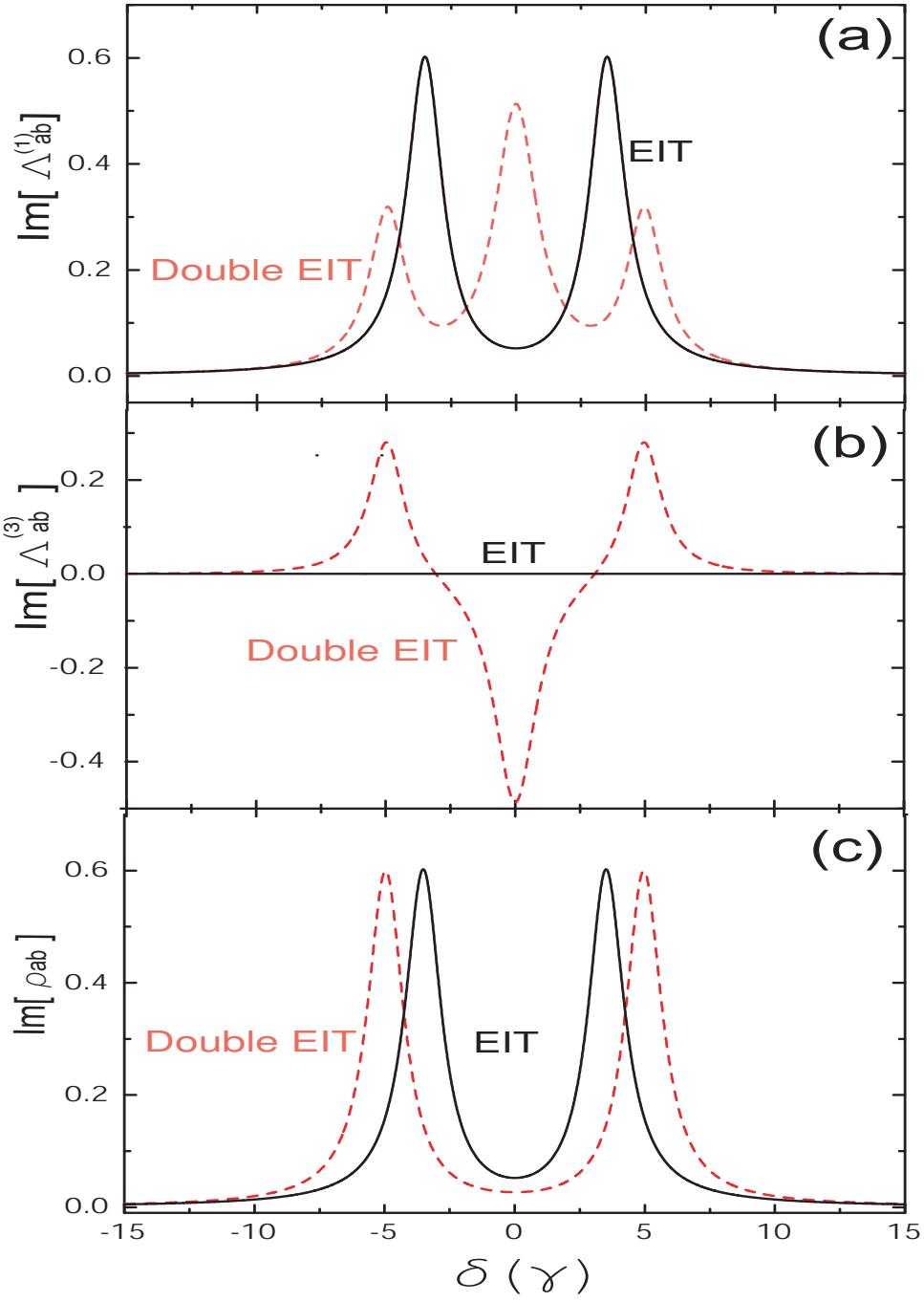

Fig. 15. Plot to show the absorption Im ρ_{ab} vs δ for EIT and double EIT in the double-ladder configuration. (a) Im $\Lambda^{(1)}_{ab}$(b) Im $\Lambda^{(3)}_{ab}$ (c) Im ρ_{ab}. $\Omega_{p\pm}$=0.2, $\Omega_{d\pm}$=3.5 for double EIT and Ω_{p+}=0.2, Ω_{d-}=3.5 for ladder-EIT, Δ=0. All the frequencies scale in with γ.

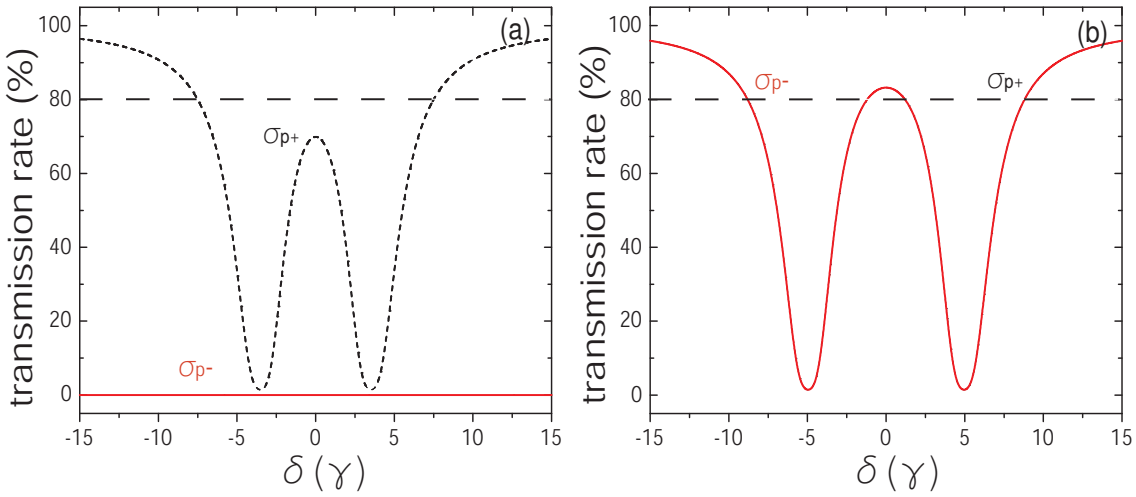

Fig. 16. The graph (a) and (b) are, respectively, the calculated probe transmission spectra with the parameters of (a) Ω_{p+}=0.2, Ω_{d-}=3.5, Δ=0 (b) $\Omega_{p\pm}$=0.2, $\Omega_{d\pm}$=3.5, Δ=0, η=0.05. All the frequencies scale in with γ.

C. Experimental results

Our main experimental results, shown in Fig. 17(a) and (b), demonstrate the enhancement of the transmission signal of double-EIT in a double-ladder configuration compared to EIT in the ladder configuration. In Fig. 17(a), the strong drive field σ_{d-} is resonant with its respective transition and the weak probe σ_{p+} is tuned near the resonance. While the probe σ_{p+} is resonant with the drive field, the normalized probe transmission reaches a maximum of ~73% due to the EIT in the ladder configuration [38]. By then applying an additional probe σ_{p-} and drive σ_{d+} with the same field intensity as the σ_{p+} and σ_{d-}, respectively, to form double-EIT in a symmetric double ladder configuration. The transmission spectrum for the probe $\sigma_{p\pm}$ are almost the same due to the symmetric configuration for the probe field. We discover that the maximum normalized transmission of the probe field in the double-EIT system is increased to ~81%. We also note that the linewidth of probe transmission spectrum

of the double-EIT is 10 MHz broader than the linewidth in ladder-EIT system. The experimental results of the probe transmission enhancement qualitatively agree with our theoretical prediction calculated by Eqs. (4.3) and (4.4). The broader probe spectrum of double-EIT system is due to power broadening of $8^2S_{1/2}$(F=4) energy levels by the the two strong drive fields $\sigma_{d\pm}$ [56].

Although the data qualitatively agree with our theoretical calculations, we cannot accurately fit our experimental data. To do so, we would need to consider the multilevel system and residual Doppler broadening effect. Besides, the pump and probe fields are tightly focused into the 5 cm long cell. So the fields are nonuniform inside the atomic medium. Hence it is very difficult to convert the power of the field into the Rabi frequency [38].

To date, the simple four-level double-ladder system has been experimentally realized by complicated multilevel system with Rb [39, 42, 57] and Cs [58, 59]. However, the experimental results can only qualitatively agree with the theoretical calculation. Quantitative agreement between theory and experiment is still not achieved, particularly under the condition when two strong drives in different orthogonal polarizations are applied. Because the experimental results are contributed from multilevel systems, the double-ladder, Y and inverted-Y configurations all need to be considered into theoretical calculation. From our experiment, we found that the multilevel system is dominated by the double-ladder system. However, to quantitative fit our experimental results, the other two systems should be also included into our calculations. A detailed discussion for the study of the role of Y and inverted-Y systems in our experiment will be discussed elsewhere.

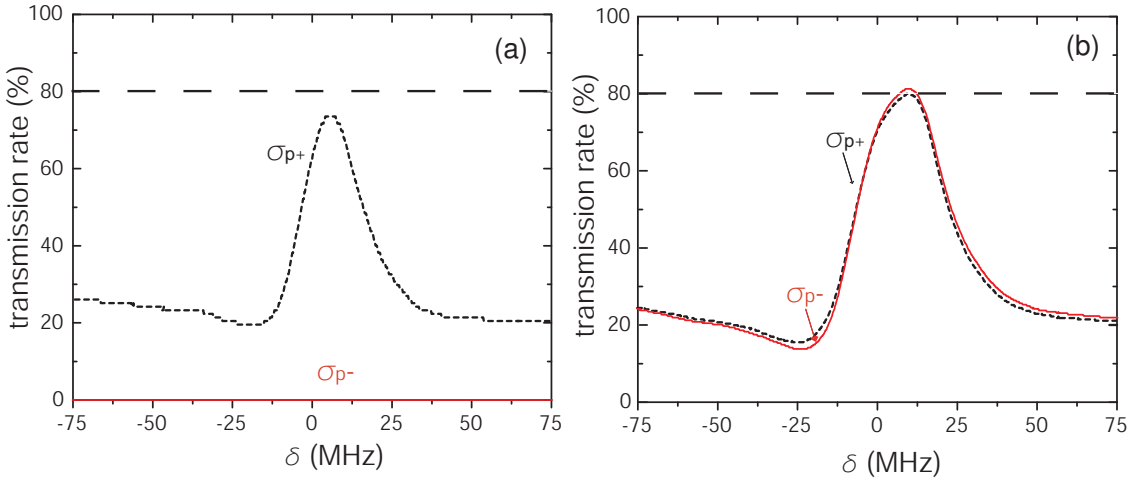

Fig. 17. Measured probe transmission vs probe detuning δ for the (a) ladder-EIT condition at probe σ_{p+} power 1 μW and coupling drive σ_{d-} power 29 mW (b) double-EIT condition at probe power 1 μW for both $\sigma_{p\pm}$ and coupling drive 29 mW for both $\sigma_{d\pm}$, atomic density N=3x10^{10} cm^{-3}.

D. Summary

To conclude, we have theoretically studied the enhancement of probe transparency of double-EIT in the double-ladder system. We have shown that this enhancement is due to the large resonant $\chi^{(3)}$ effect. We have presented a proof-of-principle experiment that is in conformity with our theoretical calculation.

CHAPTER V

WIDTH OF ELECTROMAGNETICALLY INDUCED TRANSPARENCY RESONANCE IN ATOMIC LADDER SYSTEM

Coherence preparation by lasers of atomic media and quantum interference in the amplitudes of optical transitions, have made revolutionary changes in many well-studied nonlinear process such as parametric- and second-harmonic generation as well as four-wave mixing [59, 60, 61, 62]. The efficiency of these process can be very high at extremely low input power [25]. Electromagnetically induced transparency (EIT) plays a key role in these nonlinear processes. EIT has also been proposed to various different applications, for example, gain and lasing without inversion [63, 64], small and compact atomic clocks [65] and the storage of quantum information [66, 67].

The EIT resonance is one of the important results of atomic coherence that can be easily measured experimentally. The study of the EIT width leads to better understanding of the influence of different processes on the atomic coherence [7, 68]. Among them the are relaxation and collisional rates [69], spontaneous transfer of coherence [70], radiation trapping [71], and Doppler broadening.

The linear behavior [72, 73, 74] and nonlinear [75] behavior of the EIT width in a lambda configuration on the laser drive field has been experimentally and theoretically studied in recent years. However, the EIT width in a ladder configuration has only been theoretically discussed in Ref [38]. In this chapter, we present an experimental study of ladder-EIT width in Doppler-broadened Cs vapor for a wide range of intensities of the drive field. From our measurement, we find good qualitative agreement between the theory and experiment. However, the residual Doppler width in the system is 3 times less than the theoretical prediction in Ref [38].

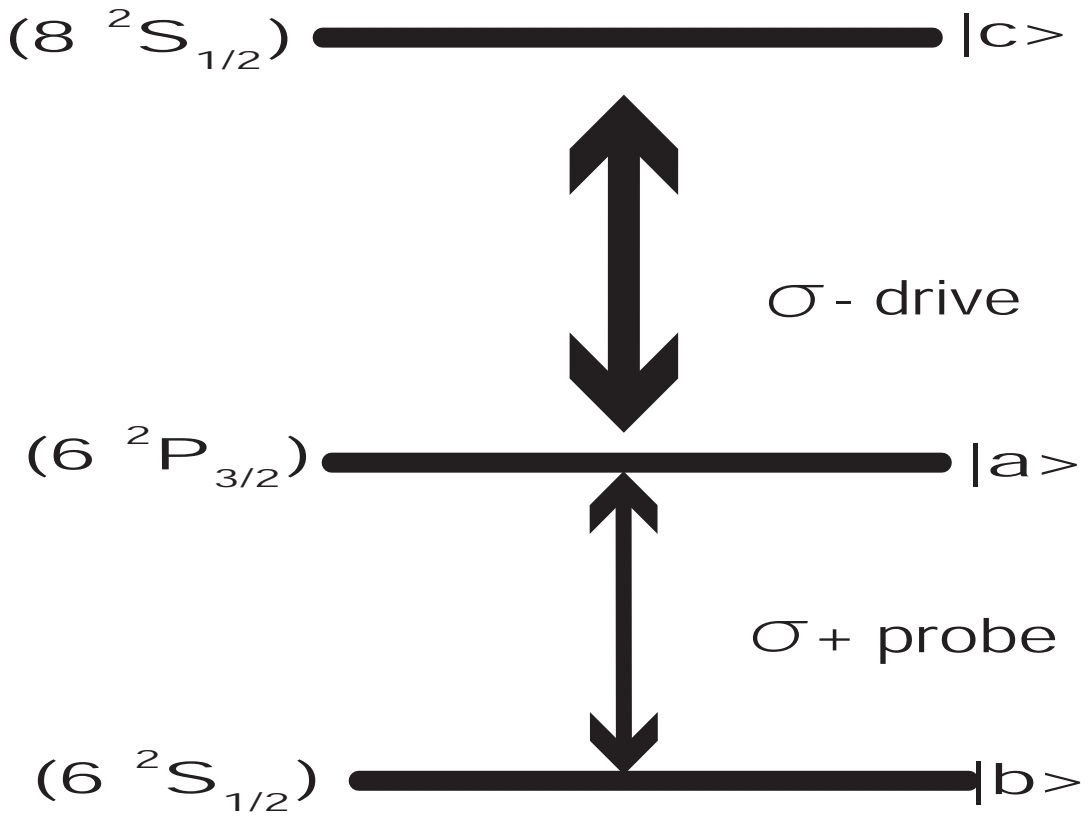

Fig. 18. The energy level diagram

A. Experimental setup

Our three-level ladder system is experimentally realized by a Cs atom vapor cell with the energy levels shown in Fig. 18. The probe laser is tuned near the $6^2S_{1/2}$(F=4)$\rightarrow$ $6^2P_{3/2}$(F$'$=5) D2 transition at a wavelength 852.2 nm, and drive field is tuned near the $6^2P_{3/2}$(F$'$=5)$\rightarrow$ $8^2S_{1/2}$(F=4) transition at a wavelength 794.3 nm. The experimental setup is shown in Fig. 28. The length of the Cs vapor cell is 5 cm and it is placed inside a two-layer magnetic shield to suppress the laboratory magnetic field. The density of Cs vapor is controlled by the temperature of the cell. The transition of drive field is driven by a single frequency (linewidth of 500 KHz) Ti:sapphre laser and the laser beam is focused to a spot size of 500 μm. The probe transition is

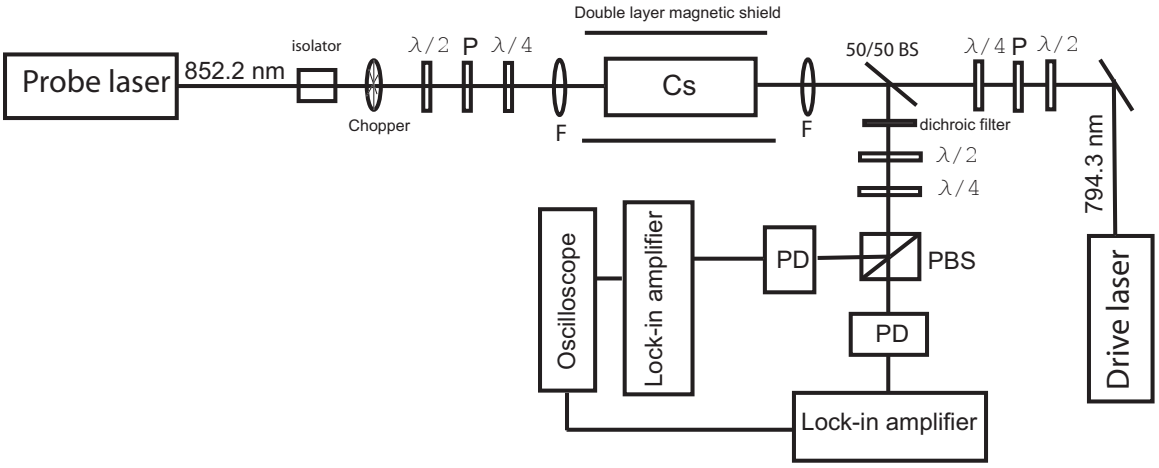

Fig. 19. The experimental diagram

driven by a external cavity diode laser(ECDL) focused to a spot size 200 μm. Two photon Doppler cancellation is achieved with counterpropagating probe and drive beams. The transmitted probe beam is separated with a 50/50 beam splitter and then measure by a photodetector.

B. Analysis and experimental results

If the drive σ_{d-} and probe σ_{p+} both are resonant with respective to their transitions, the transmission of the probe is maximum, shown in Fig. 20. It is a typical EIT condition [38], and the large transmission is due to the creation of a dark state between states $|b\rangle$ and $|c\rangle$ by the probe and drive field. The medium polarization of probe field $\mathcal{P} = N\rho_{ab}$, where the N is atomic density and ρ_{ab} is the density element of the probe transition. To obtain the medium polarization, we calculate ρ_{ab} [20]

$$\rho_{ab} = \Omega_p \frac{i(\Gamma + i(\delta + \Delta))}{|\Omega_d|^2 + (\Gamma + i(\Delta + \delta))(\gamma + i\delta)}, \tag{5.1}$$

where $\gamma(\Gamma)$ is the radiative decay for the probe(drive) transition, δ (Δ) is the frequency detuning for probe (drive) field. Equation (5.1) is the solution for the steady state,

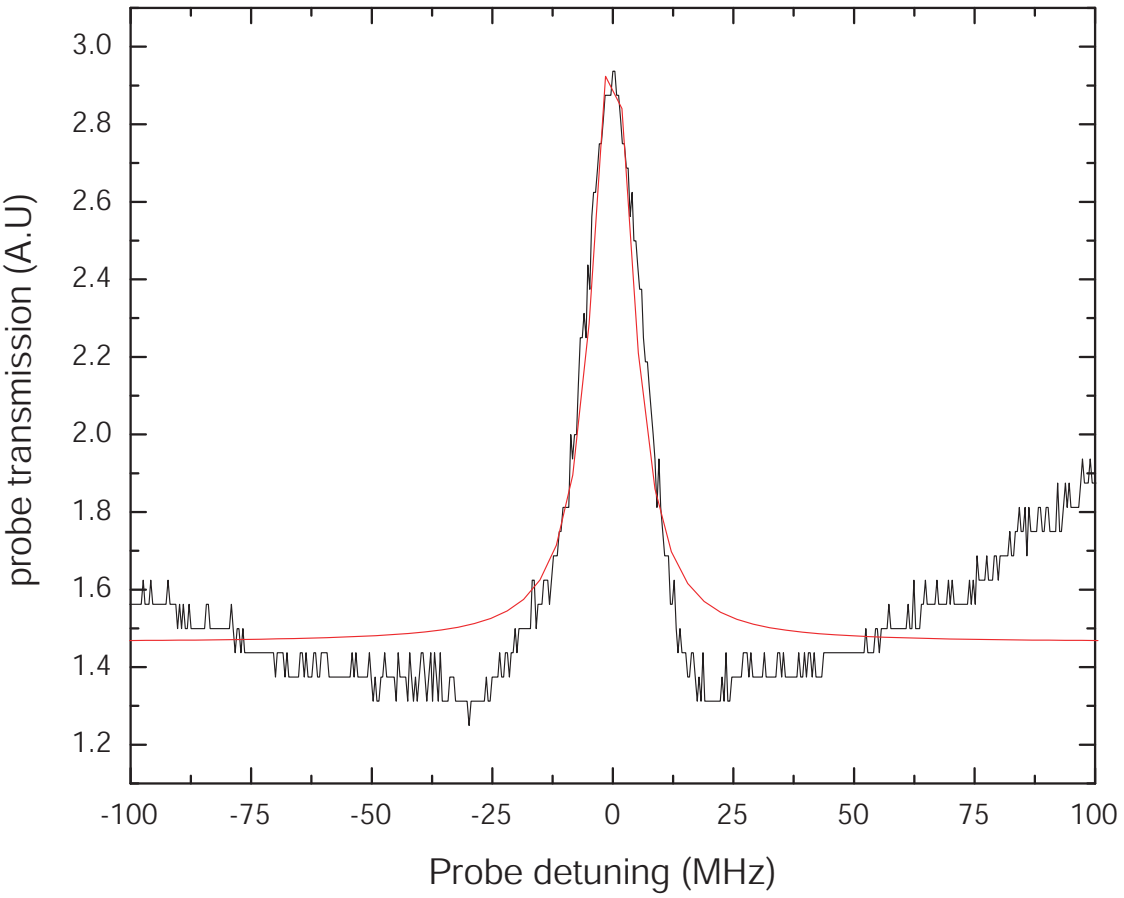

Fig. 20. The probe transmission is a function of detuning at atomic density N=2.6x10^{10}cm^{-3}. The drive power is 15 mW and input probe power is 1 μW. The red line is Lorentzian fitting.

and the Doppler effect is not included. To give a more clear picture, the full expression for the Doppler broadened susceptibility in our system corresponding to the probe field is given by

$$\rho_{ab} = \Omega_p \frac{i(\Gamma + i(\delta_v + \Delta_v))}{|\Omega_d|^2 + (\Gamma + i(\Delta_v + \delta_v))(\gamma + i\delta_v)}, \tag{5.2}$$

where, $\Delta_v = \Delta + \vec{k}_d \cdot \vec{v}$ and $\delta_v = \delta - \vec{k}_p \cdot \vec{v}$, $\vec{v}$ is the velocity of atom, and $\vec{k}_p$ ($\vec{k}_d$) is the wavevector of probe (drive) field. As the wavelengths of the probe (852.2 nm) and drive (794.3 nm) are very different, the residual two-photon Doppler term $(\vec{k}_d - \vec{k}_p) \cdot \vec{v}$ is still significantly large in the resonant ladder configuration. Therefore, the contribution of residual Doppler broadening to the EIT linewidth is not negligible.

The EIT linewidth Γ_{EIT} in the ladder configuration can be simply written as

$$\Gamma_{EIT} = \frac{|\Omega_d|^2}{\gamma} + \Gamma + \delta W_d, \tag{5.3}$$

where the W_d is the residual Doppler broadening. For a purely Doppler-broadened medium, the full width at half maximum of the absorption profile is [38]

$$W_d = \frac{2w_p}{c} u\sqrt{ln2}. \tag{5.4}$$

Where w_p is the probe frequency, c is light speed and u is the atomic velocity. The residual Doppler width of the two photon transition with wavelength mismatching condition is [38]

$$\delta w_d = W_d(\frac{w_p - w_d}{w_p}), \tag{5.5}$$

where w_d is drive frequency.

We experimentally studied the lineshape of the EIT resonance for various drive power. Fig. 20 shows a good Lorentzian fit for the EIT lineshape profile. Therefore, the EIT linewidth can be obtained from the Lorentzian fitting. The measured EIT linewidth is linearly dependent on the drive power, shown in Fig. 21. When the drive

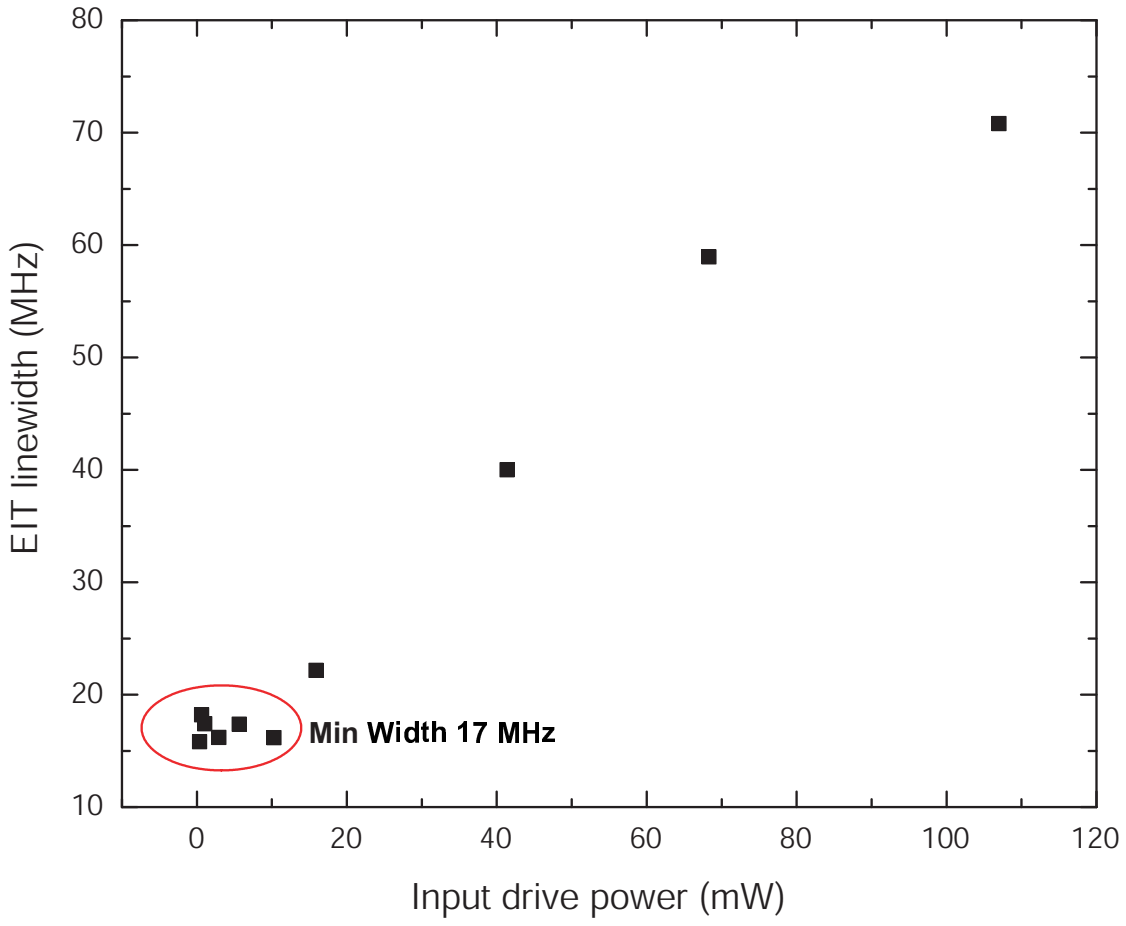

Fig. 21. Drive power vs the EIT spectra linewidth at the atomic density N=2.6x10^{10}cm^{-3} and input probe power 1 μW.

power is below 5 mW, the EIT linewidth is saturated at 17 MHz. The minimum Γ_{EIT} obtained from the experiment is only the sum of δW_d and Γ, and the power broadening term $|\Omega_d|^2$ is negligible due to $|\Omega_d|^2 \ll \gamma$. However, the theoretical residual Doppler δW_d calculated by Eqs. (5.4) and (5.5) is $\sim$ 45 MHz, which is 2.5 times larger than the EIT linewidth measured from our experiment. In this dissertation, we report this result and a further detailed theoretical explanation will be discussed elsewhere.

CHAPTER VI

MEASUREMENT OF GROUND-STATE DECOHERENCE VIA INTERRUPTION OF COHERENT POPULATION TRAPPING

A. Introduction

Coherent control is usually limited by the coherence lifetime, which is the inverse of the dephasing rate. For improving the ability to control atomic polarization coherently, it is important to know the value of various decoherence rates. A lambda-system, having two ground states coupled to a common excited state by lasers can generate a coherent eigen (dark)-state that is transparent to the incoming fields and, hence, suppresses fluorescence from the excited state. However, ground-state dephasing perturbs the dark state, leading to an increase in fluorescence. In this chapter, we theoretically study the role of ground-state coherence on the the fluorescence from the excited state in a lambda system under continuous-wave excitation. From our analytical calculations, we suggested the use of this strong dependence of fluorescence on the ground-state dephasing as a new method for measuring ground-state dephasing rates. The theory and a proof-of-principle experiment using ^{87}Rb vapor are given.

The outline of this chapter as follows: brief review for dephasing measurement methods in Sec. II. We describe the system and derive dynamical equation in Sec. III. In Sec. IV, we present numerical results to show how the excited-state population is affected due to interruption of coherent population trapping(CPT) by ground-state decoherences. We also derive an analytical formula to understand the numerical result, and also to demonstrate the possibility of measuring various ground-state decoherence rates. In Sec. V, we present the results of a proof-of-principle experiment using a ^{87}Rb vapor cell with results that are in good agreement with the theory.

Finally, we summarize and conclude in Sec. VI.

B. Brief introduction for dephasing measurement methods

A popular method for determining the dephasing of the ground states is via Raman scattering because the linewidth of the scattering process is determined by the effective decay of the coherence between the initial and final states [76]. Similar information can be obtained from coherent anti-Stokes Raman scattering (CARS) [77] because the CARS lineshape is related to the Raman lineshape [78, 79, 80]. All this typically assumes pump and probe fields so that the resulting physical process is described by the third order susceptibility. Compared to conventional Raman scattering, CARS is capable of high spectral resolution. However, it is limited by a stringent phase matching requirement. In what follows, we show how coherent population trapping (CPT) [6] can be used for the determination of the dephasing rates.

Further, the method we propose also enables one to determine the nonradiative rates which might come about from thermally stimulated processes [81]. As is well known, a dark state forms when no decay processes other than radiative decay are considered [20]. However, the dark state starts becoming bright due to nonradiative processes. Clearly the interruption of the dark state could be a sensitive method of studying nonradiative processes. This is reminiscent of studies in interferometry where the interferometer is tuned to a dark fringe. It has been observed in an earlier study that CPT is also very sensitive to internal parameters of the atom such as spontaneous emission linewidths [82].

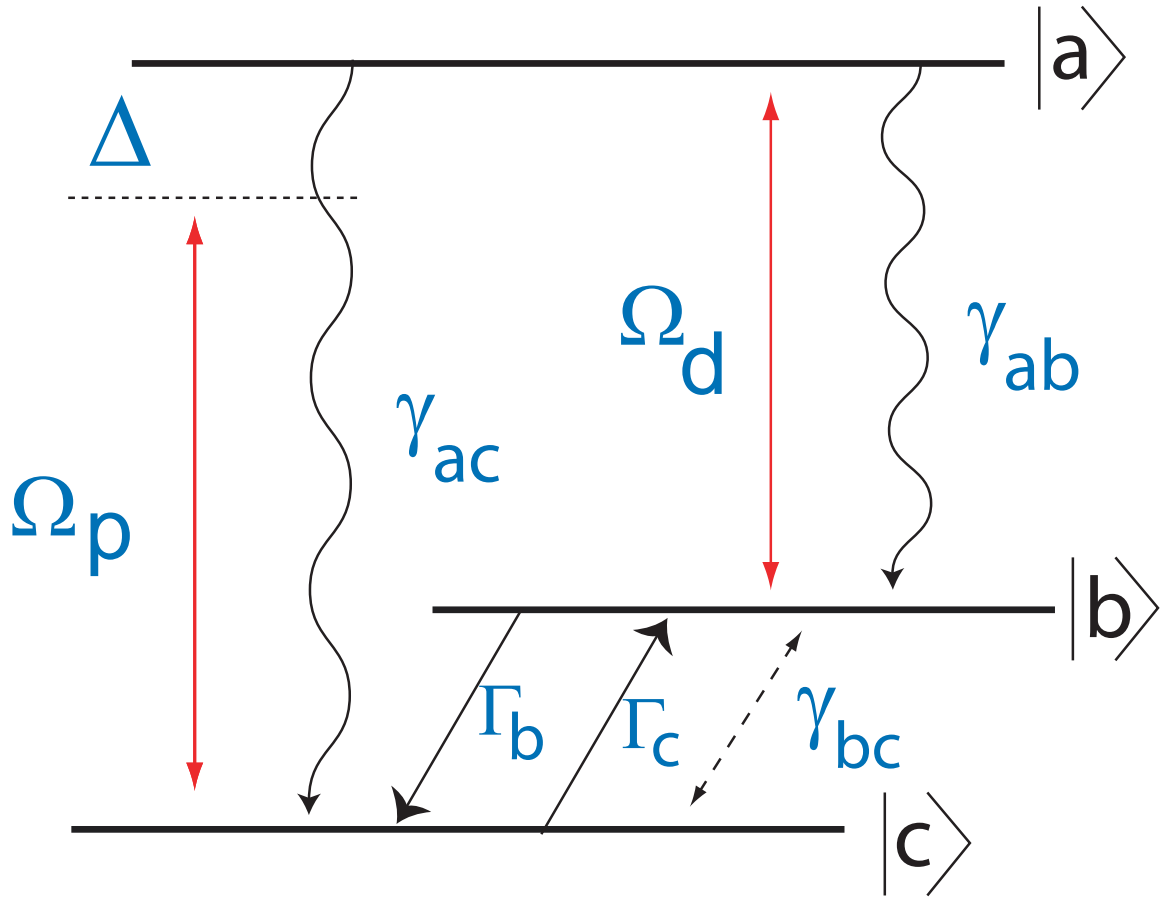

Fig. 22. A three level lambda system with ground state coherence dephasing γ_{bc} and also non-radiative decays Γ_b and Γ_c in the ground state. The spontaneous decay from $a \leftrightarrow b$ ($a \leftrightarrow c$) is given by γ_{ab} (γ_{ac}). The pump field Ω_p is detuned by Δ from the $a \leftrightarrow c$ transition and the drive field Ω_d is on resonance with the $a \leftrightarrow b$ transition.

C. The system and the dynamics

We consider a three level lambda system having all various possible decays such as coherence dephasing γ_{bc} and non-radiative decays Γ_b and Γ_c. The source of coherence dephasing can be due to collisions in gas cells [83] or phonon induced in solids [84], and the non-radiative decays could be incoherent pumpings between the ground states via thermal excitations in gas cells (particularly when the ground states are degenerate or near degenerate) or crystal field induced decays [81]. Two lasers couple the two ground states with the excited state. The pump (drive) laser couples the $a \leftrightarrow c$ ($a \leftrightarrow b$) transition with a Rabi frequency $2\Omega_p = \wp_{ac}E_p/\hbar$ ($2\Omega_d = \wp_{ab}E_d/\hbar$). Here $\wp_{ij} = \langle i|\wp|j\rangle$ represents the dipole moment corresponding to the $|i\rangle \leftrightarrow |j\rangle$ transition. In the following we briefly outline the derivation of dynamical equations.

The interaction Hamiltonian in the *rotating wave approximation* (RWA) can be written as [20]

$$\mathcal{H}_I = -\hbar\Omega[r|a\rangle\langle c|e^{-i\omega_p t} + |a\rangle\langle b|e^{-i\omega_d t} + \text{H.c.}] \tag{6.1}$$

where ω_p (ω_d) represents the central frequency of the pump (drive) field. We use the notation $r = \Omega_p/\Omega_d$ and $\Omega_d = \Omega$. The unperturbed Hamiltonian for this system (shown in Fig. 22) can be written as

$$\mathcal{H}_0 = \hbar\omega_{ac}|a\rangle\langle a| + \hbar\omega_{bc}|b\rangle\langle b| \tag{6.2}$$

where $\hbar\omega_{ij}$ is the energy separation between the states $|i\rangle \leftrightarrow |j\rangle$. The equation of motion for the lambda system is given by the density matrix equation

$$\frac{\partial\rho}{\partial t} = -\frac{i}{\hbar}[\mathcal{H}_0 + \mathcal{H}_I, \rho] + \text{decay terms.} \tag{6.3}$$

Next we make the following transformation $\rho \rightarrow \tilde{\rho}$ to eliminate the rapid temporal

oscillations

$$\begin{aligned} \rho_{ab} &\rightarrow \tilde{\rho}_{ab} \exp[-i\omega_d t] \\ \rho_{ac} &\rightarrow \tilde{\rho}_{ac} \exp[-i\omega_p t] \\ \rho_{bc} &\rightarrow \tilde{\rho}_{bc} \exp[-i(\omega_p - \omega_d)t] \\ \text{and } \rho_{ii} &\rightarrow \tilde{\rho}_{ii} \,. \end{aligned} \tag{6.4}$$

Thus the equations for the density matrix elements with natural decay, ground state dephasing and non-radiative decay rates are

$$\begin{aligned} \frac{\partial \rho_{aa}}{\partial t} &= -2(\gamma_{ab} + \gamma_{ac})\rho_{aa} + i\Omega\rho_{ba} - i\Omega^*\rho_{ab} + ir\Omega\rho_{ca} \\ &\quad -ir^*\Omega^*\rho_{ac} \\ \frac{\partial \rho_{ab}}{\partial t} &= -(\gamma_{ab} + \gamma_{ac} + \Gamma_b/2)\rho_{ab} - i\Omega(\rho_{aa} - \rho_{bb}) \\ &\quad +ir\Omega\rho_{cb} \\ \frac{\partial \rho_{ac}}{\partial t} &= -(\gamma_{ab} + \gamma_{ac} + \Gamma_c/2 + i\Delta)\rho_{ac} + i\Omega\rho_{bc} \\ &\quad -ir\Omega(\rho_{aa} - \rho_{cc}) \\ \frac{\partial \rho_{bb}}{\partial t} &= -\Gamma_b\rho_{bb} + \Gamma_c\rho_{cc} + 2\gamma_{ab}\rho_{aa} - i\Omega\rho_{ba} + i\Omega^*\rho_{ab} \\ \frac{\partial \rho_{bc}}{\partial t} &= -(\gamma_{bc} + (\Gamma_b + \Gamma_c)/2 + i\Delta)\rho_{bc} + i\Omega^*\rho_{ac} - ir\Omega\rho_{ba} \\ \frac{\partial \rho_{cc}}{\partial t} &= -\Gamma_c\rho_{cc} + \Gamma_b\rho_{bb} + 2\gamma_{ac}\rho_{aa} - ir\Omega\rho_{ca} + ir^*\Omega^*\rho_{ac} \,. \end{aligned} \tag{6.5}$$

Here Γ_b (Γ_c) is the non-radiative decay from state b to c (c to b), $2\gamma_{ij}$ are the decay rates from $|i\rangle \rightarrow |j\rangle$, γ_{bc} is the dephasing rate of the Raman coherence and Δ is the pump field detuning (see Fig. 22). In the following section we solve the above dynamical equation to determine how fluorescence is affected by all these decay rates.

D. Results and discussions

We have numerically solved Eqs. (6.5) and plotted the steady state excited state population ρ_{aa} in Fig. 23. This depicts how the fluorescence from the atom depends on pump field detuning. We see that when both fields Ω_b and Ω_c are on resonance, the population reaches minimum for a zero dephasing rate γ_{bc} and non-radiative decay rates Γ_b and Γ_c. This is clearly due to CPT. However for finite γ_{bc} and $\Gamma_b = \Gamma_c = \Gamma$, the CPT is perturbed and hence population from the dark state (anti-symmetric superposition of ground state) partially transfers to the bright state (symmetric superposition of the ground states). Thus the excited state gets populated by its coupling to the bright state and hence starts fluorescing. In what follows, we will show how this significant variation in the fluorescence signal at resonance could be used to measure the ground state decoherence rates.

To isolate the roles of ground state dephasing and non-radiative decay we have plotted ρ_{aa} in Fig. 23(A) assuming the non-radiative decay $\Gamma_b = \Gamma_c = 0$, and in Fig. 23(B) we have shown the excited state population when only non-radiative decay is present but $\Gamma_{bc} = 0$. Clearly, γ_{bc} affects the fluorescence only around resonance as it only disturbs the coherence created in the ground state. As a result, some population is made available at the bright state to couple to the excited state via the laser field and hence start fluorescing. Clearly for larger γ_{bc}, we find stronger fluorescence at $\Delta = 0$. However, the non-radiative decays affect the fluorescence profile even for the wide off-resonant field because Γ_b and Γ_c incoherently mix populations in the ground state in addition to causing ground state decoherence.

To understand the above argument, we have calculated ρ_{aa} analytically for both resonant and off-resonant cases in the limit of intense lasers. In the following we present the solutions with non-radiative decay between ground states included in the

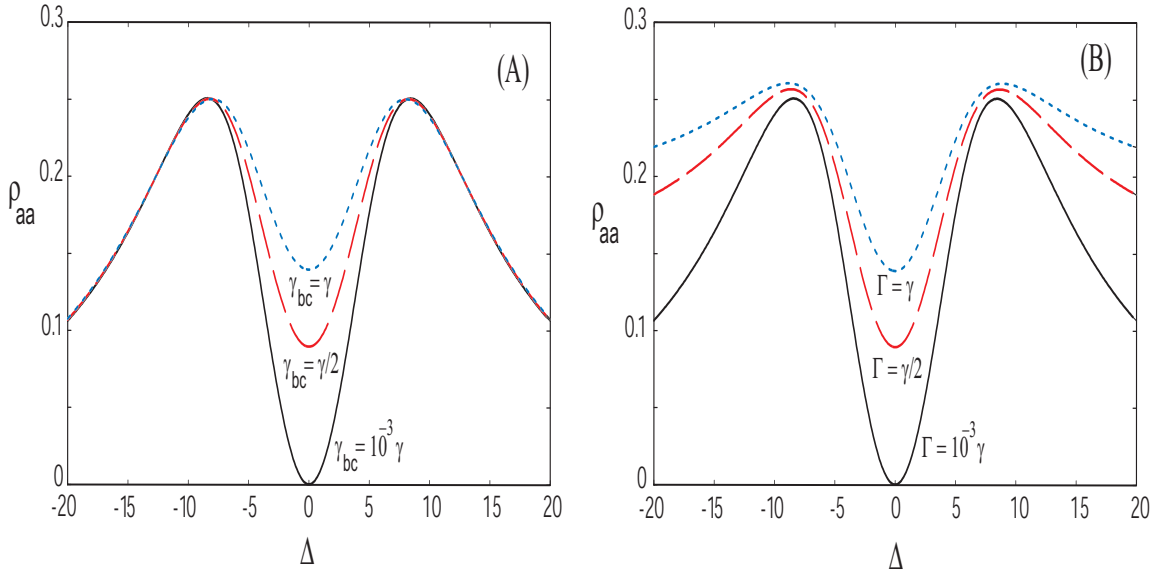

Fig. 23. The excited population for various values of ground state dephasing γ_{bc} and non-radiative decays Γ_b and Γ_c. The dependence of two decays are illustrated in (A) $\Gamma_b = \Gamma_c = \Gamma = 0$ and (B) $\gamma_{bc} = 0$. In all the plots, we have assumed $\gamma_{ab} = \gamma_{ac} = \gamma$, the laser Rabi frequency $\Omega = 5\gamma$ and $r = 1$.

calculation, and assuming that $\Omega \gg \gamma_{ab}, \gamma_{ac}, \gamma_{bc}, \Gamma_b, \Gamma_c$. For $r = 1$ and $\Gamma_b = \Gamma_b = \Gamma$, $\gamma_{ab} = \gamma_{ac} = \gamma$, the steady state solution of Eq. (2.14) for the off-resonant pump laser ($\Delta \neq 0$) is obtained as

$$\rho_{aa} = \frac{A_1(4\Omega^4 A_2 + \Delta^4\Gamma) + \Delta^2\Omega^2\{4\gamma A_1 + 2\Gamma(2\gamma + \gamma_{bc}) + 3\Gamma^2\}}{A_1\{4\Omega^4(3A_2 + 4\gamma) + \Delta^4 A_3\} + \Delta^2\Omega^2\{2A_3(4\gamma + A_2) + 3\Gamma^2\}} \tag{6.6}$$

where

$$A_1 = 4\gamma + \Gamma, \;\; A_2 = \Gamma + \gamma_{bc}, \;\text{ and }\; A_3 = 2\gamma + 3\Gamma. \tag{6.7}$$

This analytical result agrees very well with the numerical result presented above. Clearly in Fig. 23(A), the value of ρ_{aa} at resonance (i.e., $\Delta = 0$) is given by $\rho_{aa} \equiv \gamma_{bc}/(3\gamma_{bc} + 4\gamma)$. For $\gamma_{bc} \ll \gamma$, the excited state population under the condition of CPT depends linearly on γ_{bc}, i.e., $\rho_{aa} \approx \gamma_{bc}/(4\gamma)$. Similarly, in Fig. 23(B), ρ_{aa} at $\Delta = 0$ is

given by $\rho_{aa} = (\Gamma_b + \Gamma_c)/[3(\Gamma_b + \Gamma_c) + 8\gamma]$.

Further we get a more general result for the resonant pumping. Again, we have considered strong pump and drive lasers but $r \neq 1$ ($\Omega_p \neq \Omega_d$). We could even keep unequal non-radiative decays between the ground states $\Gamma_b \neq \Gamma_d$. The solution for this case is obtained as

$$\rho_{aa} = \frac{\Gamma_b r^4 + 2\gamma_{bc} r^2 + \Gamma_c}{\Gamma_b(1 + 2r^4) + \Gamma_c(2 + r^4) + 6\gamma_{bc} r^2 + 2\gamma(1 + r^2)^2} \,. \tag{6.8}$$

Assuming there is no coherence dephasing in the system (i.e., $\gamma_{bc} = 0$), the above expression reduces to that obtained in Ref. [80]. For $r = 1$, the above equation further simplifies to

$$\rho_{aa} = \frac{2\gamma_{bc} + \Gamma_b + \Gamma_c}{3(2\gamma_{bc} + \Gamma_b + \Gamma_c) + 8\gamma} \,. \tag{6.9}$$

This matches exactly with the numerical results presented above. Next, in Fig. 24 we show a numerical plot of how ρ_{aa} varies with the change in ratios of the intensities r^2, when both the fields are on resonance. These plots match perfectly with the above analytical result. It should be noted that these analytical results also hold well for $r = 0$ as long as Ω is assumed to be strong.

Equation (6.8) is very important, as it can be written as a linear equation in terms of the decoherence rates γ_{bc} , Γ_b and Γ_c , given by

$$\kappa_1 \Gamma_b + \kappa_2 \Gamma_c + \kappa_3 \gamma_{bc} + \kappa_0 = 0 \tag{6.10}$$

where

$$\begin{aligned} \kappa_1 &= (1 + 2r^4)\rho_{aa} - r^4, \quad \kappa_2 = (2 + r^4)\rho_{aa} - 1 \\ \kappa_3 &= 2r^2(3\rho_{aa} - 1), \quad \text{and} \quad \kappa_0 = 2\gamma(1 + r^2)^2 \rho_{aa} \,. \end{aligned} \tag{6.11}$$

The coefficients κ_i are functions of measurable quantities such as the ratio of inten-

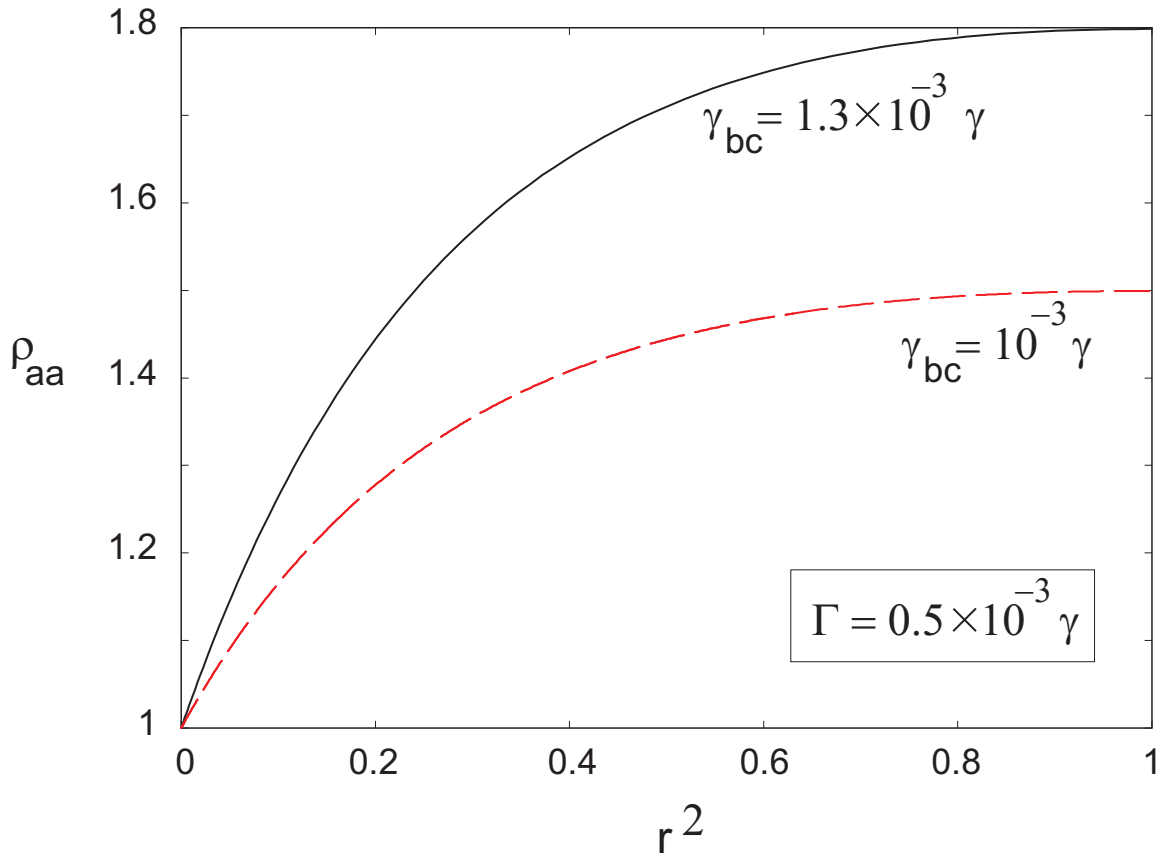

Fig. 24. Plot of normalized ρ_{aa} with respect to their values at $r = 0$ vs the intensity ratio r^2. Here $\gamma_{ab} = \gamma_{ac} = \gamma$ and $\Omega = 5\gamma$. Both pump and drive fields are on resonance here.

sities (r^2) of the two applied fields and the excited state population which is proportional to the fluorescence intensity. In an experiment, that would mean we need three values of ρ_{aa} for different r^2 to determine all three ground state decoherence rates. In this spirit, we can observe in Fig. 24 that indeed ρ_{aa} depends very strongly on γ_{bc} and Γ_i $(i = b, c)$. In the plot we have normalized the ρ_{aa} with their corresponding values at $r = 0$.

It may be noted that this method should be valid for varieties of systems having the generic model of a three-level lambda scheme. Some possible systems of interest could be atoms in a buffer gas [85], molecules doped in solid [86, 87, 88, 89], or multilevel quantum dots [90, 91].

E. The experiment

In this section we present the results of a proof-of-principle experiment that agrees qualitatively with the above discussions. At the end of this section we discuss in detail some limits in implementing the exact idea in ^{87}Rb gas.

The experimental setup is shown schematically in Fig. 25. An external cavity diode laser (ECDL) is tuned to the $5S_{1/2}(\mathrm{F} = 2) \rightarrow 5P_{1/2}(\mathrm{F} = 1)$ transition of the Rb D_1 line. The laser linewidth is about 100 kHz. The laser beam is split into two by a 50/50 beam splitter, the polarization of one of the beams is rotated by a $\lambda/2$ wave plate, and these two orthogonal linearly polarized beams are then combined with a polarizing beam splitter(PBS). After the combined beam passes through $\lambda/4$ wave plate, the beam is a combination of two orthogonal circularly polarized components. These components couple two Zeeman ground state sublevels to the single excited state as shown in Fig. 25b. Thus compared to the model in Fig. 22, the right-circular polarization component would correspond to Ω_p and the left-circular polarization

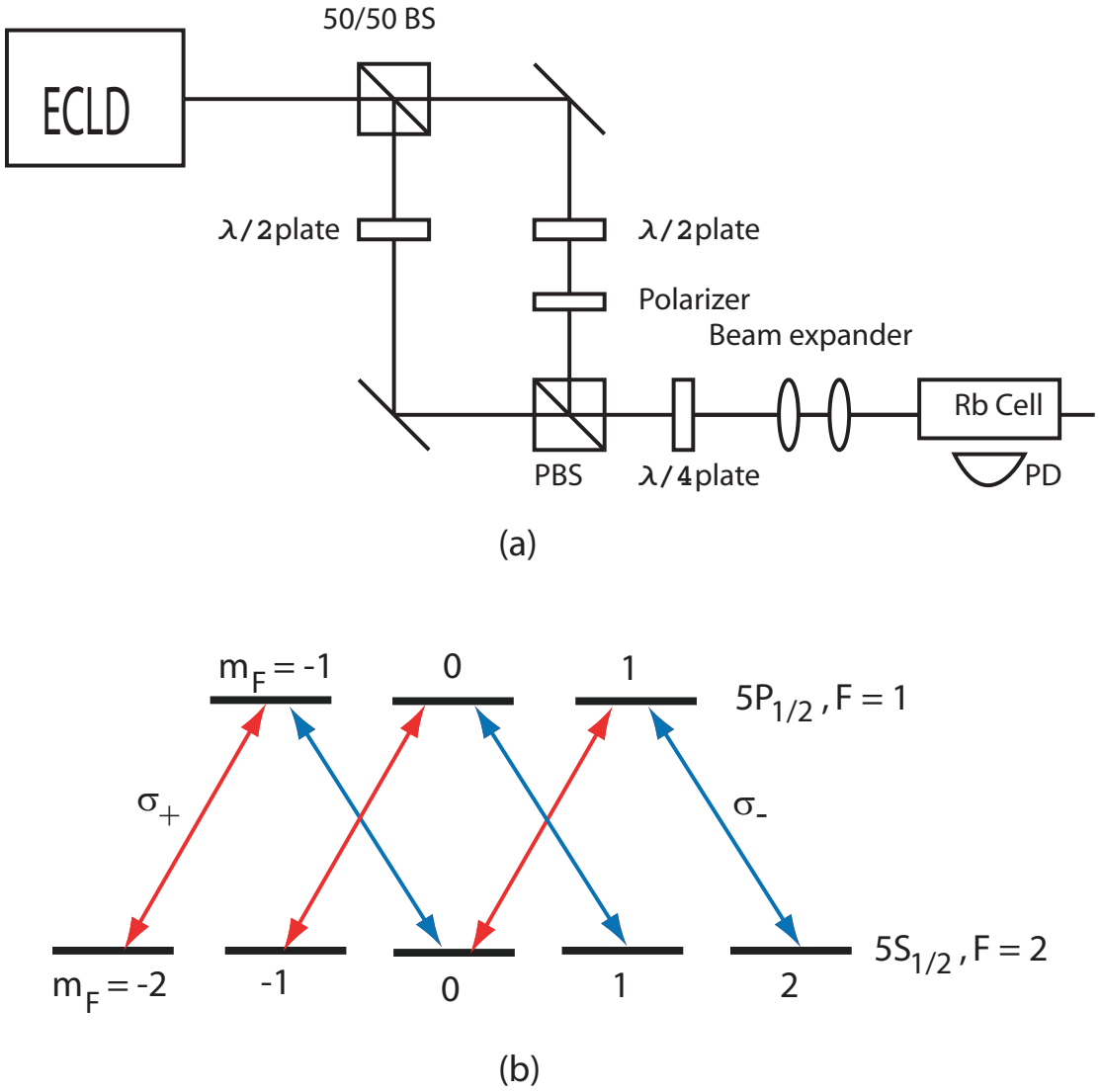

Fig. 25. (a) Schematic diagram of the experimental setup: ECDL, external cavity diode laser; BS, beam splitter; PBS, polarized beam splitter; PD, photodiode detector. The experimental set up to detect the fluorescence as a function of intensity ratio r^2. (b) The hyperfine Zeeman sublevel transitions of ^{87}Rb under consideration.

component would correspond to Ω_d. The intensity for the left- and right-circular polarization components can be attenuated by placing polarizers after the $\lambda/2$ wave plate. The laser beam diameter can be controlled with a telescope beam expander. The beam then passes through a cylindrical glass cell of length 10 cm containing rubidium vapor. At room temperature, the Rb density is approximately 8×10^9 cm^{-3}.

The laser power in each beam at the entrance of the Rb cell is approximately 3 mW. The fluorescence signal is registered with an Amplified Si Detector (PDA55) with 10 MHz frequency bandwidth. Fluorescence is detected at the side of the cell, perpendicular to the laser propagation direction. Care is taken to minimize residual scattered light from the glass wall of the cell. To compensate for this scattered light, the signal is measured when the laser is detuned far away from resonance so there is no fluorescence, and this background is subtracted from the fluorescence signal. In the experiment, we measure the fluorescence emission from the excited state for various ratios of intensities r^2. To minimize the experimental uncertainty, we fix the intensity of the left circular polarized component Ω_d as the reference beam and only varied the intensity for the right circular component Ω_p .

The different laser beam diameters D give rise to different ground state dephasing rates because the thermally moving atoms spend more time on the average in a larger beam. Coherence is lost when the atoms collide with the walls, and thus in a larger beam one would expect a lower rate of dephasing collisions. So the maximum coherence time (and so the minimum γ_{bc}) is determined by the laser beam diameter. We present here data sets for two different values of D. Since the total number of atoms contributing to the fluorescence changes with the beam diameter, we have normalized the fluorescence signals by their corresponding values at $r = 0$. Further, the number of atoms in the interaction region for a given beam diameter is same for both $r = 0$ and $r \neq 0$. Thus, the normalized fluorescence becomes independent of

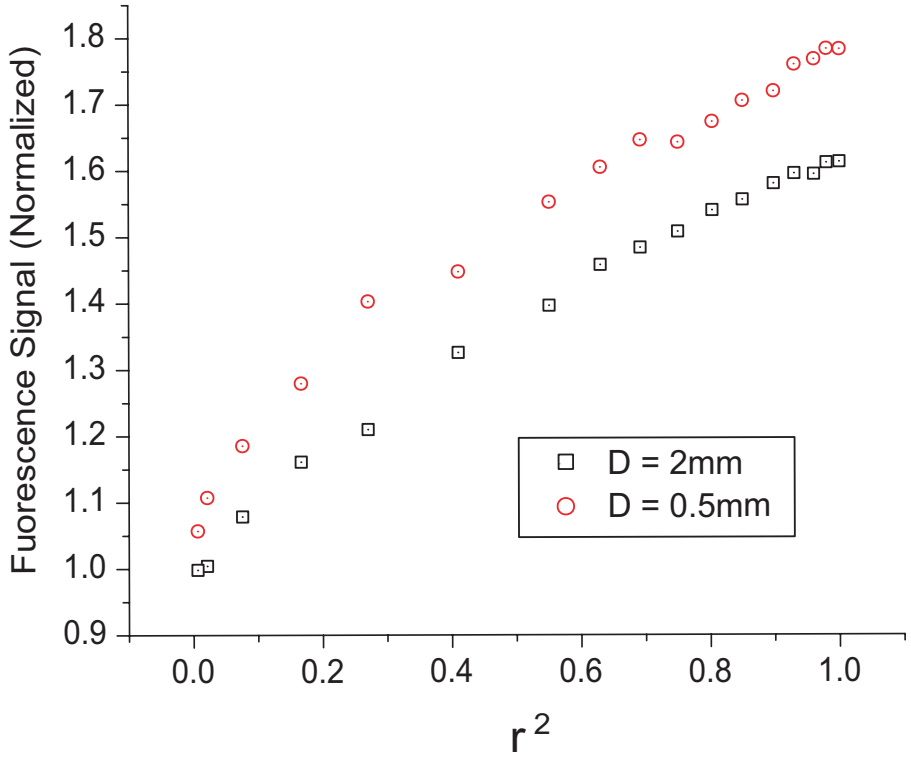

Fig. 26. Experimental fluorescence data (normalized with their corresponding $r = 0$) under CPT versus the intensity ratio r^2. A larger value for beam diameter D would result in smaller γ_{bc}.

number of atoms participating in the fluorescence. The results are shown in Fig. 26. These agree qualitatively with the behavior shown in Fig. 24 calculated from the three level model.

Although the data agree qualitatively with the analytical calculations, we cannot derive accurate values for the dephasing rates. To do so, we would need to extract ρ_{aa} from the data which would require calibrating the measured fluorescence to the total fluorescence from the atoms. One way of performing this calibration would be to incoherently pump the excited state and detect the fluorescence with a detector of known efficiency. However such pumping in ^{87}Rb would also excite the other upper (or lower) hyperfine components. (The upper $5P_{1/2}(\mathrm{F}=2)$ state considered here is only 800 MHz from the $5P_{1/2}(\mathrm{F}=1)$ state, and only partially resolved due to the inhomogeneous Doppler broadening of 500 MHz). Therefore, our theory would be exact for systems having reasonably isolated ground and excited states.

It may also be noted that the model system for the theoretical calculation given in Sec. III corresponds to a closed system. However, the proof-of-principle experiment on ^{87}Rb gas cell corresponds to an open system. It has been observed that the CPT resonance strongly depends on the strength of the driving field in an open system [92]. It is well known that the population loss in the cell due to finite time of flight of the gaseous atoms through the interaction region (laser beam) contributes as an additional effective ground state dephasing rate [93, 94], though the dynamic population itself is not affected as much [1]. The aforsaid underlying principle, thus, remains same for both closed and open systems in the determination of the collisional dephasing rate, except that one has to account for the finite time of flight of gas atoms. The average

[1]The effect of time of flight in the open system is discussed in the appendix C.

time of flight can be determined as

$$t_{\text{flight}} = D\sqrt{\frac{3k_BT}{M_a}}, \tag{6.12}$$

where D is the diameter of the laser beam, T is the temprature of the cell, M_a is mass of the atom and k_B is the Boltzmann constant. Therefore, the actual value of the collisional dephasing rates in gas cell would be given by subtracting $(t_{\text{flight}})^{-1}$ from the experimentally measured value of the ground state dephasing.

F. Summary and conclusion

We have examined the role of ground state decoherence rates on the fluorescence in a resonant three level lambda system. We have shown that the fluorescence is strongly affected by the ground state decoherence due to interruption of the coherent population trapping. We have theoretically demonstrated how to exploit this sensitivity to measure ground state decoherence rates including the non-radiative decays via an analytical solution. We have presented a proof of principle experiment that is in conformity with our theoretical calculation. We have noted that this method should work well for a wide variety of systems.

CHAPTER VII

NONLINEAR MAGNETO-OPTIC POLARIZATION ROTATION WITH INTENSE LASER FIELDS

A. Introduction

There is interest in improving the sensitivity of polarization spectroscopy measurements [95, 96], both for fundamental reasons and for practical reasons such as optical magnetometry [97]. The sensitivity of optical pumping magnetometers (OPMs) has already achieved $10^{-9}\mathrm{G}/\sqrt{\mathrm{Hz}}$ under laboratory conditions [98, 99]. In such devices, the Zeeman level shift measurements are based on light absorption [94], but the sensitivity is limited if the absorption is strong. Scully and Fleischhauer et al. [100, 101] proposed a high-sensitivity optical magnetometer based on electromagnetic induced transparency (EIT) where the high dispersion at an EIT resonance can dramatically improve the sensitivity of magnetic field measurements by suppression of the absorption via quantum interference.

We describe nonlinear magneto-optic polarization rotation as follows. Consider two circularly polarized electromagnetic waves near atomic resonance in a Λ configuration as shown in Fig. 27. When the two frequencies are in Raman (two-photon) resonance, a "dark-state" is created that is associated with electro-magnetically induced transparency [6, 28]. The atoms are optically pumped into a coherent superposition of ground-state Zeeman sublevels that is accompanied by very steep dispersion. This dispersion gives rise to such effects as enhanced index of refraction [100, 102] and ultra slow light [13, 14, 15]. Therefore, even a small shift of magnetic sublevels can result in a large change in the refractive indices for the two circular components, so that they acquire different optical phase shifts after traversing the length of the cell.

This phase difference results in rotation of the polarization of linear polarized light exiting the cell with respect to the direction it entered with. This effect is known as nonlinear magneto-optical rotation (NMOR). If $\chi_+(\chi_-)$ represents the susceptibility of the birefringent medium corresponding to the right (left) circular component of the probe, the rotation angle, for small absorption, is given by

$$\phi = \pi k_p l(\chi_- - \chi_+) \tag{7.1}$$

where k_p corresponds to the propagation vector of the probe and l is the length of the medium along the direction of propagation.

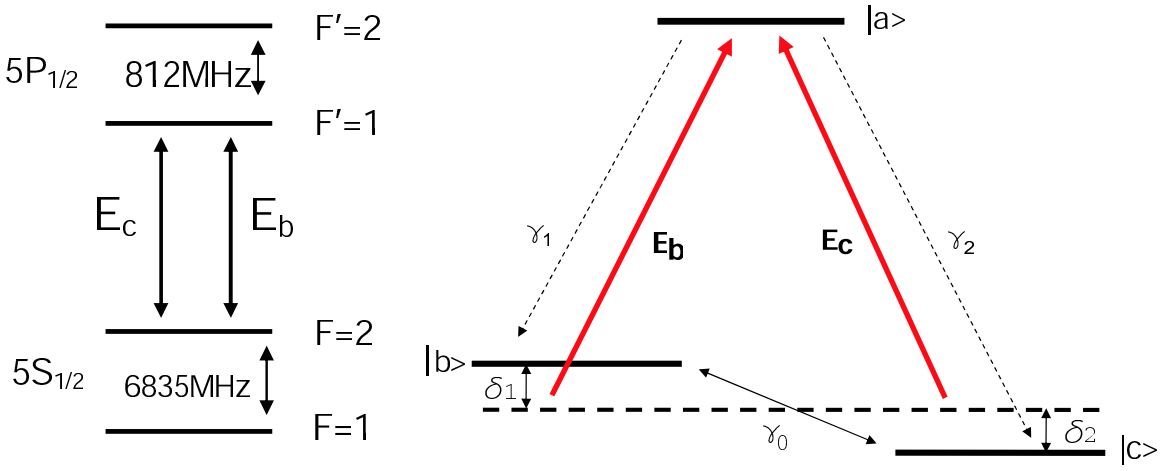

Fig. 27. Simplified three level Λ diagram for experimental condition

The use of NMOR for magnetometry in optical thin and thick media has been extensively studied [103, 104, 105]. This work shows that the ground state coherence dephasing plays an important role in decreasing sensitivity. Various methods have been used to reduce the dephasing rate such as high-quality anti-relaxation walls [98, 104] and buffer gas [103]. These methods can effectively increase the lifetime of ground-state coherence, greatly improving magnetic field sensitivity. For example, Ref. [104] demonstrates sensitivity of 3×10^{-12} G/$\sqrt{\text{Hz}}$. Further high-sensitivity

work has been done using optical pump-probe magnetometry [106, 107].

The usual limit on the smallest Zeeman level shift that can determined is from the signal-to-noise ratio. It was pointed out by Fleischhauer et al. [101] that the limit of the detectable magnetic field shift is determined by two fundamental restrictions: photon counting error, due to the vacuum fluctuation of the laser field (shot noise), and coupling the laser field to nonresonant levels (ac-Stark shifts). Compensation of ac-Stark shifts has been studied experimentally [108]. Based on the shot noise limit the smallest detectable magnetic field δB_z, has been written as [104]

$$\delta B_z = \frac{1}{\sqrt{N_{ph}}}(\frac{\partial \phi}{\partial B_z})^{-1}. \tag{7.2}$$

where N_{ph} is the number of photons counted.

Shot noise can be reduced by increasing the laser intensity, but this results in broadening of the EIT resonance which decreases the polarization rate. Ref. [101] proposed that the sensitivity of an optical magnetometer could be improved by simultaneously increasing both laser-field intensity and atomic density. This approach was studied for a limited range of laser intensity in [103]. However, it is found that radiation trapping effects limit the polarization rotation by introducing a new type of dephasing [71].

In this dissertation, we show that there is an optimal intensity and density for the system to achieve the ultimate shot-noise-limited magnetic field sensitivity. The outline of the chapter is as follows: The experimental setup and results are presented in Sec. II. We describe our system, derive dynamical equations and show our numerical results in Sec. III. The analysis for our experimental measurements and summary in Sec. VI and Sec. V, respectively.

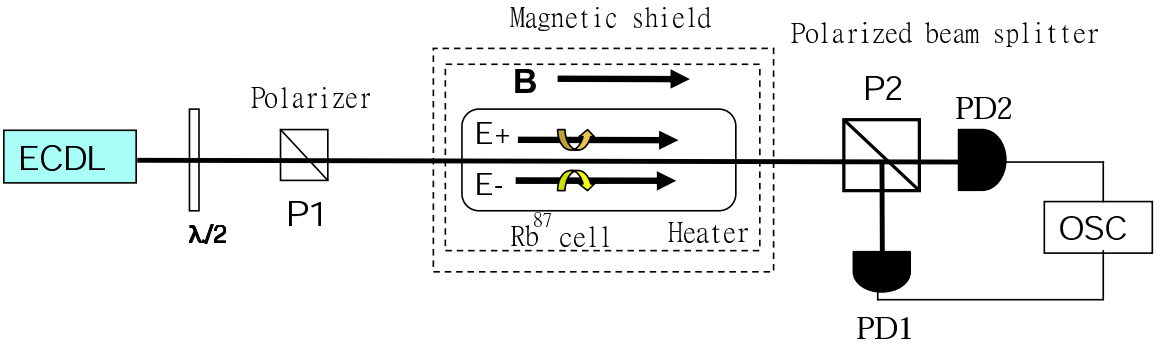

Fig. 28. Diagram showing the experimental setup

B. Experimental setup and measurement

Our experimental setup is shown in Fig. 28. A Topica DLX 110 high-power tunable single mode diode laser is tuned to the transition 795 nm $5S_{1/2}\,(F{=}2) \rightarrow 5P_{1/2}\,(F'{=}1)$ transition of the rubidium D_1 line, shown in Fig. 27. The laser propagates through a high quality polarizer P_1 which produces linear polarization, then through a cylindrical glass cell of length $L = 5.0$ cm and diameter $D = 2.5$ cm containing isotopically enhanced Rb^{87}. The laser power can be accurately controlled by a polarizer with a half-wave plate. To control the beam diameter, a beam expander may be placed after the polarizer. The atomic density of Rb^{87} is controlled by the temperature of the coldest spot of the cell, which is installed in a temperature controlled double layer magnetic shield. A longitudinal magnetic field is created by a solenoid installed inside the inner magnetic shield. A polarization analyzer P_2 is placed after the cell and titled 45 degrees with respect to the polarizer. Photodiodes PD1 and PD2 detect the light from both channels of the analyzer, allowing simultaneous measurements of the polarization rotation angle ϕ and transmitted laser power.

In our experiment we consider the effect of different laser beam diameters and on different intensities of the laser. Because there is no buffer gas or wall coatings in our cell, changing the beam diameter changes the amount of time which the atoms interact

with the laser (time of flight), and therefore changes the ground state dephasing rate γ_0. Increasing the beam diameter leads to a smaller ground state dephasing rate and should enhance the ground state coherence resulting in better sensitivity.

Figure 29 shows the experimental rotation rate as a function of density for two different beam diameters (d = 2 mm and d = 4 mm) and different laser intensities. The polarization rotation rate $d\phi/dB$ is obtained by measuring the polarization rotation for very small changes of magnetic field, such that small changes in the polarization rotation are proportional to small changes in magnetic field. The individual curves show that for a fixed intensity, the rotation rate increases with density, reaches a maximum value, and rolls off rapidly with increasing density. The maximum value increases with intensity. This tendency of the individual curves has been explained [71]. However, the overall profiles of the rotation rate for larger intensities and densities from the linear region($\Omega \leq \gamma$) to the nonlinear region($\Omega >> \gamma$) has not been previously explored.

For each value of the intensity, there is therefore a density where the rotation rate is maximum. Figure 30(A) shows the maximum rotation rate as a function of intensity for the two different beam diameters used above. The inset shows the density for which the maximum rotation rate is reached as a function of intensity. We can relate the maximum rotation rate to magnetic field sensitivity with Eq. (7.2). This calculated sensitivity is shown in Fig. 30(B). We see that the sensitivity improves (drops) as the intensity is increased, but reaches a limiting value. The limiting value is improved by increasing the beam diameter (and increasing the interaction time of the atoms with the laser). It is important to note that each point (each different intensity) is measured at the density for which the rotation rate is maximum.

These data demonstrate the interplay of increasing rotation rate and increased transmission on the sensitivity calculated by Eq. (7.2). From our measurements we

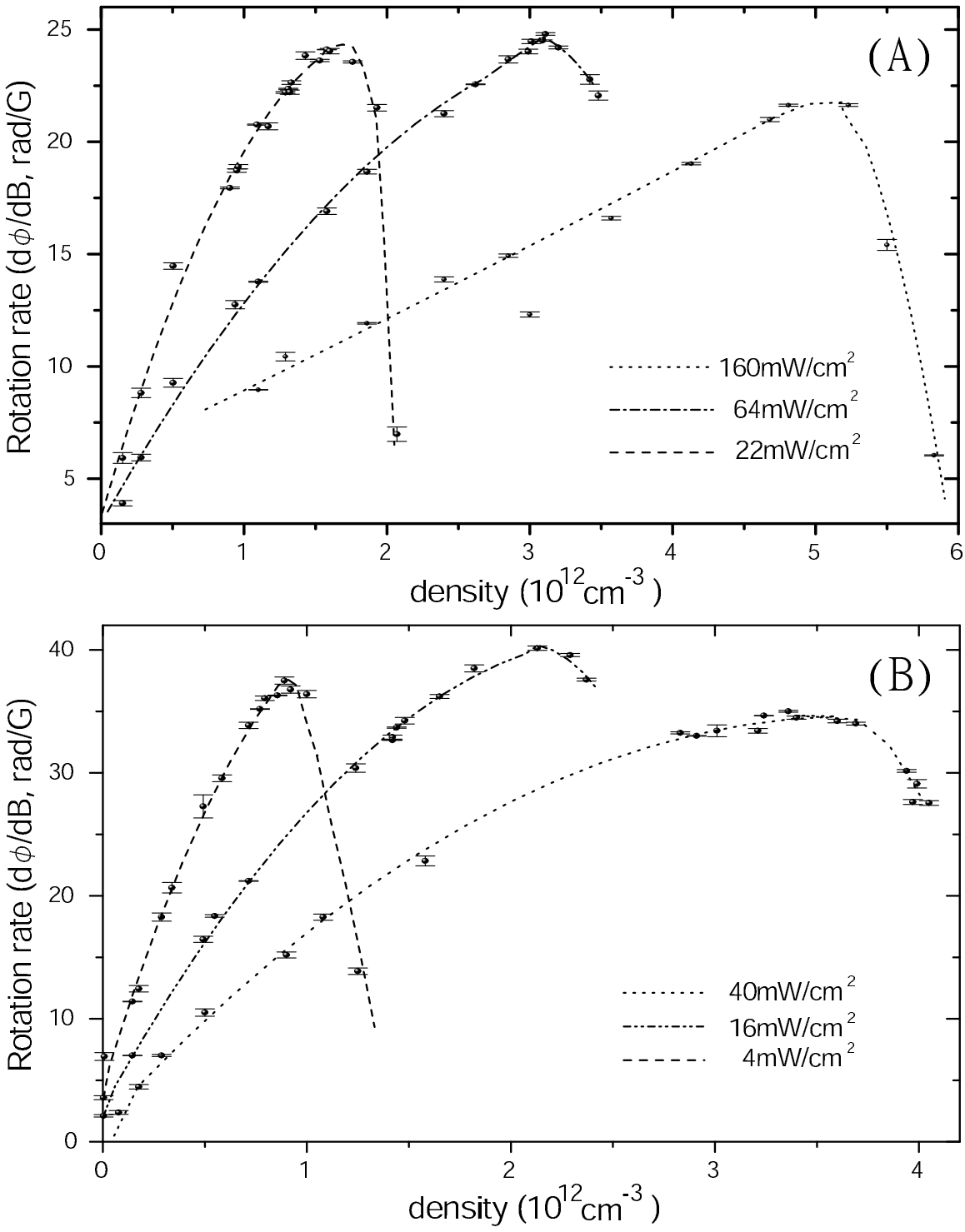

Fig. 29. Rotation rate dϕ/dB due to the nonlinear Faraday effect as a function of atomic density for the beam diameter (A) $d = 2$ mm and (B) $d = 4$ mm for different intensities. Dashed lines are guides.

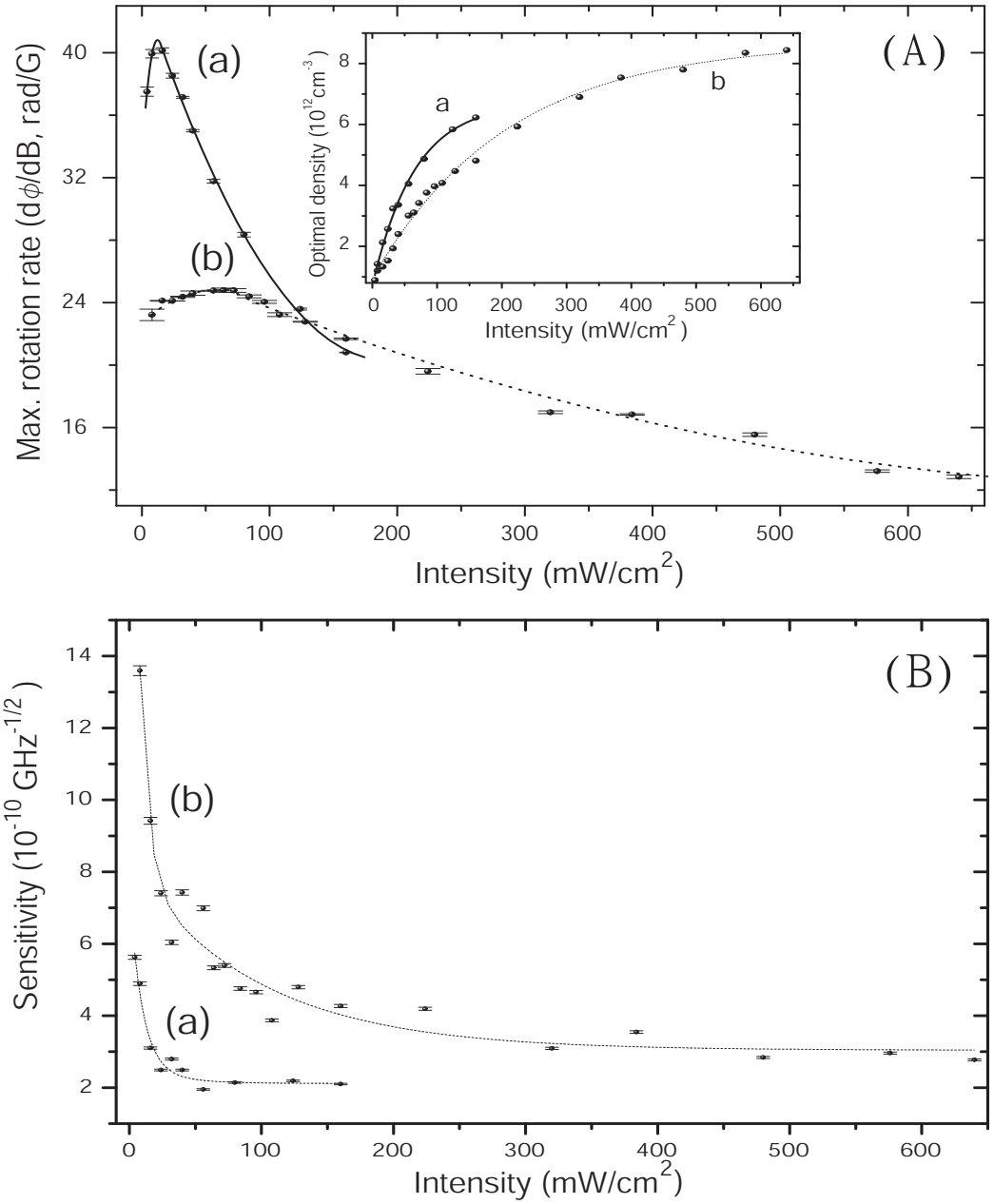

Fig. 30. (A) Maximum rotation rate as a function of laser intensity. The inset shows the density corresponding to the maximum rotation rate. Curve (a) is for $d = 2$ mm beam diameter and curve (b) is for $d = 4$ mfm. (B) Calculated sensitivity for the maximum rotation rate data. Dotted and dashed lines are guides.

find that the maximum rotation rates for different intensities are observed when the transmission is around 2 to 5%. However, the density for which we calculate optimal sensitivity corresponds to a much higher transmission. This is shown in Fig. 31 for the rotation data with $I = 64$ mW/cm^2 and diameter $d = 2$ mm. The inset shows the transmission for this same condition. We clearly see that the optimum sensitivity does not occur at the same point as the maximum rotation rate. In other words the two factors of Eq. (7.2) optimize at different densities. For our data, the optimal sensitivity occurs on the order of $\simeq 50\%$ transmission. Figure 31(B) shows the optimal sensitivity for each intensity at their optimal densities. Both optimal sensitivity curves for different beam diameters are saturated when the light intensities for $d = 2$ mm ($d = 4$ mm) beam diameters are greater than 128 mW/cm^2 at atomic density 0.9×10^{12} cm^{-3} (56 mW/cm^2 at atomic density 1.58×10^{12} cm^{-3}).

C. System and dynamics

In this section we theoretically investigate the saturation of the rotation rate $\partial\phi/\partial B$ and also the sensitivity δB_z. We consider a monochromatic field $\vec{E}(z,t)$ with field polarization along $\hat{e}$

$$\vec{E}(z,t) = \hat{e}\mathcal{E}(z)\mathrm{e}^{ikz-i\omega t} + \text{c.c.} \tag{7.3}$$

propagating inside a medium consisting of atoms having a three level scheme as shown in Fig. 27. Here $\mathcal{E}(z)$ is the field amplitude and k corresponds to the propagation constant with central frequency ω. The propagation of the field along the z-direction in the medium is governed by the Maxwell-Bloch equation

$$\frac{\partial^2\vec{E}}{\partial z^2} - \frac{1}{c^2}\frac{\partial^2\vec{E}}{\partial t^2} = \frac{1}{\epsilon_0 c^2}\frac{\partial^2\vec{P}}{\partial t^2}\ . \tag{7.4}$$

Assuming the same phase dependence for the polarization of the medium $\vec{P} =$

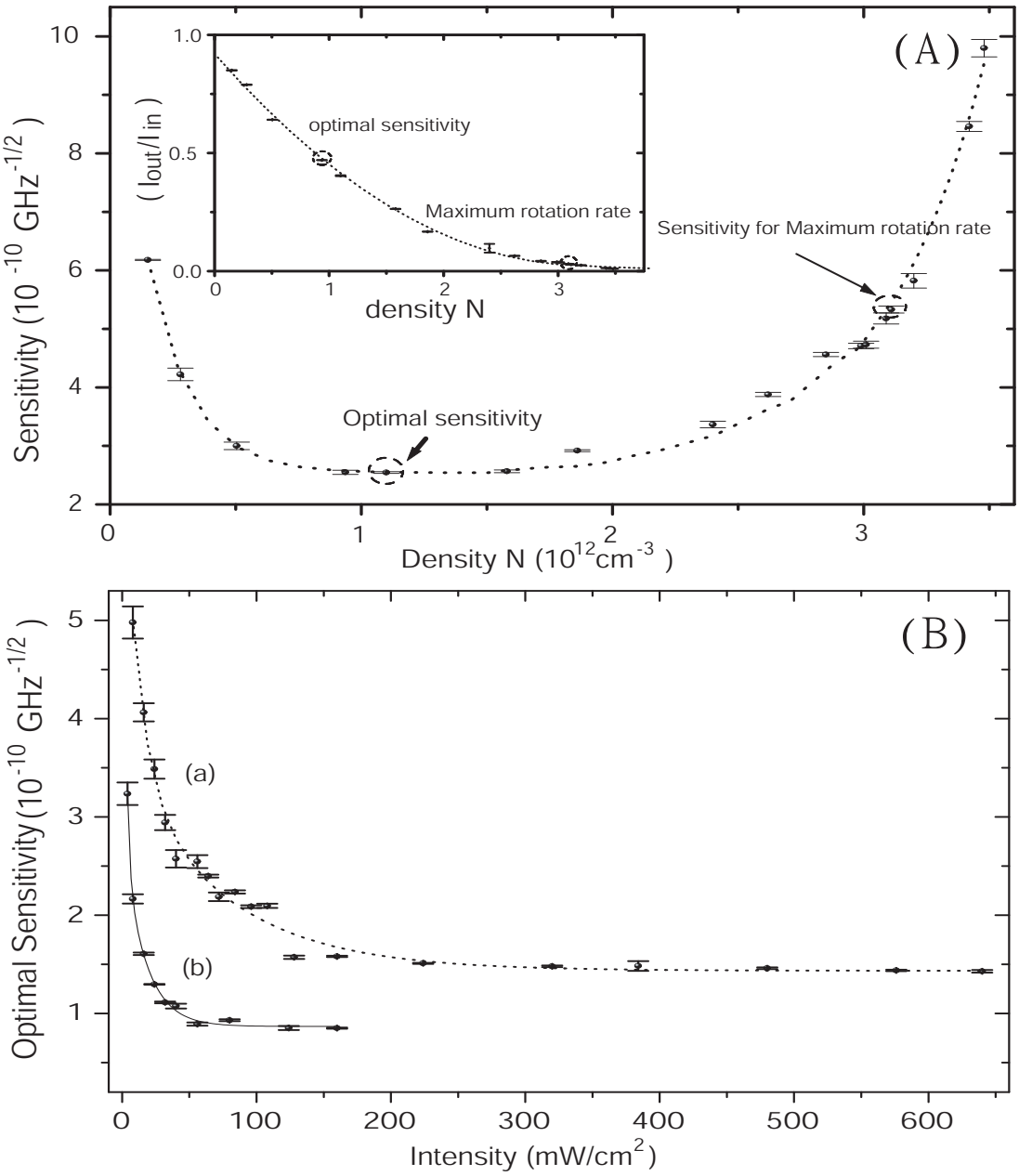

Fig. 31. Sensitivity as function of density for intensity $I = 64$ mW/cm^2 and diameter $d = 2$ mm. The plot shows the optimal sensitivity is not the same as the maximum rotation rate point. The inset shows the transmission(I_{out}/I_{in}) versus density. (B) The optimal sensitivity for each intensity. (a) A Dashed guiding line indicates $d = 2$ mm beam diameter, (b) a solid line indicates $d = 4$ mm beam diameter.

$\hat{e}\mathcal{P}e^{ikz-i\omega t}$ + c.c. as for the field $\hat{E}$ given in Eq. (7.3), and using the slowly varying amplitude and phase approximations, we find

$$\frac{\partial \mathcal{E}}{\partial z} = \frac{ik}{2\epsilon_0}\mathcal{P} \ . \tag{7.5}$$

Considering the atom-field interaction, the Rabi frequencies $\Omega_c = \wp_{ac}\mathcal{E}_c/2\hbar$, $\Omega_b = \wp_{ab}\mathcal{E}_b/2\hbar$ and atomic polarization $\mathcal{P} = N\wp\rho\dot{\text{T}}$he above propagation equations can be written as

$$\frac{\partial \Omega_c}{\partial z} = i\eta_c\rho_{ac} \tag{7.6}$$

$$\frac{\partial \Omega_b}{\partial z} = i\eta_b\rho_{ab} \tag{7.7}$$

where $\eta_b = k_b N\wp_{ab}^2/(\hbar\epsilon_0)$, $\eta_c = k_c N\wp_{ac}^2/(\hbar\epsilon_0)$, and N is the atomic density. The equations for the density matrix elements of the three-level lambda system under consideration are

$$\begin{aligned}\frac{\partial \rho_{aa}}{\partial t} &= -2(\gamma_1+\gamma_2)\rho_{aa} + i\Omega_b\rho_{ba} - i\Omega_b^*\rho_{ab} \\ &\quad + i\Omega_c\rho_{ca} - i\Omega_b^*\rho_{ac} \end{aligned} \tag{7.8}$$

$$\begin{aligned}\frac{\partial \rho_{ab}}{\partial t} &= -(\gamma_1+\gamma_2+i\delta_1)\rho_{ab} - i\Omega_b(\rho_{aa}-\rho_{bb}) \\ &\quad + i\Omega_c\rho_{cb} \end{aligned} \tag{7.9}$$

$$\begin{aligned}\frac{\partial \rho_{ac}}{\partial t} &= -(\gamma_1+\gamma_2+i\delta_2)\rho_{ac} + i\Omega_b\rho_{bc} \\ &\quad - i\Omega_c(\rho_{aa}-\rho_{cc}) \end{aligned} \tag{7.10}$$

$$\frac{\partial \rho_{bb}}{\partial t} = 2\gamma_1\rho_{aa} - i\Omega_c\rho_{ba} + i\Omega_c^*\rho_{ab} \tag{7.11}$$

$$\begin{aligned}\frac{\partial \rho_{bc}}{\partial t} &= -(\gamma_0 + i(\delta_2-\delta_1))\rho_{bc} \\ &\quad + i\Omega_b^*\rho_{ac} - i\Omega_b\rho_{ba} \end{aligned} \tag{7.12}$$

$$\frac{\partial \rho_{cc}}{\partial t} = 2\gamma_2\rho_{aa} - i\Omega_c\rho_{ca} + i\Omega_c^*\rho_{ac}. \tag{7.13}$$

Note that δ_1 and δ_2 are the detunings of the E_b and E_c fields respectively. The conservation of population gives

$$\rho_{aa} + \rho_{bb} + \rho_{cc} = 1. \tag{7.14}$$

We calculate the stationary solutions of the density matrix equations by considering two photon detuning $\delta_1 = -\delta_2 = \delta$ and $\gamma_1 = \gamma_2 = \gamma$, then the full analytical expression for the atomic polarization can be obtained:

$$\begin{aligned}
\rho_{ab} &= i\Omega_b \frac{|\Omega_c|^2\gamma((|\Omega_c|^2 + |\Omega_b|^2)(\gamma_0 - i2\delta) + (2\gamma + i\delta)(\gamma_0^2 + 4\delta^2))}{D1} \\
\rho_{ac} &= i\Omega_c \frac{|\Omega_b|^2\gamma((|\Omega_c|^2 + |\Omega_b|^2)(\gamma_0 + i2\delta) + (2\gamma - i\delta)(\gamma_0^2 + 4\delta^2))}{D2},
\end{aligned} \tag{7.15}$$

where

$$\begin{aligned}
D1 &= \gamma(|\Omega_c|^6 + |\Omega_b|^6) + |\Omega_c|^4(3|\Omega_b|^2(\gamma + \gamma_0) + A) \\
&\quad + |\Omega_b|^4(3|\Omega_c|^2(\gamma + \gamma_0) + A) + |\Omega_b|^2(B + C|\Omega_c|^2) + |\Omega_c|^2 B \\
D2 &= \gamma(|\Omega_c|^6 + |\Omega_b|^6) + |\Omega_c|^4(3|\Omega_b|^2(\gamma + \gamma_0) + A) \\
&\quad + |\Omega_b|^4(3|\Omega_c|^2(\gamma + \gamma_0) + A) + |\Omega_b|^2(B + C|\Omega_c|^2) + |\Omega_c|^2 B \\
A &= 4\gamma(\gamma\gamma_0 - \delta^2) \\
B &= \gamma(4\gamma^2 + \delta^2)(\gamma_0^2 + 4\delta^2) \\
C &= 2\gamma(4\gamma\gamma_0 + 3\gamma_0^2 + 8\delta^2)
\end{aligned} \tag{7.16}$$

To find physical meaning from this, we examine the solution under certain limiting conditions. In the strong field limit where both Ω_b and Ω_c are much larger than γ and δ the atomic polarizations are

$$\rho_{ab} = \frac{\Omega_b|\Omega_c|^2\gamma(2\delta + i\gamma_0)}{\gamma(|\Omega_b|^4 + |\Omega_c|^4) + |\Omega_b|^2|\Omega_c|^2(2\gamma + 3\gamma_0)}$$

$$\rho_{ac} = \frac{\Omega_c|\Omega_b|^2\gamma(-2\delta + i\gamma_0)}{\gamma(|\Omega_b|^4 + |\Omega_c|^4) + |\Omega_b|^2|\Omega_c|^2(2\gamma + 3\gamma_0)} \tag{7.17}$$

In the weak field limit where γ is much greater than Ω_b , Ω_c , and γ_0 the polarizations are

$$\begin{aligned}\rho_{ab} &= \frac{i\Omega_b|\Omega_c|^2\gamma(2\gamma + i\delta)(\gamma_0^2 + 4\delta^2)}{(|\Omega_b|^2 + |\Omega_c|^2)\gamma(4\gamma^2 + \delta^2)(\gamma_0^2 + 4\delta^2)} \\ \rho_{ac} &= \frac{i\Omega_c|\Omega_b|^2\gamma(2\gamma - i\delta)(\gamma_0^2 + 4\delta^2)}{(|\Omega_b|^2 + |\Omega_c|^2)\gamma(4\gamma^2 + \delta^2)(\gamma_0^2 + 4\delta^2)}\end{aligned} \tag{7.18}$$

Thus solutions of Eqs. (7.6) and (7.7) along with Eqs. (7.15) describe the spatial evolution of the fields inside the medium. To study these solutions, we have performed numerical simulations where the rotation rates are determined by taking the difference of nonlinear Faraday spectra with $\mathrm{B}_z = \pm 2$ mG (same as the experimental condition) and $B_z = \pm 10$ μG. The numerical results for the rotation rate are the same for both magnetic field regions except for the low transmission part. By using the smaller B_z the rotation rates always increase with density, and are similar to the analytical results obtained from Ref. [101, 105], that is:

$$\frac{d\phi(L)}{dB}|_{B\to 0} = \frac{2\mu_B}{\hbar\gamma_0}\ln|\frac{I_{in}}{I_{out}}|. \tag{7.19}$$

where I_{in} and I_{out} are the intensities of the laser before and after the atomic cell, μ_B is the Bohr magneton and γ_0 is the decay rate of ground-state Zeeman coherence. However, our experimental measurement shows that the rotation rates drop in the low transmission region (below $\approx 4\%$) which qualitatively agrees with the numerical result using large B_z. Hence, our numerical simulations for the rotation rate are based on large B_z. The discussion of this unexpected dropping effect will be discussed elsewhere.

Our simulations focus on the intensity and density effects on the rotation rates

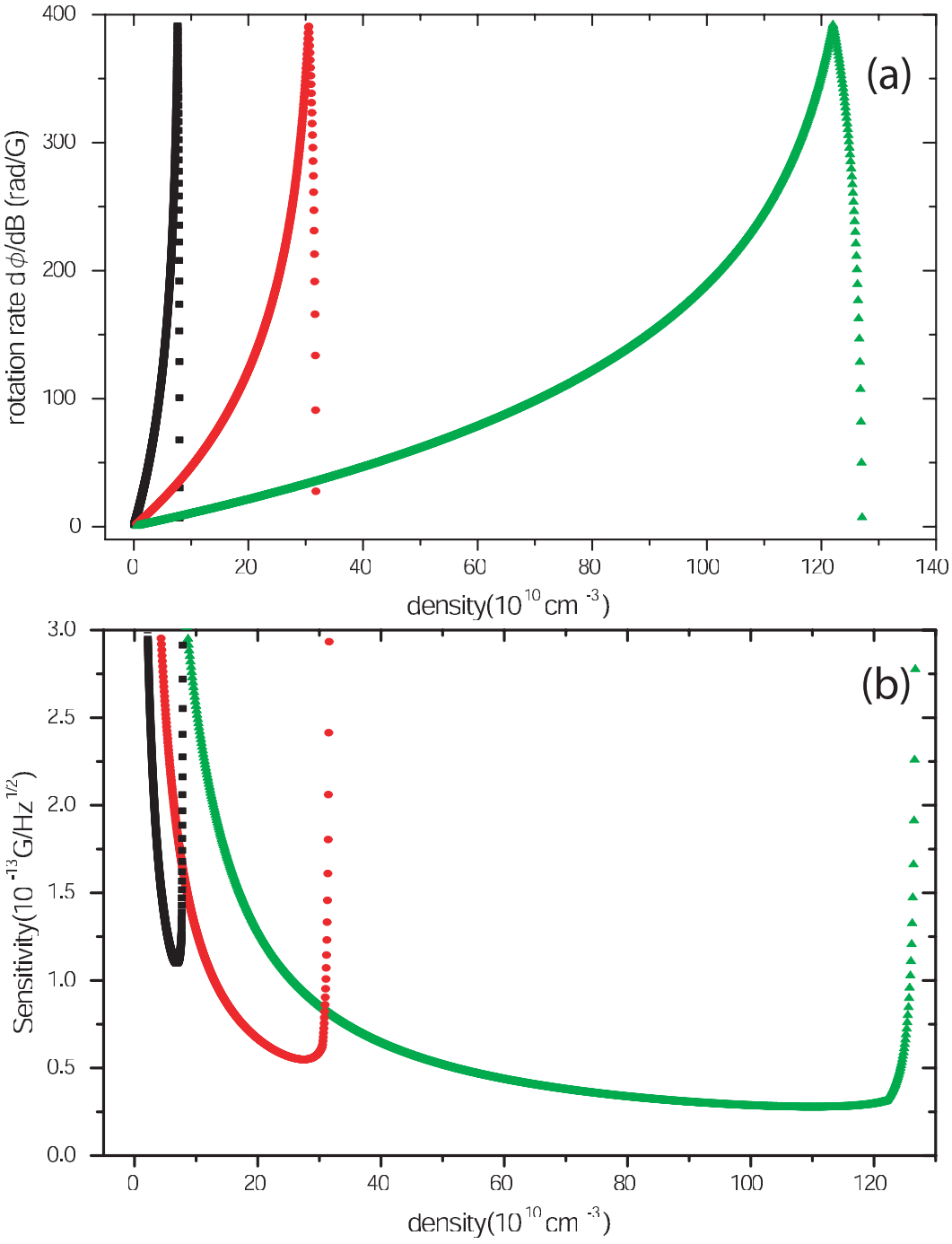

Fig. 32. (a) Plot of rotation slope vs density for different laser Rabi frequency $|\Omega|$. Here $\gamma_0 = 0.001\gamma$, and $\Omega_b = \Omega_c$, $\Omega = \Omega_b + \Omega_c$. Squares: $|\Omega|=2\gamma$, Circles: $|\Omega|=4\gamma$ Triangles: $|\Omega|=8\gamma$. (b) Sensitivity corresponding to the same data as in (a).

and sensitivities. Figure 32(a) shows the rotation rate increases with density but that after passing a certain density it drops rapidly. The maximum rotation is the same for each intensity with the same transmission rate at different densities. The corresponding sensitivity shows that the higher the density and the intensity the better the sensitivity. Our numerical calculations, without considering inhomogeneous Doppler broadening and the incoherent pumping, qualitatively agree with previous experimental results [104, 103]. However, the saturation of the optimal sensitivity at high intensity and the varying maximum rotation rates still cannot be explained from our numerical simulations. We will give a physical interpretation by using our numerical results along with consideration of incoherent pumping effects in the following section.

D. Analysis

As we have seen in the experimental results and numerical simulations, for a constant field intensity higher densities can lead to larger rotation rates (as in Fig. 29), but also leads to increased absorption of the input field. As the atomic density is increased, radiation trapping becomes an important factor [71]. Radiation trapping has a destructive effect on the atomic spin orientation produced by optical pumping, so it can easily spoil the ground-state coherence created by the two coupling lasers polarizations which leads to the absorption increase [109, 110].

The exact solution of the system is extremely complicated and involves 13 magnetic sublevels of the ground and excited hyperfine states for the D_1 line of Rb^{87}. To obtain a qualitative understanding, we consider the simplified three-level system in our previous analysis, and include an incoherent pumping rate for radiation trapping

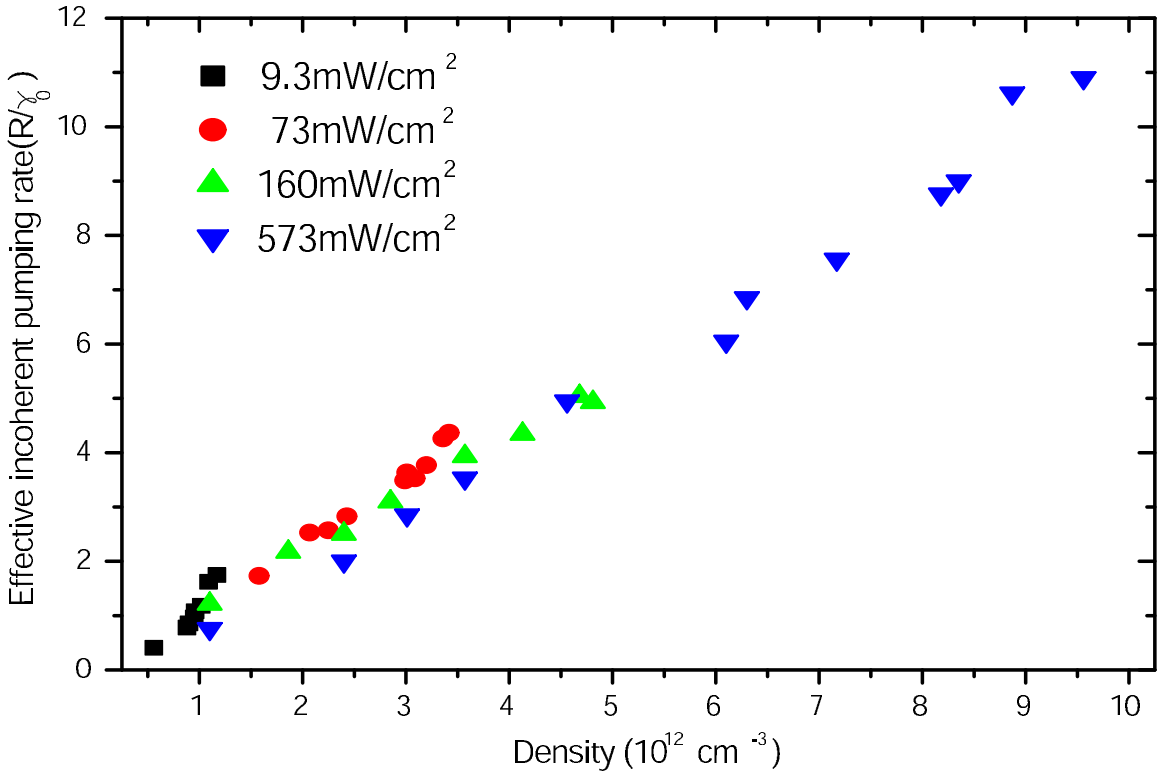

Fig. 33. The scaled incoherent pumping rate R/γ_0 for laser beam diameter $d = 2$ mm

as in Ref. [71]

$$\frac{d\phi(z)}{dB}|_{B\to 0} = \frac{2\mu_B}{\hbar(\gamma_0 + R)} \ln|\frac{I_{in}}{I_{out}}| \tag{7.20}$$

where R is the incoherent pumping rate which can be determined from measuring the rotation rate $d\phi/dB$ and transmission rate I_{out}/I_{in}. The result, based on the data presented earlier, is shown in in Fig. 33. For the case of a beam diameter $d = 2$ mm, the rate of incoherent pumping becomes larger than the ground state dephasing rate $\gamma_0 \sim 20$ KHz at a density of 0.8×10^{12} cm^{-3}. In the transmission region ($I_{out}/I_{in} > 60\%$), the increase rate of rotation rate ($d\phi/dB$) with density is higher than the decrease rate of the square root of the number of transmitted photons $\sqrt{N_{ph}}$, which leads to a greater sensitivity. Once the density is high enough, both rotation rate

and transmission suffer from the increase of decoherence rate owing to the radiation trapping effect, the sensitivity is getting worse with the increasing density, shown in Fig. 31(A).

From the numerical simulation, we conclude that the higher density and intensity can always lead to better sensitivity, shown in Fig. 32(B). However, in the real system, higher the density, higher the incoherent pumping rate R, shown in Fig. 33. The incoherent pumping will not only increase the absorption but also reduce the rotation rate, which suppresses both parameters of the sensitivity. Therefore, the contribution to the increase of sensitivity from the higher intensity and density is evened out by the decoherence from the incoherent pumping. Consequently, the optimal sensitivity curves exhibit the saturated behavior, shown in Fig. 31(B). Larger beam size results in smaller ground state dephasing rate which helps to preserve longer ground state coherence and reduce numbers of spontaneous emitting photons, which can reduce the radiation trapping effect. Therefore, the optimal density for larger beam size is greater than the smaller beam size.

The simulation also shows, under the condition without considering incoherent pumping and Doppler broadening, the maximum rotation rate for each intensity at an optimal density is almost the same, shown in Fig. 32(A). The experimental data do not agree with our simulation and following is our explanation: Higher the density can lead to larger rotation rate, therefore, higher the intensity can help to reach higher density which results in the larger maximum rotation rate. However, the ac-Stark shift and incoherent pumping increases with the intensity and density, respectively. The maximum rotation rate can not always increase with the higher density and intensity, so it saturate at a optimal intensity and density, see Fig. 30(A). The corresponding sensitivity of the maximum rotation rate data also shows a saturation behavior by the intensity, which is similar to the optimal sensitivity curve. The fluctuations of the

data results from the low transmission of the signal into the detector, thus the shot noise level is relative high compared to the sensitivity data at high transmission. In low laser intensity region, the rotation rates and transmission rates increase with the laser intensity which lead to greater sensitivity, then after passing a certain intensity and density, the reduction of the maximum rotation rate and the loss of transmission rate due to incoherent pumping results in the sensitivities of the maximum rotation rate being saturated in the relatively low light intensity region.

E. Summary

We have reported an experimental study of the nonlinear Faraday effect for relatively high input laser intensity and varying density. We have formulated an analytic theory valid both in the linear and nonlinear regimes, and have shown how the previous experimental results are qualitatively matched by our theoretical calculations. We have investigated the saturation of optimal sensitivity. Moreover, behavior of the maximum rotation rate at different intensities has been observed and the corresponding sensitivity curve has been presented. These results can be explained by our numerical calculations associated with incoherent pumping due radiation trapping. To date, the limitation of sensitivity via increasing the laser intensity and density has not been fully explored, so our experimental results can be very useful for choosing the optimal laser intensity and density for and EIT-based magnetometer.

CHAPTER VIII

SUMMARY AND CONCLUSION

The main results of this work are concluded in the following:

1. There is a large control parameter domain for strong resonant $\chi^{(3)}$ processes in a double-ladder system, such as the amplitude and phase of optical drive fields, magnetic fields etc [58]. The derived analytical solutions and theoretical analysis of the double-ladder model provides an excellent understanding of physical properties of the atomic system.

2. It was shown that a new coherent field, with polarization orthogonal to a weak probe field, can be parametrically generated via an all-resonant four-wave-mixing (FWM) process in a double-ladder system [59]. The FWM is resonantly enhanced using EIT in the ladder configuration; therefore, generation of this new field can be realized even in a fairly dilute medium having at least 5% conversion efficiency. We showed experimentally [59] and theoretically [48] that the parametric generation process can be coherently controlled by coupling lasers and magnetic fields. We also showed that the interesting underlying physics is a resonant three-photon process with a wide domain of control parameters.

3. We experimentally observed that in contrast with EIT in a usual ladder system, the addition of a second channel helps to suppress the absorption of two weak probe fields in the double-ladder configuration [111]. We demonstrated that the resulting enhancement of transmission in two different channels is due to new gain caused by the underlying three-photon processes. Our results showed that the transmission of both probe fields is 8% higher than that of the probe in a standard

EIT system. We consider these results to have important applications to new types of polarization switching.

4. We observed ladder-EIT linewidth in a Doppler broadened atomic system that is a factor of 3 smaller than the theoretical prediction.

5. Any coherent control is strongly limited by the coherence lifetime, which is the inverse of the dephasing rate. For improving the ability to control atomic polarization coherently, it is important to know the value of various decoherence rates. A lambda-system, having two ground states coupled to a common excited state by lasers can generate a coherent eigen (dark)-state that is transparent to the incoming fields and, hence, suppresses fluorescence from the excited state. However, ground-state dephasing perturbs the dark state, leading to an increase in fluorescence. From our analytical calculations, we suggested the use of this strong dependence of fluorescence on the ground-state dephasing as a new method for measuring ground-state dephasing rates. The theory and a proof-of-principle experiment using ^{87}Rb vapor are presented in Ref [69].

6. When the two laser fields in a lambda-system are resonant with their respective transitions, the atomic polarization is very sensitive to the applied magnetic field that can be used for optical magnetometry. To date, the sensitivity of the best optical magnetometer based on atomic systems can reach $\approx$3x10^{12} G/$\sqrt{Hz}$ at room temperature, which is superior to the sensitivity of present state-of-the-art devices. The degree of sensitivity of such optical magnetometers is determined by two competing parameters–atomic density and laser intensity. Early theoretical predictions showed that the sensitivity could be improved by increasing the laser intensity and

atomic density. However, we showed experimentally [112] that the optimal sensitivity reaches saturation, and does not increase indefinitely with an increase in the above parameters. We have shown that the underlying physics is the re-absorption and re-emission of the spontaneously emitted photons in the optically thick medium, which increase the ground-state dephasing rate, leading to reduction of the benefit of increasing the above two parameters. Our work helps to optimize the laser intensity and atomic density and obtain optimal sensitivity of the optical magnetometer.

REFERENCES

[1] I. Newton,"*Opticks: Or a Treatise of the Reflections, Refractions, Inflections and Colours of Light-Based*," 4th Ed., London (1730).

[2] C. Huygens,"*Treatise on Light*," London (1690).

[3] M. Plank,"Zur Theorie des Gesetzes der Energieverteilung im Normalspektrum," Verh. dt. phys. Ges. **2**, 202 (1900).

[4] A. Einstein,"Zur Quantentheorie der Strahlung," Phys. Z**18**, 121 (1917).

[5] A. L. Schawlow and C. H. Townes,"Infrared and Optical Masers," Phys. Rev. **112**, 1940 (1958).

[6] E. Arimondo,"Coherent population trapping in laser spectroscopy," Prog. Optics **35**, 259 (1996).

[7] M. Fleischhauer, A. Imamoglu and J. P. Marangos,"Electromagnetically induced transparency: Optics in coherent media," Rev. Mod. Phys. **77**, 633 (2005).

[8] A. Javan,"Theory of a Three-Level Maser," Phys. Rev. **107**, 1579 (1956).

[9] O. Kocharovskaya and Ya I. Khanin,"Coherent amplification of an ultrashort pulse in a three-level medium without a population inversion," JETP Lett. **48**, 630 (1988).

[10] M. O. Scully, S.-Y. Zhu, and A. Gavrielides,"Degenerate quantum-beat laser: Lasing without inversion and inversion without lasing," Phys. Rev. Lett. **62**, 2813 (1989).

[11] Chu S, Hollberg L, Bjorkholm JE, Cable A, Ashkin A. "Three-dimensional viscous confinement and cooling of atoms by resonance radiation pressure," Phys. Rev. Lett. **55**, 48 (1985).

[12] M. H. Anderson, J. R. Ensher, M. R. Matthews, C. E. Wieman, and E. A. Cornell,"Observation of Bose-Einstein Condensation in a Dilute Atomic Vapor ," Science **269**, 198 (1995).

[13] M. M. Kash, V. A. Sautenkov, A. S. Zibrov, L. Hollberg, G. R. Welch, M. D. Lukin, Y. Rostovtsev, E. S. Fry, and M. O. Scully,"Ultraslow Group Velocity and Enhanced Nonlinear Optical Effects in a Coherently Driven Hot Atomic Gas," Phys. Rev. Lett. **82**, 5229 (1999).

[14] D. Budker, D. F. Kimball, S. M. Rochester, V. V. Yashchuk, and M. Zolotorev,"Ultraslow Group Velocity and Enhanced Nonlinear Optical Effects in a Coherently Driven Hot Atomic Gas," Phys. Rev. Lett. **83**, 1767 (1999).

[15] A. V. Turukhin, V. S. Sudarshanam, M. S. Shahriar, J. A. Musser, B. S. Ham, and P. R. Hemmer,"Observation of Ultraslow and Stored Light Pulses in a Solid," Phys. Rev. Lett. **88**, 023602 (2002).

[16] N. Herbert,"FLASH-a superluminal communicator based. upon a new kind of quantum measurement," Found. Phys. **12**, 1171 (1982).

[17] M. Fleischhauer and M. D. Lukin,"Dark-State Polaritons in Electromagnetically Induced Transparency," Phys. Rev. Lett. **84**, 5094 (2000).

[18] D. F. Phillips, A. Fleischhauer, A. Mair, R. L. Walsworth, and M. D. Lukin,"Storage of Light in Atomic Vapor," Phys. Rev. Lett. **86**, 783 (2001).

[19] J. D. jackson,"*Cassical Electrodynamics*," 3rd Ed., Wiley, New York (1962).

[20] M. O. Scully and M. S. Zubairy,"*Quantum Optics*," Cambridge University Press (1997).

[21] R. Shanker,"*Principle of Quantum Mechanics*," New York and London Press (1994).

[22] F. Schuller,"*The Liouville Space Formation in Atomic Spectroscopy*," Heron Press (2002).

[23] S. E. Harris, J. E. Field, and A. Imamoglu,"Nonlinear optical processes using electromagnetically induced transparency," Phys. Rev. Lett. **64**, 1107 (1990).

[24] S. P. Tewari and G. S. Agarwal,"Control of Phase Matching and Nonlinear Generation in Dense Media by Resonant Fields," Phys. Rev. Lett. **56**, 1811 (1986).

[25] S. E. Harris and Y. Yamamoto,"Photon Switching by Quantum Interference," Phys. Rev. Lett. **81**, 3611 (1998).

[26] H. Schmidt and A. Imamoglu,"High-speed properties of a phase-modulation scheme based on electromagnetically induced transparency," Opt. Lett. **23**, 1007 (1998).

[27] R. W. Boyd,"*Nonlinear Optics*," 2nd Ed., Elsevier, Singapore (2003).

[28] S. E. Harris,"Electromagnetically induced transparency," Phys. Today **50**, 36 (1997).

[29] S. E. Harris and L. V. Hau,"Nonlinear Optics at Low Light Levels," Phys. Rev. Lett **82**, 4611 (1999).

[30] A. Imamoglu, H. Schmidt, G. Woods, and M. Deutsch,"Strongly Interacting Photons in a Nonlinear Cavity," Phys. Rev. Lett. **79**, 1467 (1997).

[31] H. Schmidt and A. Imamoglu,"Giant Kerr nonlinearities obtained by electromagnetically induced transparency," Opt. Lett. **21**, 1936 (1996).

[32] H. Kang and Y. Zhu,"Observation of Large Kerr Nonlinearity at Low Light Intensities," Phys. Rev. Lett. **91**, 093601-1 (2003).

[33] Y. Li and M. Xiao,"Enhancement of nondegenerate four-wave mixing based on electromagnetically induced transparency in rubidium atoms," Opt. Lett. **21**, 1064 (1996).

[34] M. D. Lukin, M. Fleischhauer, A. S. Zibrov, H. G. Robinson, V. L. Velichansky, L. Hollberg and M. O. Scully,"Spectroscopy in Dense Coherent Media: Line Narrowing and Interference Effects," Phys. Rev. Lett. **79**, 2959 (1997).

[35] E. E. Mikhailov, V. A. Sautenkov, Y. V. Rostovtsev, A. Zhang, M. S. Zubairy, M. O. Scully and G. R. Welch,"Spectral narrowing via quantum coherence," Phys. Rev. A **74**, 013807 (2006).

[36] K. Hakuta, L. Marmet and B. P. Stoicheff,"Electric-field-induced second-harmonic generation with reduced absorption in atomic hydrogen," Phys. Rev. Lett. **66**, 596 (1991).

[37] G. Z. Zhang, K. Hakuta and B. P. Stoicheff,"Nonlinear optical generation using electromagnetically induced transparency in atomic hydrogen," Phys. Rev. Lett. **71**, 3099 (1993).

[38] J. Gea-banacloche, Y. Li, S. Jin, and M. Xiao, "Electromagnetically induced transparency in ladder-type inhomogeneously broadened media: Theory and experiment," Phys. Rev. A **51**, 576 (1995).

[39] S. Wielandy and A. L. Gaeta,"Coherent Control of the Polarization of an Optical Field," Phys. Rev. Lett. **81**, 3359 (1998).

[40] A. K. Patnaik and G. S. Agarwal,"Laser field induced birefringence and enhancement of magneto-optical rotation," Opt. Commn. **179**, 97 (2000).

[41] A. K. Patnaik and G. S. Agarwal,"Coherent control of magneto-optical rotation in inhomogeneously broadened medium," Opt. Commn. **199**, 127 (2001).

[42] T. H. Yoon, C. Y. Park and S. J. Park,"Laser-induced birefringence in a wavelength-mismatched cascade system of inhomogeneously broadened Yb atoms," Phys. Rev. A **70**, 061803(R) (2004).

[43] V. Boyer, C. F. McCormick, E. Arimondo, and P. D. Lett,"Ultraslow Propagation of Matched Pulses by Four-Wave Mixing in an Atomic Vapor," Phys. Rev. Lett. **99**, 143601 (2007).

[44] Y. R. Shen,"*Principles of Nonlinear Optics*," Wiley, New York (1984).

[45] S. Roy, W. D. Kulatilaka, S. V. Naik, N. M. Laurendeau, R. P. Lucht and J. R. Gord,"Effects of quenching on electronic-resonance-enhanced coherent anti-Stokes Raman scattering of nitric oxide," Appl. Phys. Letts. **89**, 104105 (2006).

[46] S. F. Hanna, W. D. Kulatilaka, Z. Arp, T. Opatrny, M. O. Scully, J. P. Kuehner and R. P. Lucht,"Electronic-resonance-enhanced coherent anti-Stokes Raman spectroscopy of nitric oxide," Appl. Phys. Letts. **83**, 1887 (2003).

[47] Y. Zhang, A. W. Brown and M. Xiao,"Observation of interference between four-wave mixing and six-wave mixing," Opt. Lett. **32**, 1120 (2007).

[48] P. S. Hsu, A. K. Patnaik and G. R. Welch, "Magneto-optical control of resonant $\chi^{(3)}$ process in double ladder system," (in preparation).

[49] D. A. Steck, "*Cs D line data report*," revision 1.6 (2003).

[50] G. R. Welch, G. G. Padmabandu, E. S. Fry, M. D. Lukin, D. E. Nikonov, F. Sander, M. O. Scully, A. Weis and F. K. Tittel, "Observation of V-type electromagnetically induced transparency in a sodium atomic beam," Fundations of physics, vol. **28**, 621 (1998).

[51] D. Petrosyan and Y. P. Malakyan,"Magneto-optical rotation and cross-phase modulation via coherently driven four-level atoms in a tripod configuration," Phys. Rev. A **70**, 023822 (2004).

[52] S. Rebic, D. Vitali, P. Tombesi, M. Artoni, F. Cataliotti and R. Corbalan,"Polarization phase gate with a tripod atomic system ," Phys. Rev. A **70**, 032317 (2004).

[53] A. Eilam, A. D. Wilson-Gordon and H. Friedmann,"Enhanced frequency conversion of nonadiabatic pulses in a double lambda system driven by two pumps with and without carrier beams," Opt. Commn. **277**, 186 (2007).

[54] C. Ottaviani, D. Vitali, M. Artoni, F. Cataliotti and P. Tombesi, "Polarization Qubit Phase Gate in Driven Atomic Media," Phys. Rev. Lett. **90**, 197902-1 (2003).

[55] Z. Wang, K. Marzlin and B. C. Sanders,"Large Cross-Phase Modulation between Slow Copropagating Weak Pulses in ^{87}Rb," Phys. Rev. Lett. **97**, 063901-1 (2006).

[56] S. H. Autler and C. H. Townes,"Stark Effect in Rapidly Varying Fields," Phys. Rev. **100**, 703 (1955).

[57] S. J. Park, C. Y. Park and T. H. Yoon,"Optical polarization modulation by competing atomic coherence effects in a degenerate four-level Yb atomic system,"

Phys. Rev. A **71**, 063819 (2005).

[58] P. S. Hsu, A. K. Patnaik and G. R. Welch,"Study of resonant $\chi^{(3)}$ process in double ladder system" (in preparation).

[59] P. S. Hsu, A. K. Patniak and G. R. Welch,"Controlled parametric generation in a double-ladder system via all-resonant four-wave mixing," Opt. Lett. **33**, 381-383 (2008).

[60] B. ü, W. H. Burkett, and M. Xiao,"Nondegenerate four-wave mixing in a double-Lambda system under the influence of coherent population trapping," Opt. Lett. **23**, 804 (1998).

[61] K. Hakuta, M. Suzuki, M. Katsuragawa, and J. Z. Li,"Self-Induced Phase Matching in Parametric Anti-Stokes Stimulated Raman Scattering," Phys. Rev. Lett. **79**, 209 (1997).

[62] S. E. Harris and A. Sokolov,"Subfemtosecond Pulse Generation by Molecular Modulation," Phys. Rev. Lett. **81**, 2894 (1998).

[63] A. S. Zibrov, M. D. Lukin, and M. O. Scully,"Experimental Demonstration of Laser Oscillation without Population Inversion via Quantum Interference in Rb," Phys. Rev. Lett. **75**, 1499 (1995).

[64] J. Kitching and L. Hollberg,"Interference-induced optical gain without population inversion in cold, trapped atoms," Phys. Rev. A **59**, 4685 (1999).

[65] J. Kitching *et al.*, "A microwave frequency reference based on VCSEL-driven dark line resonance in Cs vapor," IEEE Trans. Instrum. **49**, 1313 (2000).

[66] M. Fleishhauer and M. D. Lukin,"Dark-State Polaritons in Electromagnetically Induced Transparency," Phys. Rev. Lett. **84**, 5094 (2000).

[67] C. Liu, Z. Dutton, C. Behroozi and L.V. Hau,"Observation of coherent optical information storage in an atomic medium using halted light pulses," Nature (London) **409**, 490 (2000).

[68] C. Y. Ye and A. S. Zibrov,"Width of the electromagnetically induced transparency resonance in atomic vapor," Phys. Rev. A **65**, 023806 (2002).

[69] A. K. Patnaik, P. S. Hsu, G. S. Agarwal, G. R. Welch and M. O. Scully,"Measurement of ground-state decoherence via interruption of coherent population trapping," Phys. Rev. A **75**, 023807 (2007).

[70] A. V. Taichenachev, A. M. Tumaikin, V. I. Yudin,"Electromagnetically induced absorption in a four-state system," Phys. Rev. A **61**, 011802 (1999).

[71] A. B. Matsko, I. Novikova, G. R. Welch,"Compensation of ac Stark shifts in optical magnetometry," Phys. Rev. Lett. **87**, 133601 (2001).

[72] S. Knappe, R. Wynands, J. Kitching, H. G. Robinsion, and L. Hollberg,"Characterization of coherent population-trapping resonances as atomic frequency references," J. Opt. Soc. Am. B **18**, 1545 (2001).

[73] J. Vanier, A. Gordone, and F. Levi,"Coherent population trapping in cesium: Dark lines and coherent microwave emission," Phys. Rev. A **58**, 2345 (1998).

[74] V. A. Sautenkov, M. M. kash, V. L. Velichansky, and G. R. Welch,"Density narrowing in electromagnetically induced transparency," Laser Phys. **9**, 1 (1999).

[75] A. Akulshin, S. Barriero, and A. Lezama,"Electromagnetically induced absorption and transparency due to resonant two-field excitation of quasidegenerate levels in Rb vapor," Phys. Rev. A **57**, 2996 (1998).

[76] W. Demtröder,"*Laser Spectroscopy*," Springer-Verlag, New York (2002).

[77] Y. R. Shen, "*Principles of Non-linear Optics*," Wiley, New York (1984).

[78] F. DeMartini and J. Ducuing,"Stimulated Raman Scattering in Hydrogen: A Measurement of the Vibrational Lifetime," Phys. Rev. Lett. **17**, 117 (1966).

[79] A. Laubereau and W. Kaiser,"Vibrational dynamics of liquids and solids investigated by picosecond light pulses," Rev. Mod. Phys. **50**, 607 (1978).

[80] G. S. Agarwal and S. S. Jha,"Theory of Resonant Raman Scattering in Intense Double Frequency Fields," J. Phys. B **12**, 2655 (1979).

[81] D. G. Steel and J. F. Lam,"Two-Photon Coherent-Transient Measurement of the Nonradiative Collisionless Dephasing Rate in SF6 via Doppler-Free Degenerate Four-Wave Mixing," Phys. Rev. Lett. **43**, 1588 (1979).

[82] I. V. Jyotsna and G. S. Agarwal,"Coherent population trapping at low light levels," Phys. Rev. A **52**, 3147 (1995).

[83] R. Loudon, "*Quantum Theory of Light*," Oxford University Press (2001).

[84] J. Z. Li, M. Katsuragawa, M. Suzuki, and K. Hakuta,"Stimulated Raman scattering in solid hydrogen: Measurement of coherence decay," Phys. Rev. A **58**, R58 (1998).

[85] E. E. Mikhailov, I. Novikova, Y. V. Rostovtsev, and G. R. Welch,"Bffer-gas-induced absorption resonances in Rb vapor," Phys. Rev. A **70**, 033806 (2004).

[86] B. Lounis and W. E. Moerner,"Single Photons on Demand from a Single Molecule at Room Temperature," Nature **407**, 491 (2000).

[87] C. Kurtsiefer, S. Mayer, P. Zarda, and H. Weinfurter,"Stable Solid-State Source of Single Photons" Phys. Rev. Lett. **85**, 290 (2000).

[88] R. Brouri, A. Beveratos, J.-P. Poizat, and P. Grangier,"Photon antibunching in the fluorescence of individual color centers in diamond," Opt. Lett. **25**, 1294 (2000).

[89] A. K. Patnaik, J. Q. Liang, and K. Hakuta,"Slow light propagation in a thin optical fiber via electromagnetically induced transparency," Phys. Rev. A **66**, 063808 (2002).

[90] E. A. Muljarov, T. Takagahara, and R. Zimmermann,"Phonon-Induced Exciton Dephasing in Quantum Dot Molecules," Phys. Rev. Lett. **95**, 177405 (2005).

[91] P. Borri, L. Lagbein, U. Woggon, M. Schwab, M. Beyer, S. Fafard, Z. Wasilewski, and P. Hawrylak,"Exciton Dephasing in Quantum Dot Molecules," Phys. Rev. Lett. **91**, 267401 (2003).

[92] F. Renzoni, W. Maichen, L. Windholz, and E. Arimondo,"Coherent population trapping with losses observed on the Hanle effect of the D_1 sodium line," Phys. Rev. A **55**, 3710 (1997).

[93] J. Vanier and C. Audoin," *The quantum physics of atomic frequency standards*," Bristol ; Philadelphia : A. Hilger (1989).

[94] W. Happer,"Optical Pumping," Rev. Mod. Phys. **44**, 169 (1972).

[95] J. Geremia, J. K. Stockton, and H. Mabuchi,"Suppression of Spin Projection Noise in Broadband Atomic Magnetometry," Phys. Rev. Lett. **94**, 203002 (2005).

[96] V. Petersen, L. B. Madsen, and K. Moler,"Magnetometry with entangled atomic samples," Phys. Rev. A **71**, 012312 (2005).

[97] E. Taskova, S. Gateva, E. Alipeva, K. Kowalski, M. Glodz and J. Szonert,"Nonlinear Faraday Rotation for Optical Limitation," App. Opt. **43**, 4178 (2004).

[98] E. B. Alexandrov, M. V. Balabas, A. S. Pasgalev, A. K. Vershovskii, and N. N. Yakobson,"Double-Resonance Atomic Magnetometers: from Gas Discharge to Laser Pumping," Laser Phys. **6**, 244 (1996).

[99] E. B. Alexandrov and V. A. Bonch-Bruevich, "Optically pumped atomic magnetometers after three decades," Opt. Eng. (Bellingham) **31**, 711 (1992).

[100] M. O. Scully,"Enhancement of the index of refraction via quantum coherence," Phys. Rev. Lett. **67**, 1855 (1991).

[101] M. Fleischhauer, A. B. Matsko, and M. O. Scully,"Quantum limit of optical magnetometry in the presence of ac Stark shifts," Phys. Rev. A **62**, 013808 (2000).

[102] M. D. Lukin, L. W. Hollberg, D. E. Nikonov, M. O. Scully, H. G. Robinson, and V. L. Velichansky,"Experimental Demonstration of Enhanced Index of Refraction via Quantum Coherence in Rb," Phys. Rev. Lett. **76**, 3935 (1996).

[103] I. Novikova and G. R. Welch,"Magnetometry in dense coherent media," J. Mod. Opt. **49**, 349 (2002).

[104] D. Budker, D. F. Kimball, S. M. Rochester, V. V. Yashchuk, and M. Zolotorev,"Sensitive magnetometry based on nonlinear magneto-optical rotation," Phys. Rev. A **62**, 043403 (2000).

[105] V. A. Sautenkov, M. D. Lukin, C. J. Benar, I. Novikova, E. Milhailov, M. Fleischhauer, V. L. Velichansky, G. R. Welch, and M. O. Scully,"Enhancement

of magneto-optic effects via large atomic coherence in optically dense media," Phys. Rev. A **62**, 023810 (2000).

[106] I. K. Kominis, T. W. Kornack, J. C. Allred and M. V. Romalis,"Sub-femtotesla Multi-channel Atomic Magnetometer," Nature **422**, 596 (2003).

[107] W.Gawlik, L. Krzemien, S. Pustelny, D. Sang, J. Zachorowski, M. Graf, A. O. Sushkov and D. Budker,"Nonlinear magneto-optical rotation with amplitude modulated light," Appl. Phys. Lett. **88**, 131108 (2006).

[108] I. Novikova, A. B. Matsko, V. L. Velichansky, M. O. Scully, and G. R. Welch,"Compensation of ac Stark shifts in optical magnetometry," Phys. Rev. A **63**, 063802 (2001).

[109] A. B. Matsko, I. Novikova, G. R. Welch,"Radiation trapping under conditions of Electromagnetically Induced Transparency," J. Mod. Opt. **49**, 367 (2002).

[110] G. Ankerhold, M. Schiffer, D. Mutschall, T. Scholz, and W. Lange,"Nonlinear effects of radiation trapping in ground-state oriented sodium vapor," Phys. Rev. A **48**, R4031 (1993).

[111] Paul S. Hsu, Anil K. Patnaik, and George R. Welch," Transmission Enhancement of double-EIT in double ladder system,"(To be submitted to Physical Review A).

[112] Paul S. Hsu, Anil K. Patnaik, and George R. Welch, "Optical Magnetometry with Intense Laser Field," (To be submitted to Physical Review A).

[113] R. N. Hall, G. E. Fenner, J. D. Kingsley, T. J. Soltys, and R. O. Carlson,"Coherent Light Emission From GaAs Junctions," Phys. Rev. Lett. **9**, 366 (1962).

[114] M. W. Fleming, and A. Mooradian,"Fundamental line broadening of single-mode (GaAl)As diode lasers," Appl. Phys. Lett. **38**, 511 (1981).

[115] Y. S. Cheng and R. C. Chang,"Characteristics of a prism-pair anamorphic optical system for multiplex holography," Opt. Eng. **37**, 2717 (1998).

[116] L. G. Deshazer and E. A. Maunders,"Optical isolator for near infrared," Rev. Sci. Instrum. **38**, 248 (1967).

[117] D. J. Gauthier, P. Narm, and R. W. Boyd,"Simple, compact, high-performance permanent-magnet Faraday isolator," Opt. Lett. **11**, 623 (1986).

APPENDIX A

DIODE LASER

Forty years ago, Robert N. Hall and his team at General Electric research center invented the first diode laser [113]. Since then this small and compact coherent light source has been widely used both in industry and science. Comprehensive reviews of basic properties and the spectroscopic applications of diode lasers have been discussed in Ref [113]; for that reason we provide the specific information concerning the diode laser system used in the experiments.

We use a single mode laser diode operating at the wavelength 852 nm. The laser diode has an anti-reflection (AR) coating on the front facet of the diode with reflection below 0.05%. The diode is thermostabilized to ensure reliable operation and to reduce the drift of the laser frequency due to the temperature fluctuations. Since the laser linewidth for the free-running diode laser is quite broad, ~ 25 MHz, it can be improved by using a frequency selective optical feedback system [114]. In our experiment, we use an external cavity in Littrow configuration, shown in Fig. 34, to reduce the linewidth and improve the wavelength selectivity. The AR coating of the laser diode can increase the effect of the external feedback. The emission from the laser is collimated and coupled to a diffraction grating. The first order diffraction is coupled into laser diode as optical feedback. Wavelength tuning can be performed by rotation of the grating. Although we have not performed a precision laser linewidth measurement for our system, its value from the Doppler-free spectroscopy measurement can be estimated at about 1 MHz, which is below the radiative width of the Cs transitions ($\gamma = 2\pi \cdot 5.3$ MHz). The spacial beam profile of the diode laser system is ellipse due to the geometry of the diode chip. To obtain a Gaussian beam profile,

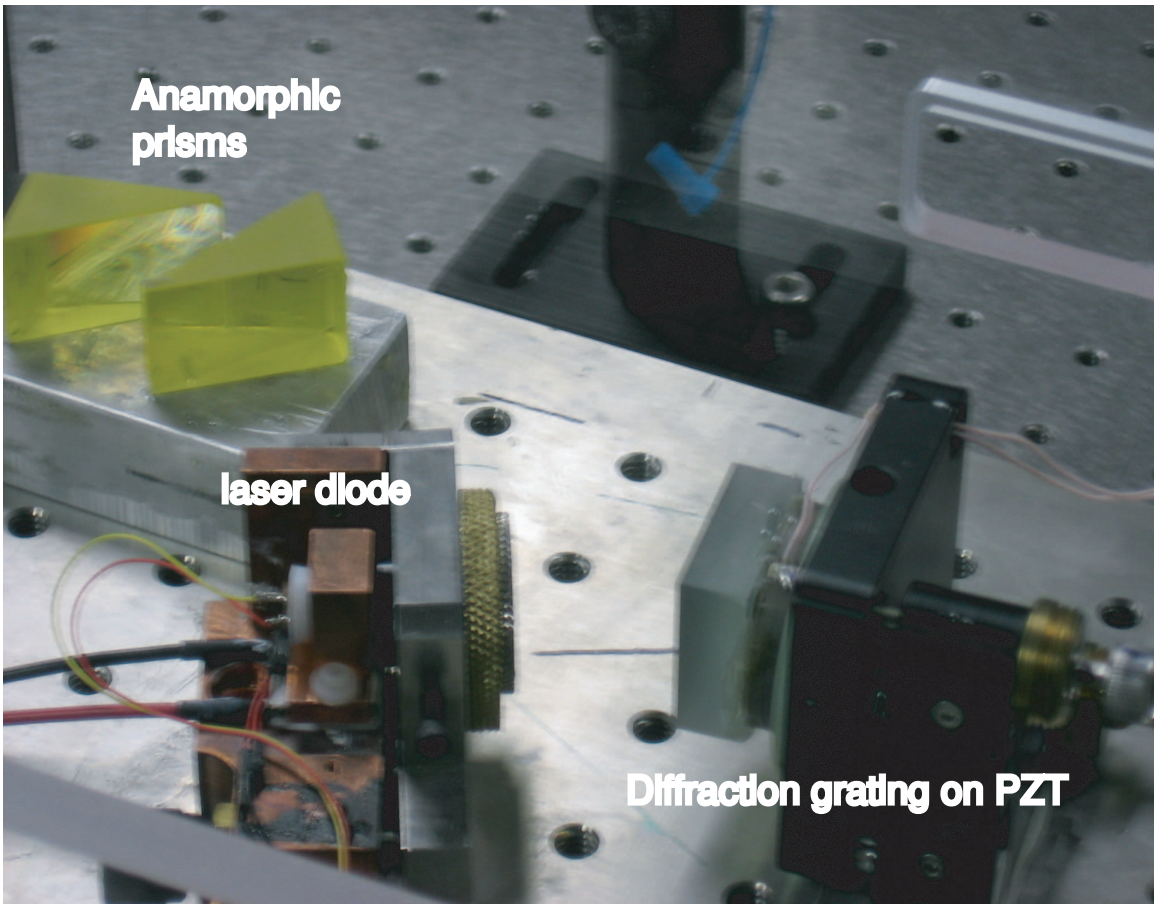

Fig. 34. The photo of the external cavity diode laser used in the experiment.

the symmetry of the laser beam may be adjusted by a pair of anamorphic prisms [115]. To avoid retro-reflections from various surfaces, a Faraday isolator [116, 117] is placed after the laser. The maximum laser power available from external cavity diode laser system is $P_{mzx} \simeq 10\ mW$ with the beam size D=2 mm.

APPENDIX B

DOUBLE-EIT AND EIT COMPARISON IN THE DIFFERENT ATOMIC SYSTEM

A. Double-lambda system

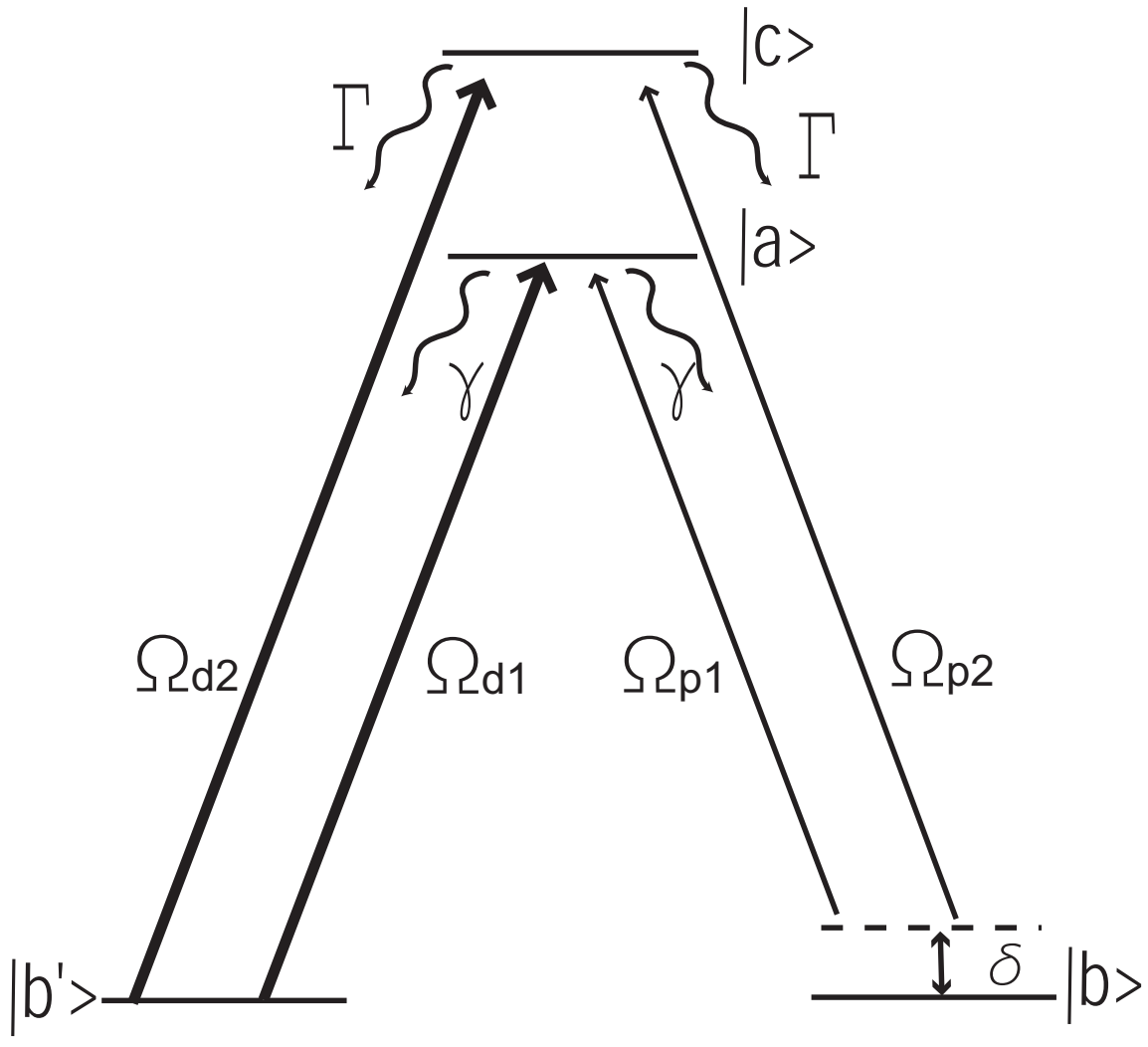

Fig. 35. Diagram showing the energy level of double-lambda system

We consider a four-level double-lambda system, shown in Fig. 35. The probe(drive) transition is $|b\rangle \rightarrow |i\rangle (|b'\rangle \rightarrow |i\rangle)$, i=a,c. The interaction Hamiltonian in rotation wave approximation (RAW) can be written as [20]

$$\begin{aligned}\mathcal{H}_I &= -\hbar[\Omega_{p2}|c\rangle\langle b|e^{-iw_{p1}t} + \Omega_{p2}|a\rangle\langle b|e^{-iw_{p2}t} + \Omega_{d1}|a\rangle\langle b'|e^{-iw_{d1}t} + \\ &\quad \Omega_{d2}|c\rangle\langle b'|e^{-iw_{d2}t} + h.c.]. \end{aligned} \tag{B.1}$$

Using standard semiclassical methods (see, e.g. [20]), we find the following equations of motion for the matrix elements of the atomic density operator:

$$\begin{aligned}\frac{\partial \rho_{ab}}{\partial t} &= -i\Omega_{p1} - (\gamma + i\delta)\rho_{ab} - i\Omega_{d1}\rho_{b'b} + i\Omega_{p2}\rho_{ac} \\ \frac{\partial \rho_{cb}}{\partial t} &= -i\Omega_{p2} - (\Gamma + i\delta)\rho_{cb} - i\Omega_{d2}\rho_{b'b} + i\Omega_{p1}\rho_{ca} \\ \frac{\partial \rho_{b'b}}{\partial t} &= -(\gamma_{b'b} + i\delta)\rho_{b'b} + i\Omega_{p1}\rho_{b'a} - i\Omega^*_{d1}\rho_{ab} + i\Omega_{p2}\rho_{b'c} - i\Omega^*_{d2}\rho_{cb} \end{aligned} \tag{B.2}$$

As we show below, as long as we are only interested in the solution of system to lowest order in the weak probe field. The off-diagonal elements for probe transition can be solved from Eqns. (B.2) as

$$\begin{aligned}\rho_{ab} &= \frac{i\Omega_{p1}}{i\delta + \gamma}[\frac{(i\delta + \gamma_{b'b})(i\delta + \gamma)(i\delta + \Gamma) + (i\delta + \gamma)|\Omega_{d2}|^2}{D}] \\ &\quad -\frac{i\Omega_{p2}\Omega_{d1}\Omega^*_{d2}}{D} \end{aligned} \tag{B.3}$$

$$\begin{aligned}\rho_{cb} &= \frac{i\Omega_{p2}}{i\delta + \gamma}[\frac{(i\delta + \gamma_{b'b})(i\delta + \gamma)(i\delta + \Gamma) + (i\delta + \Gamma)|\Omega_{d1}|^2}{D}] \\ &\quad -\frac{i\Omega_{p2}\Omega^*_{d1}\Omega_{d2}}{D} \end{aligned} \tag{B.4}$$

where

$$D = (i\delta + \gamma_{b'b})(i\delta + \gamma)(i\delta + \Gamma) + (i\delta + \Gamma)|\Omega_{d1}|^2 + (i\delta + \gamma)|\Omega_{d2}|^2 \tag{B.5}$$

Assuming $\Omega_{p1} = \Omega_{p2} = \Omega_p$, $\Omega_{d1} = \Omega_{d2} = \Omega_d$ and $\gamma = \Gamma$ for double-EIT case, under such condition, $\rho_{ab} = \rho_{a'b}$. Then we compare EIT and double-EIT in lambda system in the resonant condition

$$\begin{aligned} \rho_{ab}^{double-EIT} &= \frac{i\Omega_p\gamma_{b'b}\gamma}{\gamma_{b'b}\gamma^2 + 2\gamma|\Omega_d|^2} \\ \rho_{ab}^{EIT} &= \frac{i\Omega_p\gamma_{b'b}\gamma}{\gamma_{b'b}\gamma^2 + \gamma|\Omega_d|^2} \end{aligned} \tag{B.6}$$

The results show that the coherence term ρ_{ab} of double-EIT in the double-lambda configuration have larger denominator compared to the EIT in lambda configuration. Therefore, the better transparency for double-EIT in double-lambda system can be expected. Physically, we can also see this kind of double-lambda scheme, shown in Fig. 35, as folded double-ladder scheme. Therefore, we prove the similar behavior of two-channel transmission enhancement can also exist in the double-lambda system.

B. Tripod system

We consider a four-level tripod system, shown in Fig. 36. The probe (drive) laser couple the transition $|i\rangle \rightarrow |a\rangle$ ($|c\rangle \rightarrow |a\rangle$); $i = b, b'$. The Rabi frequency of the correspond probe (drive) transition is $\Omega_{p\pm} = \wp_{p\pm}\mathcal{E}_{p\pm}/2\hbar$ ($\Omega_d = \wp_d\mathcal{E}_{d\pm}/2\hbar$), $\wp_{p+}$=$\wp_{ab}$, $\wp_{p-}$=$\wp_{ab'}$, $\wp_d$=$\wp_{ac}$. Here $\mathcal{E}_\alpha$ is the amplitude of electromagnetic field and $\wp_\alpha$ is the dipole moment, α= $p\pm$, d. The Hamiltonian in rotation wave approximation (RAW)

can be written as [20]

$$\begin{aligned}\mathcal{H} &= \mathcal{H}_0 + \mathcal{H}_I \\ &= \hbar[w_c|c\rangle\langle c| + w_a||a\rangle\langle b| + w_{b'}||b'\rangle\langle b'| + w_b||b\rangle\langle b|] \\ &\quad -\hbar[\Omega_{p+}|a\rangle\langle b|e^{-iw_p t} + \Omega_{p-}|a\rangle\langle b'|e^{-iw_p t} \\ &\quad +\Omega_d|a\rangle\langle c|e^{-iw_d t} + h.c.], \end{aligned} \tag{B.7}$$

where w_i is the transition frequency between the levels $|i\rangle$ and absolute ground state and w_p (w_d) represents the central frequency of probe (drive) field. The equation of motion for the tripod system is given by the density-matrix equation

$$\frac{\partial \rho}{\partial t} = \; - \; \frac{i}{\hbar}[\mathcal{H}, \rho] + \text{decay} \;\; \text{terms.} \tag{B.8}$$

Next we use the slowly varying amplitude approximations transforming $\rho \rightarrow \tilde{\rho}$ to eliminate the rapid temporal oscillations

$$\begin{aligned}\rho_{ab} &= \tilde{\rho_{ab}} e^{-iw_p t}, \\ \rho_{ab'} &= \tilde{\rho_{ab'}} e^{-iw_p t}, \\ \rho_{ac} &= \tilde{\rho_{ac}} e^{-i(w_d) t}, \\ \rho_{ii} &= \tilde{\rho_{ii}}. \end{aligned} \tag{B.9}$$

Thus by applying standard semiclassical methods [20], we find the following dynamic equations for density matrix elements:

$$\begin{aligned}\frac{\partial \rho_{aa}}{\partial t} &= i[\Omega^*_{p+}\rho_{ba} - \Omega_{p+}\rho_{ab} + \Omega^*_{p-}\rho_{b'a} - \Omega_d \rho_{ab'} + \Omega^*_d \rho_{ca} - \Omega_d \rho_{ac}] \\ &\quad -3\gamma\rho_{aa}, \\ \frac{\partial \rho_{bb}}{\partial t} &= i[\Omega_{p+}\rho_{ab} - \Omega^*_{p+}\rho_{ba}] + 2\gamma\rho_{aa} \end{aligned}$$

$$
\begin{aligned}
\frac{\partial \rho_{b'b'}}{\partial t} &= i[\Omega_{p-}\rho_{ab'} - \Omega^*_{p-}\rho_{b'a}] + 2\gamma\rho_{aa} \\
\frac{\partial \rho_{cc}}{\partial t} &= i[\Omega_d\rho_{ac} - \Omega^*_d\rho_{ca}] + 2\gamma\rho_{aa} \\
\frac{\partial \rho_{ab}}{\partial t} &= i[\delta\rho_{ab} + \Omega^*_{p+}(\rho_{bb} - \rho_{aa}) + \Omega^*_{p-}\rho_{b'b} + \Omega^*_d\rho_{cb}] - 3\gamma\rho_{ab} \\
\frac{\partial \rho_{ab'}}{\partial t} &= i[\delta\rho_{ab'} + \Omega^*_{p-}(\rho_{b'b'} - \rho_{aa}) + \Omega^*_{p+}\rho_{bb'} + \Omega^*_d\rho_{cb'}] - 3\gamma\rho_{ab'} \\
\frac{\partial \rho_{ac}}{\partial t} &= i[\Delta\rho_{ac} + \Omega^*_d(\rho_{cc} - \rho_{aa}) + \Omega^*_{p+}\rho_{bc} + \Omega^*_{p-}\rho_{b'c}] - 3\gamma\rho_{ac} \\
\frac{\partial \rho_{bb'}}{\partial t} &= i[\Omega_{p+}\rho_{ab'} - \Omega^*_{p-}\rho_{ba}] - \gamma_{bb'}\rho_{bb'} \\
\frac{\partial \rho_{bc}}{\partial t} &= i[\Omega_{p+}\rho_{ac} - \Omega^*_d\rho_{ba} - (\Delta - \delta)\rho_{bc}] - \gamma_{bc}\rho_{bc} \\
\frac{\partial \rho_{b'c}}{\partial t} &= i[\Omega_{p-}\rho_{ac} - \Omega^*_d\rho_{b'a} - (\Delta - \delta)\rho_{b'c}] - \gamma_{b'c}\rho_{b'c} \qquad \text{(B.10)}
\end{aligned}
$$

Here the δ (Δ) is the detuning for the probe(drive) field, γ is the rate of radiative decay and $\gamma_{bb'}$, γ_{bc} and $\gamma_{b'c}$ are the dephasing rate. For simplicity, we assume the drive field is on resonance in the following calculation, Δ=0.

The off diagonal coherence terms ρ_{ab} and $\rho_{ab'}$ can be obtained by using the solutions of Eqs. (B.10). With the assumption of $|\Omega_d| \gg |\Omega_{p\pm}|$, the analytical solutions for the probe transitions are obtained to the first order in both weak fields Ω_{p+} and Ω_{p-} as

$$
\rho_{ab} = \frac{\Omega_{p+}(i\gamma_{bc} - \delta)}{(|\Omega_d|^2 + 2\gamma\gamma_{bc} - \delta^2) + i(2\gamma + \gamma_{bc})\delta}, \qquad \text{(B.11)}
$$

$$
\rho_{ab'} = \frac{\Omega_{p-}(i\gamma_{b'c} - \delta)}{(|\Omega_d|^2 + 2\gamma\gamma_{b'c} - \delta^2) + i(2\gamma + \gamma_{b'c})\delta}. \qquad \text{(B.12)}
$$

The analytical solutions, ρ_{ab} and $\rho_{ab'}$, for the off diagonal coherence are EIT solution. We find out the coherence term in a tripod system is the same for both the EIT and double-EIT case.

APPENDIX C

OPEN SYSTEM MODEL TO DESCRIBE TIME OF FLIGHT EFFECT

In this appendix we describe briefly the open system considerations for the system of our interest. The system to describe the effect of artificial decays due to finite time of interaction of the atoms during the time of flight through the laser beams could be modelled as shown in the Fig. 37. Correspondingly our equations of motion (6.5) will be modified to

$$\begin{aligned}
\frac{\partial \rho_{aa}}{\partial t} &= -2(\gamma_{ab}+\gamma_{ac}+\gamma_E)\rho_{aa} + i\Omega\rho_{ba} - i\Omega^*\rho_{ab} \\
&\quad + ir\Omega\rho_{ca} - ir^*\Omega^*\rho_{ac} \\
\frac{\partial \rho_{ab}}{\partial t} &= -(\gamma_{ab}+\gamma_{ac}+2\gamma_E+\Gamma_b/2)\rho_{ab} - i\Omega(\rho_{aa}-\rho_{bb}) \\
&\quad + ir\Omega\rho_{cb} \\
\frac{\partial \rho_{ac}}{\partial t} &= -(\gamma_{ab}+\gamma_{ac}+2\gamma_E+\Gamma_c/2+i\Delta)\rho_{ac} + i\Omega\rho_{bc} \\
&\quad - ir\Omega(\rho_{aa}-\rho_{cc}) \\
\frac{\partial \rho_{bb}}{\partial t} &= R - 2\gamma_E\rho_{bb} - \Gamma_b\rho_{bb} + \Gamma_c\rho_{cc} + 2\gamma_{ab}\rho_{aa} - i\Omega\rho_{ba} \\
&\quad + i\Omega^*\rho_{ab} \\
\frac{\partial \rho_{bc}}{\partial t} &= -(2\gamma_E+\gamma_{bc}+(\Gamma_b+\Gamma_c)/2+i\Delta)\rho_{bc} + i\Omega^*\rho_{ac} \\
&\quad - ir\Omega\rho_{ba} \\
\frac{\partial \rho_{cc}}{\partial t} &= R - 2\gamma_E\rho_{cc} - \Gamma_c\rho_{cc} + \Gamma_b\rho_{bb} + 2\gamma_{ac}\rho_{aa} - ir\Omega\rho_{ca} \\
&\quad + ir^*\Omega^*\rho_{ac}\,. \qquad \text{(C.1)}
\end{aligned}$$

Here, R is the rate at which atoms enter into interaction region and γ_E is the effective decay of the atomic population due to exit of atoms from the interaction region given

by $(t_{\text{flight}})^{-1}$. Here t_{flight} is flight time of atom through the laser beams. Demanding that in steady state the total change in poulation should be zero, i.e.,

$$\frac{\partial \rho_{aa}}{\partial t} + \frac{\partial \rho_{bb}}{\partial t} + \frac{\partial \rho_{cc}}{\partial t} = 0, \tag{C.2}$$

gives

$$\rho_{aa} + \rho_{bb} + \rho_{cc} = \frac{R}{\gamma_E}. \tag{C.3}$$

Thus to restrict any build up of population in the interaction region, we need the condition $R = \gamma_E$. Now we make a very approximate estimate as in the following.

1. Since the time of flight is order of miliseconds as compared to spontaneous decay time of order of nanoseconds, we can drop γ_E compared to γ_{ij} in the equations for ρ_{aa}, ρ_{ab} and ρ_{ac}.

2. Moreover, as we are working under the CPT condtion, if we assume $\rho_{bb} \approx \rho_{cc} \approx 0.5$ (and also using the condition that $R = \gamma_E$), the first two terms in both equations for ρ_{bb} and ρ_{cc} will cancel with each other.

Thus all the above equations in (C.1) reduce to exactly the same form as in closed system Eqs. (2.14), except for the equation for ground state coherence ρ_{bc}, because γ_E is comparable to γ_{bc}. Therefore, in our calculation the time of flight induced decay primarily affects the dephasing and the population decay is not affected as much.

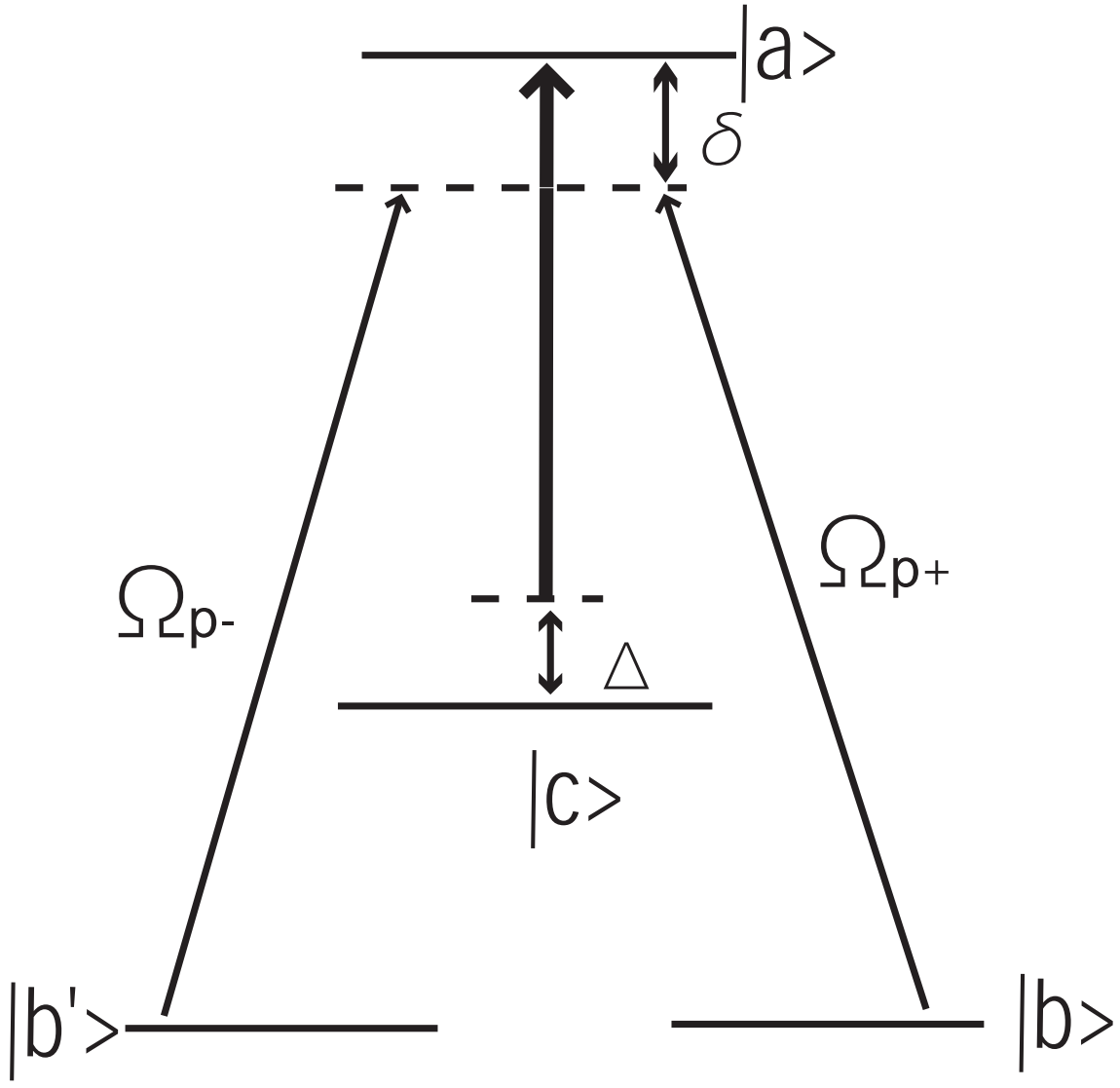

Fig. 36. Diagram showing the energy level of tripod system

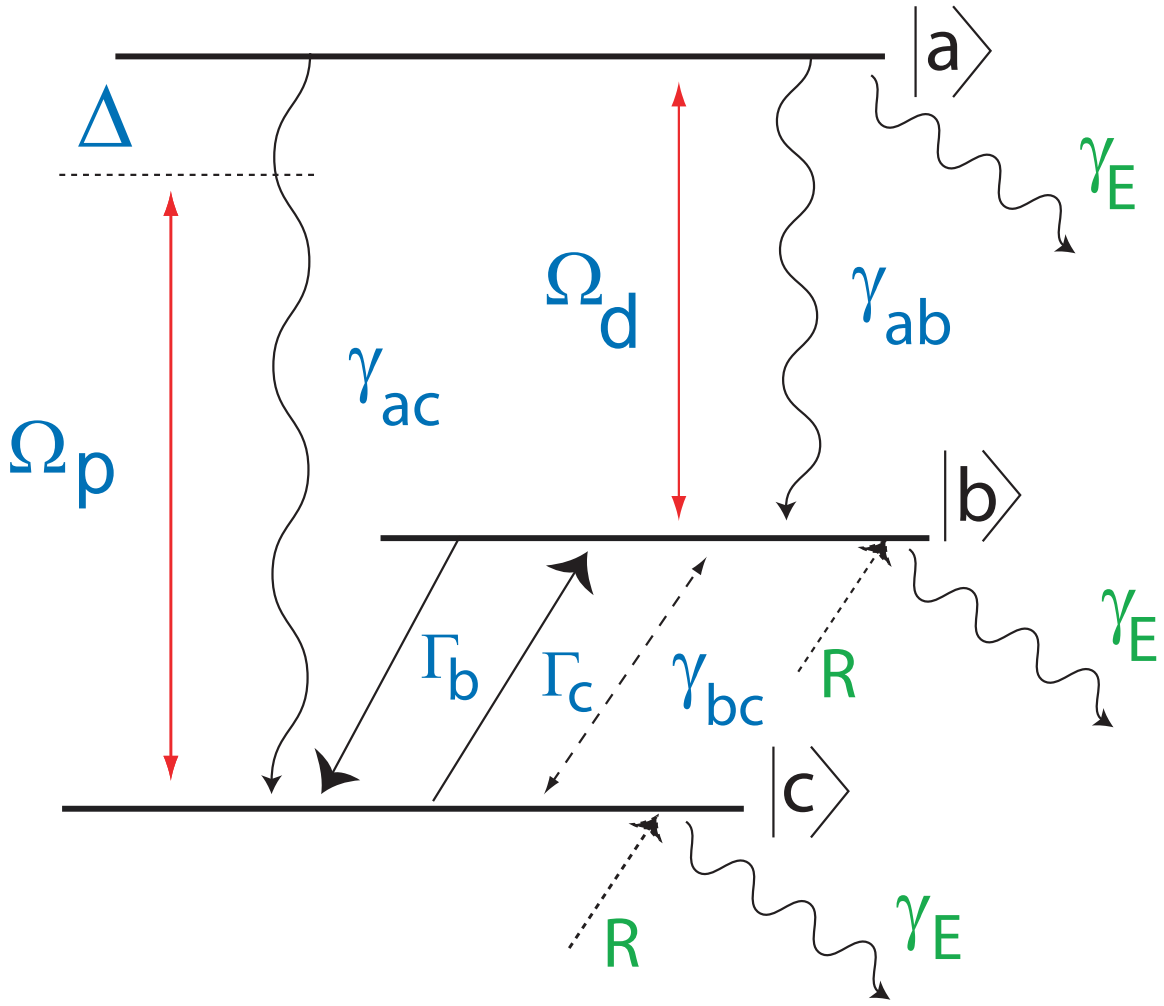

Fig. 37. (Color online) The model for an open system. Here R is the rate at which atoms enter into interaction region and γ_E is the effective decay of the atomic population due to exit of atoms from the interaction region.

VITA

Name: Paul Steve Hsu

Address: Department of Physics, Texas A&M University, College Station, Tx, 77843-4242.

E-mail: p-hsu@tamu.edu; phsu4031@yahoo.com

Education:

Ph. D. in Physics, Texas A&M University (May 2008).

B.S., Physics, National Central University, Taiwan (July 2001).

Work Experience:

1. Internship in the AFRL, Dayton OH (6/2007-12/2007).

2. Visiting scholar at Wright State University, Dayton, OH (2007/8-2007/12).

3. Research and teaching assistant at Physics Dept., Texas A&M University (2002/9-2007/5).

4. Research assistant in the at Physics Dept., National Central University (9/2000-6/2002).

5. Computer lab assistant in the National Central University(6/1998-6/1999).

Awards and Honors:

1. National Research Council (NRC) Postdoctoral Research Award (Air Force Research Laboratory, Wright-Patterson Air Force Base, Dayton OH).

2. Research week winner among the best 3 at Texas A&M.

3. GPA:3.8/4.0 (in Texas A&M Ph. D program).

4. Creativity research awards of undergraduate project competition from NSF (Taiwan).

The typist for this dissertation was Paul Steve Hsu